

# Final Report on: “WP2 – Impacts of Seismicity: Transmission to People, Property and Well Integrity”

A Technical Report commissioned by the Oil and Gas Authority (OGA)

**PROJECT: OGA Scientific and Engineering Analysis of the Preston New Road 1z (PNR-1z) Data**

**Benjamin Edwards** PhD FHEA FGS ([intra](#)**seis** Ltd.)

**Helen Crowley** PhD (Independent Consultant)

**Rui Pinho** PhD (Independent Consultant)

Independent Expert Review

**Julian Bommer** PhD CEng FICE (Bommer Consulting Ltd.)

**Report Number: ISEIS-HC-RP-JJB-OGA\_WP2-4 29-10-2019**

## Version History

Version	Date	Author(s)	Reviewer(s)
4 (Revised)	29-10-2019	Edwards, Crowley, Pinho	OGA, Bommer
3 (Submitted)	26-09-2019	Edwards, Crowley, Pinho	Bommer
2 (Final Draft)	23-09-2019	Edwards, Crowley, Pinho	Bommer
1 (Draft)	27-08-2019	Edwards, Crowley, Pinho	Bommer
0 (Early Draft)	19-08-2019	Edwards, Crowley, Pinho	

[Blank Page]

## Executive Summary

Cuadrilla Resources began hydraulic fracturing at Preston North Road (PNR), Lancashire, in October 2018. By the end of the operation in December 2018 the British Geological Survey (BGS) had detected 57 seismic events on a dense network of seismometers at the surface. The magnitude of these detected events was small ( $-0.8 \leq M_L \leq 1.5$ ), although the largest two ( $M_L$  1.1 and 1.5) were reported as European Macroseismic Intensity (EMS-98) II (scarcely felt: felt only by very few people at rest in houses) by the BGS. On completion of the operations, the Oil and Gas Authority (the regulator) commissioned a series of scientific and engineering studies on the data collected. This report documents the investigations for Work Package 2 of these analyses and aims to investigate the induced seismicity at PNR and potential impacts of hypothetical future events.

This report comprises four main sections. Section 2 provides readers with an overview of several important topics that are of relevance to induced seismicity at PNR and the analysis documented later in this report. Section 3 documents site characterisation work undertaken in the surrounding region and later used for interpretation of recorded ground motion data and for development of scenario calculations. Section 4 provides an analysis of the recordings of the 57 detected earthquake events, focussing in particular on the performance of predictive models. Section 5 then uses these predictive models to determine hypothetical earthquake scenarios at PNR in terms of ground shaking and macroseismic intensity. Finally, using these scenario calculations a risk analysis is undertaken, determining the exposure of people and impact on buildings at the surface in addition to the well itself.

### *Site Characterisation and Ground Motion Amplification*

The shear-wave velocity of near surface geological deposits is a reliable proxy for ‘site-amplification’ effects. These amplification effects can lead to significant spatial differences in the levels of shaking from one earthquake and are often correlated with regions of high macroseismic intensity and damage due to large earthquakes. Through multi-channel analysis of surface wave (MASW) experiments our site investigation work shows that the region around PNR is characterised by sediments of low shear-wave velocity (as low as 180 m/s at the surface increasing, in some cases, to 400 m/s at depths of about 30 m). Three main geological regions were classified and measured, those with superficial deposits of (i) blown-sand, (ii) till and (iii) alluvium. The blown sand deposits, which extend over much of the coastal areas of Blackpool and Lytham St. Annes, lead to the lowest velocity sites, with a 30 m average shear-wave velocity ( $V_{s30}$ ) of around 200 m/s. The site characterised by till deposits showed the highest  $V_{s30}$ , at around 260 m/s. The site with alluvial and peat deposits had  $V_{s30} = 240$  m/s. These values are all indicative of very low velocity and potentially strongly amplifying sediments. For reference,  $V_{s30}$  values tend to lie between 180 – 360 m/s (soils), 380 – 760 m/s (very dense soil and ‘soft’ rock) and  $> 760$  m/s (rock). The site conditions in the region around PNR therefore lead to significantly higher motions (e.g., up to 2 – 3 times higher for peak ground velocity, PGV, or more at the fundamental resonance frequency) than would be experienced for the same earthquake on rock sites. Fortunately, the nature of these soils means that we also expect significant non-linear effects at high strain levels. As a result, for large magnitude

earthquakes the soils do not behave linearly, which generally leads to lower amplification levels during strong shaking.

#### *Recorded Ground Motion Data and Predictive Model Performance*

The recorded ground motion data from 57 earthquakes have been processed, visually inspected and compared to predictions from two earthquake ground motion models (GMMs) developed specifically for induced seismicity (Atkinson, 2015 and Douglas et al., 2013). In general, GMMs require moment magnitude as input, and these models are no exception. To determine moment magnitude for the PNR events we tested two models that convert the available local magnitudes to moment magnitudes: an empirical model developed for European earthquakes (Gruenthal et al., 2009), which has been shown to perform well against UK tectonic earthquakes; and an empirical-theoretical model developed for induced seismic events in St. Gallen, Switzerland (Edwards et al., 2015). We found that the combination of the Atkinson (2015) ground motion prediction equation (GMPE) and the Edwards et al. (2015) magnitude conversion led to unbiased predictions, apart from a slight under-prediction at very short epicentral distances ( $R_{\text{epi}} < 3$  km) for the smallest ( $M_L < 0$ ) earthquakes. Subsequent to this work being completed Cuadrilla Resources published an empirical magnitude conversion equation based on the PNR data that was almost identical to that of Edwards et al. (2015), confirming it as a good choice in this case. Based on the fit to the data and other considerations, we proposed a transition between the induced earthquake magnitude conversion (valid for  $M_L \leq 1.5$ ) and that of Gruenthal et al. (2009) for  $M_L > 2.5$ .

#### *Scenarios for Risk Calculations*

We propose hypothetical earthquake scenarios that are used in the remaining analyses, which aim to better understand the potential effects from larger induced earthquakes at the PNR site. These scenarios were proposed prior to the  $M_L$  2.9 event that occurred in August 2019, but this fact nevertheless does not alter the logic behind their choice. Five scenarios are used:  $M_L$  2.5, 3.0, 3.5, 4.0 and 4.5. Based on events that have already occurred at PNR and Preese Hall, in addition to general considerations of UK seismicity, we define the events on a sliding qualitative scale from ‘likely to happen’ ( $M_L$  2.5), to ‘may happen’ ( $M_L$  3.5) and ‘unlikely to happen’ ( $M_L$  4.5). It is important to note that no probabilities are assigned to these scenarios and they are purely representative of qualitative scenarios (‘likely’ through to ‘unlikely’). For instance, while we consider it unlikely that a  $M_L$  4.5 event occurs at PNR, there is international precedent for hydraulic fracturing to lead to events of this magnitude (even if at a vanishingly small percentage of hydraulically fractured wells), and similar magnitude (and shallow) UK tectonic events have occurred in the past. It is, therefore, not possible to rule out the  $M_L$  4.5 scenario.

Using the Atkinson (2015) GMPE we predict PGV, peak ground acceleration (PGA) and spectral accelerations (SA) at ten oscillator periods (0.03 to 5 s) for the 5 earthquake scenarios and 3 representative  $V_{s30}$  values (200, 240 and 280 m/s). In an initial analysis we use the PGV predictions to calculate the expected macroseismic intensity across the region. Using the median PGV predictions at a conservative  $V_{s30} = 200$  m/s, we find median epicentral intensities

reach IV for the  $M_L$  3.5 scenario and extend for roughly 5 km. In terms of the 84<sup>th</sup>-percentile PGV predictions (only 16 % of motions are expected to exceed this level), we find that intensity V is reached at the epicentre. In this case, PGV exceeds 1.5 cm/s, which is a rough threshold at which localised cosmetic (non-structural) damage may occur. For the largest scenario,  $M_L$  4.5, we predict median intensities of VI extending out to 4 km from PNR. At the 84<sup>th</sup>-percentile PGV predictions (which, again, may only occur in isolated pockets, not over the whole region) we find that intensities of VII (EMS-98 scale: damaging) may occur out to about 3 km.

Uncertainties in converting PGV to intensity are high, with roughly  $\pm 1$  unit at one standard deviation. In terms of providing a regional picture (median PGV) and potential localised effects (84<sup>th</sup>-percentile PGV) of the effect of induced seismicity these scenarios provide a useful insight. However, instead of providing intensity measures, a more thorough approach is to perform a risk analysis, considering the input ground motion and calculating the effect of this on buildings. For this purpose, 200 ground motion scenarios have been calculated for each earthquake scenario, and each  $V_{s30}$ . Each of the ground motion fields is sampled from the full statistical model (as opposed to only using the median predictions or 84<sup>th</sup>-percentiles) and considers a spatially correlated ground motion field (nearby locations experience similarly higher- or lower-than-average motions). The result is a non-homogeneous distribution of predicted ground motions with statistical characteristics defined by the GMPEs. This means that in any one of the 200 realisations for one earthquake magnitude and  $V_{s30}$ , a particular location could experience median, or  $\pm 1$ , 2 and up to 3 standard deviations from the median.

### *Risk Calculations*

Based on the various scenarios defined above, risk calculations are performed in a semi-probabilistic framework. For each of the earthquake and  $V_{s30}$  scenarios, the 200 randomly generated ground motion fields are used. Each is compared with probabilistic fragility curves for an inventory of structures in a 10 x 10 km region surrounding PNR. For each of the 200 ground motion fields, the resulting damage in terms of damage state (DS) levels (1 – 4, from minor/cosmetic through to heavy structural damage, respectively) and additionally chimney collapse is calculated. Statistics are then calculated over the 200 realisations, and a mean and median level (in terms of the percentage of structures at each damage state) is calculated (Table E1). The difference between mean and median predictions gives an indication of the influence of outliers (i.e., particularly high motions, well in excess of the median PGV) on the resulting damage. This could be indicative, for example, of a small built-up area being hit by particularly high (e.g., 95<sup>th</sup>-percentile motions) for one of the 200 random ground motion realisations.

It is worth reflecting on these results in light of the more recent induced seismic events that occurred in August 2019, with the largest reaching  $M_L$  2.9. The larger event, at  $M_L$  2.9 is close to our  $M_L = 3.0$  scenario, and lies between the ‘likely to happen’ ( $M_L$  2.5) to ‘may-happen’ ( $M_L$  3.5) qualitative descriptors used in this report. Median predicted PGV for an  $M_L = 3.0$  at the epicentre is about 0.5 cm/s (for  $V_{s30} = 240$  m/s), which is approximately the threshold of intensity IV according to Caprio et al. (2015). BGS assigned the event as intensity VI due to some reports of minor damage (DS1), which is unusual for an event of this magnitude (see, for

instance, Section 4.1). The risk analyses performed here showed a *median* prediction (which has a 50% probability of not being exceeded) of zero buildings with DS1 in this case. Nevertheless, variability in ground motion (which is taken into account in our analyses) means that a range of outcomes are possible for one magnitude scenario. Due to this, and the contribution of outlier events, a *mean* of 0.1 % of buildings at DS1 (of the order tens of buildings) was calculated, which is consistent with reports made to the BGS. It is noted, however, that we are not aware if the reports of DS1 have been verified at this stage, since BGS rely on ‘did you feel it’ reports that can be self-submitted online.

Finally, the impact of ground motions on the well itself are calculated. We find that the well can accommodate significant loading without the occurrence of damage. Two cases are looked at: (i) deformations induced by motions from a nearby earthquake and (ii) bending and shear stresses due to a fault traversing the well. In terms of induced ground strains due to a nearby earthquake, we find that the level of motion expected due to a  $M_L$  4.5 event would be unlikely to induce failure. Specifically, 98.8 % of realised motions from such an event would be lower than the threshold for damage. In terms of fault shearing, assuming a movement of 17 mm during the largest considered earthquake ( $M_L$  4.5), we find that there is a critical length less than 0.075 % of the production well length that is sensitive this slip; the fault would have to cut through this precise region in order for the bending moment to overcome the well’s elastic flexural capacity, which again constitutes the threshold for damage, not necessarily failure, to occur.

Table E1. Mean and median percentage of buildings at each damage state within a 10 x 10 km grid around PNR for scenario events, assuming  $V_{s30} = 240$  m/s. See Section 2.6 for a description of damage states (DS) 1-4.

Scenario ( $M_L$ )	DS1 (%)		DS2 (%)		DS3 (%)		DS4 (%)		Chimney failure (%)	
	Mean	Median	Mean	Median	Mean	Median	Mean	Median	Mean	Median
<b>2.5</b>	0.0	0.0	0.0	0.0	0.0	0.0	0.0	0.0	0.0	0.0
<b>3</b>	0.1	0.0	0.0	0.0	0.0	0.0	0.0	0.0	0.0	0.0
<b>3.5</b>	0.9	0.2	0.2	0.0	0.0	0.0	0.0	0.0	0.1	0.0
<b>4</b>	3.9	2.2	1.6	0.2	0.8	0.0	0.4	0.0	1.4	0.2
<b>4.5</b>	9.6	8.6	5.4	3.5	3.2	0.8	2.3	0.1	5.4	2.1

## Contents

1.	Introduction and Structure of Work Package .....	1
2.	Overview of Ground Motions and their Impact .....	8
2.1	Summary of Ground-Motion Characteristics.....	8
2.1.1	Peak Displacement, Velocity, Acceleration and Response Spectra .....	9
2.1.2	Significant Shaking Duration.....	11
2.1.3	Frequency Content.....	11
2.1.4	Variability .....	12
2.1.5	Spatial Correlation .....	13
2.2	Factors Influencing Ground Motions.....	14
2.2.1	Earthquake Magnitude .....	14
2.2.2	Attenuation.....	16
2.2.3	Site Characteristics.....	17
2.2.4	Earthquake Stress Drop.....	19
2.3	Prediction of Ground Motions .....	20
2.4	Relationship between Ground Motions and Macroseismic Intensity .....	25
2.4.1	Macroseismic Intensity .....	25
2.4.2	Ground Motion to Intensity Conversion Equations.....	26
2.5	Impact of Ground Motion Levels on People.....	27
2.6	Impact of Ground Motion Levels on the Built Environment.....	29
3.	Ground Characterisation at PNR .....	34
3.1	Site Characterisation Measurements Undertaken at PNR .....	34
3.1.1	Site L001 .....	35
3.1.2	Site L003 .....	40
3.1.3	Site L009.....	42
3.2	Shear-Wave Velocity Model for Selected PNR sites .....	44
3.2.1	Till deposit sites (L001).....	44
3.2.2	Peat/Alluvium Deposit Sites (L003).....	46
3.2.3	Blown sand deposit sites (L009).....	48
3.3	$V_{s30}$ for PNR sites .....	51
4.	Induced Events and Ground Motions Observed at PNR .....	52
4.1	Macroseismic Data for the Events .....	53
4.2	Surface Ground Motion Recordings from PNR Events.....	56

4.3	Assessment of Predictive Models for PNR Ground Motions .....	58
4.3.1	Atkinson (2015) GMPE using Gruenthal et al. (2009) <b>M</b> .....	59
4.3.1	Atkinson (2015) GMPE using Edwards et al. (2015) <b>M</b> .....	61
4.3.2	Douglas et al. (2013) GMPE using Gruenthal et al. (2009) <b>M</b> .....	63
4.3.3	Douglas et al. (2013) GMPE using Edwards et al. (2015) <b>M</b> .....	65
4.3.4	Summary of Comparison .....	67
4.4	Comparison of Observed Motions with Anthropogenic Sources of Vibration.....	68
5.	Assessment of Potential Impact of Future Scenarios .....	71
5.1	Proposal of Potential Induced Earthquake Scenarios .....	71
5.2	Assessment of Potential Shaking Levels .....	71
5.2.1	$M_L = 2.5$ Scenario .....	72
5.2.2	$M_L = 3.5$ Scenario .....	73
5.2.3	$M_L = 4.5$ Scenario .....	75
5.2.4	Scenario Ground Motion Variability .....	76
5.3	Inventory of Exposed Structures and Population.....	76
5.3.1	Extent of Exposure Model .....	77
5.3.2	Datasets .....	77
5.3.3	Field Trip (9 <sup>th</sup> June 2019) .....	81
5.3.4	Mapping Scheme .....	83
5.3.5	Exposure Maps.....	83
5.4	Assessment of Potential Impact on the Local Community .....	85
5.5	Assessment of Potential Impact on the Built Environment .....	86
5.5.1	Fragility Functions – Chimneys.....	86
5.5.2	Fragility Functions - Buildings .....	87
5.5.3	Scenario Damage Assessment .....	91
5.5.4	Discussion of Results .....	96
5.6	Assessment of Potential Impact on Well Integrity .....	96
5.6.1	Well Integrity due to Fault Slip .....	99
5.6.2	Well Integrity due to Wave-Induced Ground Strain.....	101
6.	Conclusions .....	101
7.	Acknowledgements .....	103
8.	References .....	104

## 1. Introduction and Structure of Work Package

On 25 February 2019 the Oil and Gas Authority (OGA) announced that:

“Cuadrilla recently completed hydraulic fracturing operations at Preston New Road [PNR]. As part of our normal responsibilities as one of the regulators of this industry, the OGA now plans to carry out a scientific analysis of the data gathered during these operations. It is not a review of the traffic light system. As is usual in these circumstances, the OGA will work with recognised and independent geologists and scientists with expertise in hydraulic fracturing operations to assess these data and will provide updates on our website as appropriate.”

This report documents Work Package 2 (WP2) of this assessment of the PNR-1z data, which aims to address the impacts of seismicity, including transmission to people and property, as well as impacts on well integrity. This includes assessment of ground motions that have been recorded at PNR and that could occur under potential future induced earthquake scenarios.

The report is split into four main sections. Section 2 introduces earthquake ground motions and their impacts, including a summary of their ground motion characteristics, and factors that influence these. An overview of how earthquake ground motions are predicted is then provided, followed by a review of how these ground motions can be related to macroseismic (felt) intensities. Section 2 ends by summarising the impact of ground motions on people and the built environment. Section 3 introduces the effect of subsurface site conditions on recorded ground motions and documents the *in situ* measurements and interpretation undertaken to characterise the ground conditions in the vicinity of the PNR site. Section 4 presents an analysis of data recorded during the PNR-1z hydraulic fracturing operation, including macroseismic observations and surface seismometer recordings. The performance of predictive models is then assessed in relation to these data. Section 5 looks into the impacts of hypothetical earthquake events at PNR. Potential earthquake scenarios are proposed for use in this section based on previous UK seismic events and the seismicity observed at PNR to the end of 2018 (i.e., completion of PNR-1z). An assessment of the shaking levels predicted for these events is then undertaken, and based on this, their impact on the built environment and well integrity is determined. As part of this an inventory of exposed structures near to the PNR site is developed.

The first Preston New Road shale gas well (PNR-1z) was fracked over a 3-week period between 15<sup>th</sup> October and 17<sup>th</sup> December 2018, with an extended period of inactivity during November due to operational issues. As part of their licence, Cuadrilla Resources operated within a ‘Traffic Light System’ (TLS, Bommer *et al.* 2006). The TLS has been set by the UK government, based on a review after Preese Hall (Green *et al.*, 2012), as a means to control induced seismicity.

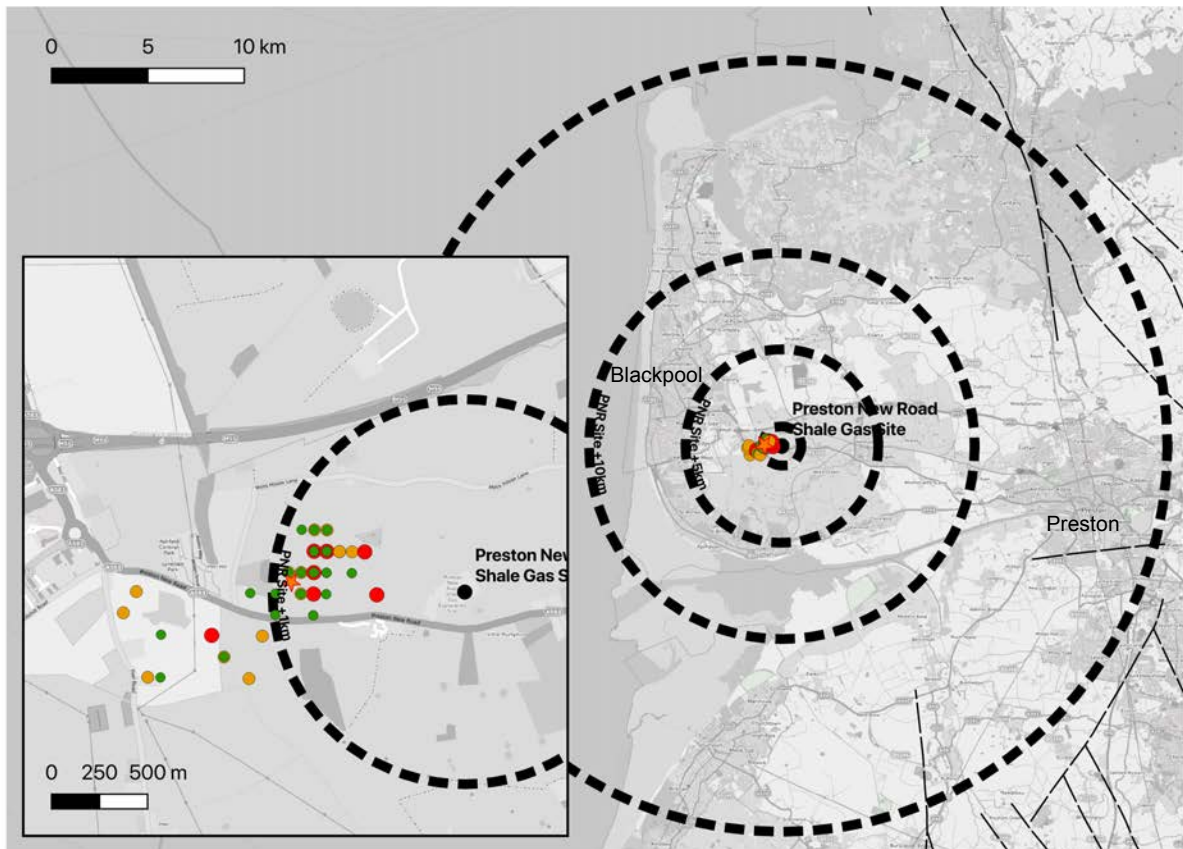


Figure 1.1. Location of PNR site showing areas within 1, 5, 10 and 20 km. Inset: Located seismicity, indicating TLS magnitude category (red, amber, green).

The TLS defines three levels: green (normal operation), amber and red, with earthquake magnitudes  $M_L = 0$  and  $0.5$  triggering the amber and red levels, respectively. In the UK version of the TLS, the amber level triggers a higher level of monitoring and analysis, but otherwise no curtailment of operations. A ‘red light’ leads to a cessation of operations for 18 hours, during which a review of the earthquake event is undertaken. After reviewing the data, if the regulator (the OGA) is satisfied that seismicity is not of concern, the operator is permitted to reinstate well pressure after 18 hours.

During the period 15<sup>th</sup> October to 17<sup>th</sup> December 57 seismic events (Figure 1.1, Table 1.1) were detected and located by the British Geological Survey (BGS) in real-time using seismic monitoring networks operated by Cuadrilla Resources, BGS themselves and the University of Liverpool (Figure 1.2). Earthquake magnitudes were assigned using the newly revised  $M_L$  scale developed by the BGS (Luckett et al., 2018), which extended the existing UK-wide  $M_L$  scale’s validity to distances less than 10 – 20 km. The majority of these events were classified as ‘green light’ events (i.e.,  $M_L < 0$ , as expected during typical operations). In terms of magnitude alone, 17 fell into the ‘amber light’ category and 8 the ‘red light’ category ( $M_L \geq 0.5$ ) (Table 1.1). For the TLS agreed as part of the hydraulic fracture plan for PNR-1z (Cuadrilla Resources, 2018) traffic light events are declared and reported (Cuadrilla Resources, 2019a) by the operator if there is active hydraulic fracturing ongoing at the time of the event. In addition, significant trailing events (i.e., those falling in to the TLS ‘red light’ category) are reported.

The reason being that mitigating action can then be taken (pers. comm. OGA, 2019). Of the 17 events detected by the BGS and falling into the range of ‘amber’ and ‘red light’ magnitudes, only six were during active injection, and therefore declared by the operator (Cuadrilla Resources, 2019a) as ‘pumping’ TLS events (3 ‘red light’ and 3 ‘amber light’). In addition, three further ‘red light’ events were declared as ‘trailing’ events, where seismicity occurs after injection has stopped. These were events on:

- 27/10/2018 11:55:25 ( $M_L$  0.78)
- 04/11/2018 16:24:06 ( $M_L$  0.66)
- 11/12/2018 11:21:15 ( $M_L$  1.5)

Two events (2018-10-24T13:02:29.3, 2018-10-29T18:01:12.2) that exceed the ‘red light’ TLS magnitude threshold according to BGS assigned  $M_L$  were not reported by the operator in the HFP report (Cuadrilla Resources, 2019a). This is due to rounding choice (pers. comm. OGA, 2019), with BGS using standard practice of single decimal place magnitude values (which may push a 0.45 event to 0.5). With magnitudes in the ‘amber light’ category (to two decimal places), these ‘non-pumping’ events did not require reporting.

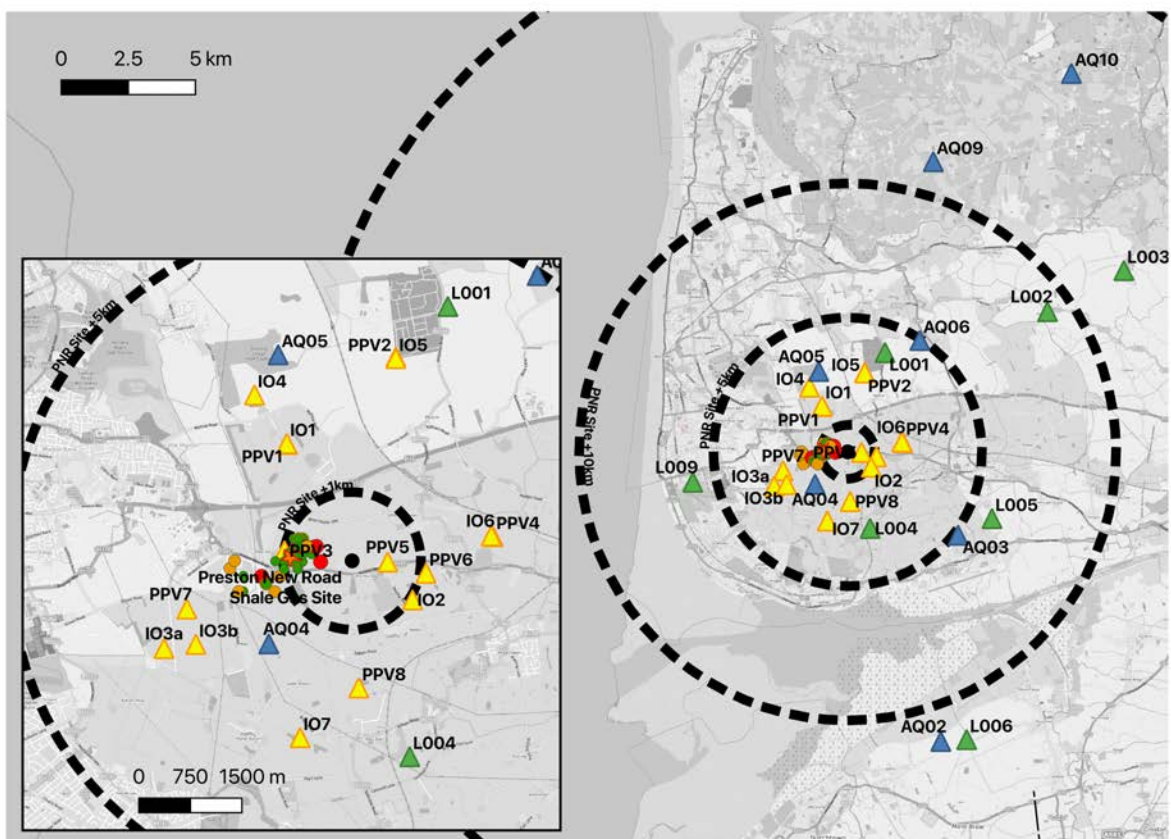


Figure 1.2. Map showing location (inset, zoom on epicentral region) of seismic monitoring stations (yellow: Cuadrilla; Green: University of Liverpool; Blue: BGS). Detected seismic events are shown as in Figure 1.1. Note PPV (peak particle velocity) stations are not used in this analysis due to concerns as to their reliability (Bommer and Edwards, 2018).

This report focuses on all 57 events detected (in real time) by the BGS (Table 1.1). It is noted that other events at PNR-1z (not listed in Table 1.1) are likely to be detected through post-processing of continuous waveform data recorded during the operational period. This may add further (previously undetected) events that occur around the detection threshold of the monitoring network, which is roughly  $M_L$  0 (pers. comm. BGS). It is also noted that this report does not consider the seismicity related to the PNR-2 well, which was hydraulically fractured in August 2019 after the analysis undertaken in this report was completed, and which led to induced events of up to  $M_L$  2.9.

It is important to note that this report does not review the TLS or aim to provide any explanation of the seismicity itself. Rather it provides analysis of the impact of events that have already occurred, or that may occur in the future. Specifically, this report provides an analysis of the ground motions from the induced earthquakes, and potential future earthquakes in terms of their effect on the built environment, community and well integrity.

Table 1.1. BGS located events during the operational period for PNR-1z. Note  $M_L$  computed by BGS to one decimal place. Cuadrilla report to two decimal places which may result in discrepancy between TLS classification. Solid backgrounds indicate declared events (i.e., during pumping or significant trailing events). Hatched backgrounds indicate TLS magnitude classification, but not declared due to no active injection. Note in Cuadrilla Resources (2019b) times are reported as local time (BST then subsequently GMT). Times here are all GMT.

ID	Date	Time	Lat (deg)	Lon (deg)	Depth (km)	$M_L$	Intensity	Cuadrilla Report
2018-10-18T15:48:53.6	18/10/2018	15:48:54	53.785	-2.975	3.2	-0.2		
2018-10-18T22:54:46.8	18/10/2018	22:54:47	53.783	-2.975	3.6	-0.8		
2018-10-18T23:44:41.9	18/10/2018	23:44:42	53.786	-2.978	2.8	-0.3		
2018-10-19T13:20:48.5	19/10/2018	13:20:48	53.783	-2.976	3.7	0.3		
2018-10-20T03:44:01.4	20/10/2018	03:44:01	53.786	-2.978	3.1	0		
2018-10-23T14:45:32.5	23/10/2018	14:45:32	53.787	-2.977	3	0.4		Amber ( $M_L$ 0.40)
2018-10-24T13:02:29.3	24/10/2018	13:02:29	53.785	-2.971	3.5	0.5		
2018-10-24T13:26:26.5	24/10/2018	13:26:26	53.784	-2.97	3.4	0.4		
2018-10-24T13:51:31.5	24/10/2018	13:51:32	53.784	-2.97	2.9	-0.1		
2018-10-24T14:38:30.3	24/10/2018	14:38:30	53.785	-2.967	3.5	0.1		
2018-10-24T23:56:12.9	24/10/2018	23:56:13	53.783	-2.968	3.8	0		
2018-10-25T14:59:27.1	25/10/2018	14:59:27	53.788	-2.965	2.4	0.3		
2018-10-25T17:00:33.8	25/10/2018	17:00:34	53.787	-2.968	2.3	-0.1		
2018-10-25T17:04:13.3	25/10/2018	17:04:13	53.786	-2.963	2.2	-0.6		
2018-10-26T02:13:01.6	26/10/2018	02:13:02	53.787	-2.966	2.3	-0.2		
2018-10-26T11:26:44.6	26/10/2018	11:26:45	53.788	-2.964	2.2	0.2		
2018-10-26T11:36:58.4	26/10/2018	11:36:58	53.787	-2.963	2.9	0.8		Red ( $M_L$ 0.76)
2018-10-26T20:39:22.7	26/10/2018	20:39:23	53.786	-2.966	2.3	-0.1		
2018-10-27T10:47:37.4	27/10/2018	10:47:37	53.787	-2.962	2.2	-0.3		
2018-10-27T10:55:25.2	27/10/2018	10:55:25	53.789	-2.963	2.5	0.8		Red ( $M_L$ 0.78)
2018-10-27T11:07:16.6	27/10/2018	11:07:17	53.787	-2.964	2.2	-0.2		
2018-10-27T11:44:31.1	27/10/2018	11:44:31	53.788	-2.963	2.4	0		
2018-10-27T13:12:34.7	27/10/2018	13:12:35	53.787	-2.964	2.2	-0.4		

ID	Date	Time	Lat (deg)	Lon (deg)	Depth (km)	M <sub>L</sub>	Intensity	Cuadrilla Report
2018-10-29T11:30:38.9	29/10/2018	11:30:39	53.789	-2.962	2.9	1.1	II	Red (M <sub>L</sub> 1.0)
2018-10-29T11:44:41.8	29/10/2018	11:44:42	53.788	-2.965	2.4	-0.2		
2018-10-29T11:43:29.3	29/10/2018	11:43:29	53.786	-2.963	2.4	-0.4		
2018-10-29T11:58:34.5	29/10/2018	11:58:34	53.788	-2.964	2.3	0		
2018-10-29T18:01:12.2	29/10/2018	18:01:12	53.788	-2.963	2.5	0.5		
2018-10-29T21:13:58.6	29/10/2018	21:13:59	53.787	-2.964	2.3	0.1		
2018-10-30T01:37:37.4	30/10/2018	01:37:37	53.788	-2.962	2.1	-0.3		
2018-10-30T14:36:38.4	30/10/2018	14:36:38	53.788	-2.962	2	-0.5		
2018-10-30T15:55:40.0	30/10/2018	15:55:40	53.787	-2.964	2.3	-0.4		
2018-11-01T06:50:58.8	01/11/2018	06:50:59	53.788	-2.964	2.2	-0.3		
2018-11-02T17:44:58.9	02/11/2018	17:44:59	53.788	-2.963	2.2	-0.5		
2018-11-02T22:59:27.4	02/11/2018	22:59:27	53.788	-2.962	2.2	-0.5		
2018-11-04T16:24:06.2	04/11/2018	16:24:06	53.787	-2.958	2.5	0.7		Red (M <sub>L</sub> 0.66)
2018-12-10T10:30:57.8	10/12/2018	10:30:58	53.788	-2.96	2.1	-0.3		
2018-12-11T09:35:01.1	11/12/2018	09:35:01	53.789	-2.963	1.8	-0.1		
2018-12-11T09:34:03.3	11/12/2018	09:34:03	53.789	-2.963	1.8	-0.2		
2018-12-11T09:51:36.4	11/12/2018	09:51:36	53.79	-2.964	1.6	-0.4		
2018-12-11T09:53:31.1	11/12/2018	09:53:31	53.789	-2.961	1.6	0.1		Amber (M <sub>L</sub> 0.10)
2018-12-11T10:06:44.6	11/12/2018	10:06:45	53.788	-2.962	1.9	-0.1		
2018-12-11T10:18:46.4	11/12/2018	10:18:46	53.79	-2.962	2.3	0		Amber (M <sub>L</sub> 0.00)
2018-12-11T10:20:27.5	11/12/2018	10:20:28	53.789	-2.963	1.9	-0.4		
2018-12-11T10:24:26.0	11/12/2018	10:24:26	53.79	-2.962	1.8	-0.5		
2018-12-11T10:34:35.3	11/12/2018	10:34:35	53.79	-2.963	1.7	0		
2018-12-11T11:21:15.1	11/12/2018	11:21:15	53.789	-2.962	1.6	1.5	II	Red (M <sub>L</sub> 1.5)
2018-12-13T13:25:16.7	13/12/2018	13:25:17	53.789	-2.961	2.1	0		

ID	Date	Time	Lat (deg)	Lon (deg)	Depth (km)	M <sub>L</sub>	Intensity	Cuadrilla Report
2018-12-14T13:06:05.3	14/12/2018	13:06:05	53.789	-2.962	1.7	-0.2		
2018-12-14T13:05:50.3	14/12/2018	13:05:50	53.789	-2.963	1.8	-0.6		
2018-12-14T13:06:36.8	14/12/2018	13:06:37	53.789	-2.962	1.8	-0.5		
2018-12-14T13:09:51.4	14/12/2018	13:09:51	53.789	-2.96	1.7	0.1		
2018-12-14T13:18:30.3	14/12/2018	13:18:30	53.789	-2.962	1.8	-0.1		
2018-12-14T13:34:42.2	14/12/2018	13:34:42	53.789	-2.962	1.8	-0.3		
2018-12-14T13:35:50.1	14/12/2018	13:35:50	53.79	-2.963	1.9	-0.5		
2018-12-14T13:41:05.5	14/12/2018	13:41:05	53.789	-2.959	2.2	0.9		Red (M <sub>L</sub> 0.86)
2018-12-14T14:51:56.5	14/12/2018	14:51:57	53.789	-2.961	2.1	0.1		

## **2. Overview of Ground Motions and their Impact**

The ground motions resulting from earthquakes are complex natural phenomena, the physics of which is, in parts, poorly understood. The earthquake ground motion field (the shaking at some reference horizon, typically the surface) is of primary interest in seismic hazard analysis. It is this motion that applies loading to structures and, in the worst case, leads to damage or failure. The ground motion field itself is a result of several processes, some of which work against one another, and which can therefore lead to significantly different ground motion fields from earthquake to earthquake. In the following section, the parameters used to characterise the complexity of the ground motion field are summarised, in addition to the phenomena that may influence these. We then provide an overview of the relationship between ‘instrumental’ ground motions (i.e., those that are recorded by seismometers or accelerometers) and macroseismic intensity, which reflects a qualitative description of shaking effects (from human perception, through to various damage states). We finally review the effects of ground motion levels on structures and people and through examples relevant to induced seismicity.

### ***2.1 Summary of Ground-Motion Characteristics***

Ground motions from earthquake events are transient movements of the surface as seismic waves radiated by an earthquake pass by. At any point at the surface (or to an extent, the subsurface) these movements can be recorded using an accelerometer (recording acceleration) or seismometer or geophone (recording velocity). These instruments typically record continuously in three orthogonal directions (vertical and two horizontal) at sample rates at or above 100 samples per second (although lower sample rates are sometimes utilised). For modern, high-quality instrumentation, signals recorded on either type can be integrated or differentiated to provide any of the three measures of motion (displacement, velocity or acceleration). After an earthquake, the radiated P (primary) and S (secondary, or shear) waves are recorded along with their multiples and coda (waves scattered due to subsurface heterogeneity). In some cases, other waves are also observed, such as surface waves – usually evident for shallow earthquakes and/or distant recordings.

Earthquake ground motions are characterised in various ways. For a given location the characteristics of shaking can broadly be split into: (i) point measures such as peak displacement, velocity and acceleration; (ii) duration of shaking; and (iii) frequency content. Variability of ground motions is also an important characteristic to consider. This variability is described in term of (iv) event-to-event and (v) site-to-site variations around the median. In terms of ground motion fields (i.e., motions over a surface area), the ground motions may also be characterised in terms of their (vi) spatial correlation. These topics are addressed in the following.

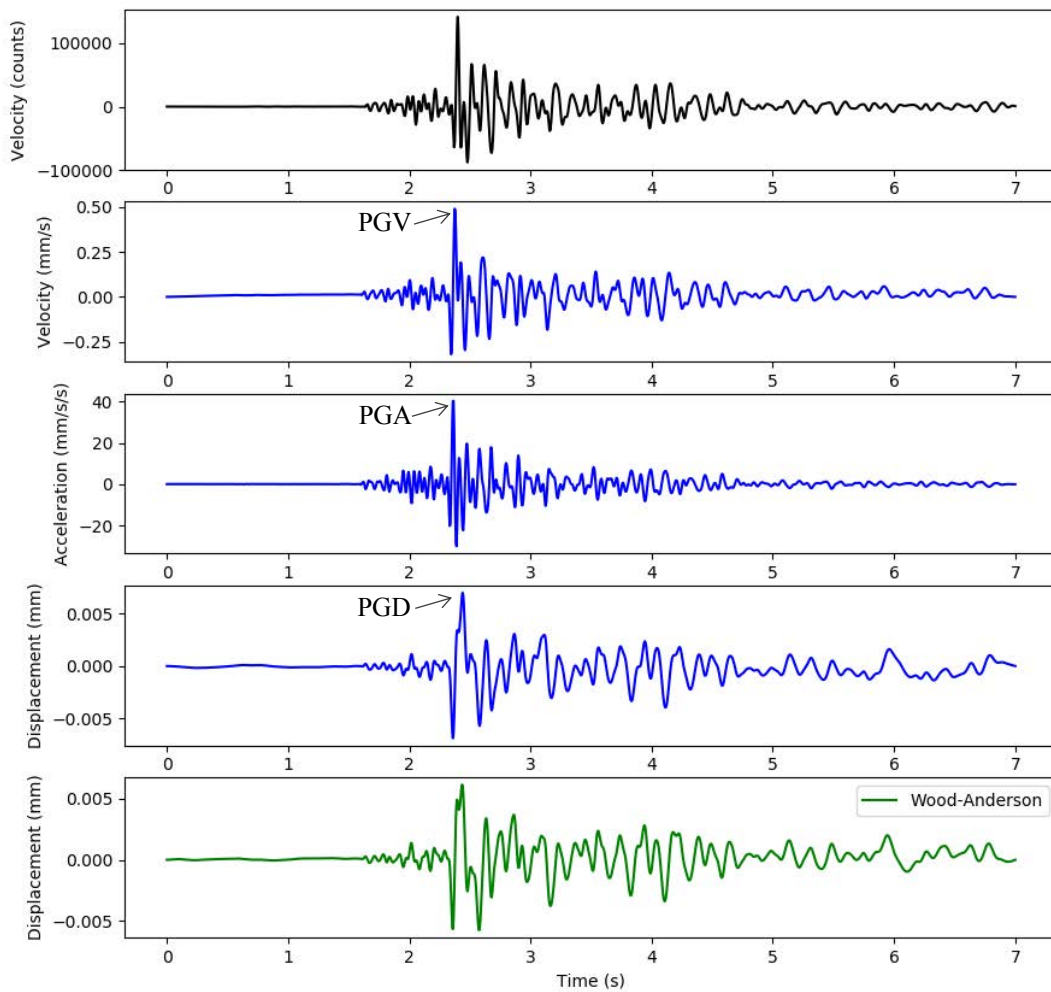


Figure 2.1. Example earthquake (2018-12-11,  $M_L = 1.5$ ) record at PNR site IO1 east-west direction. *Top to bottom*: (i) counts as recorded by datalogger (proportional to velocity); (ii) ground velocity (in mm/s); (iii) ground acceleration (in  $\text{mm/s}^2$ ) through differentiation of the recorded signal; (iv) ground displacement (mm) through integration and finally, (v) displacement (mm) simulated on a Wood-Anderson seismometer (for local magnitude calculation). PGA, PGV and PGD are indicated for this single horizontal component.

### 2.1.1 Peak Displacement, Velocity, Acceleration and Response Spectra

In terms of assessing impact on the built environment, the most common ground motion characteristic used by engineers is peak ground acceleration (PGA). For instance, building codes (which specify the design response over various oscillation periods) are often defined using PGA. For a single orientation (e.g., east-west), PGA, and similarly peak ground velocity (PGV) and displacement (PGD) are simply the maxima of the absolute values of acceleration, velocity and displacement, respectively, recorded at a given site (Figure 2.1). For induced seismicity PGV (often also termed peak particle velocity, PPV) is an important parameter, since it is used to define norms and standards within which acceptable motions are permitted (e.g., BS6472-2: BSI, 2008).

Typically, peak values are defined per recording rather than per orientation. Since recordings of ground motion are 3-component there are various ways of defining the record PGA (and equivalently PGV, PGD). The most common is the geometric mean (equivalent to the

exponentiated arithmetic mean of the natural logarithms or the square root of the product of the absolute values) of the horizontal components or subtle variations of this (e.g., Boore et al., 2006). Other options are used, however, such as maximum of the two horizontal components or the vector product (Edwards and Bommer, 2018). These definitions do not equate directly. For instance, vector mean > maximum of two components > geometric mean of the horizontal components. Care should therefore be taken in comparing measures using different definitions. It should also be noted that in certain instances (generally near the epicentre) the vertical component may have larger peak motions than the horizontal. Horizontal motion is typically of more interest to engineering design due to the fact that most structures are, by design, much more resistant to vertical forces than horizontal ones.

A more complete representation of ground motion in terms of peak amplitudes is provided by the 'response spectrum' (Figure 2.2). This provides the maximum responses at different natural periods of vibration, of which PGA forms one value (at zero period - although often approximated at 0.01 s). The response spectrum represents the peak response of a single-degree-of-freedom (SDOF) system (e.g., mass on a pole), with defined damping (typically 5% of critical), to shaking at its base as defined by the acceleration time-series.

Structures have a natural (or resonant) period (i.e., how it oscillates naturally if displaced at roof level and released): short, stiff structures have a short natural period and high-rise structures have a long-period natural response. A rule-of-thumb to determine the natural period of a building is to divide the number of storeys by 10. Therefore, relating the earthquake response spectrum at the equivalent period to a buildings natural period allows engineers to better evaluate any potential damage. The reader is directed to Bommer (2017) for further information.

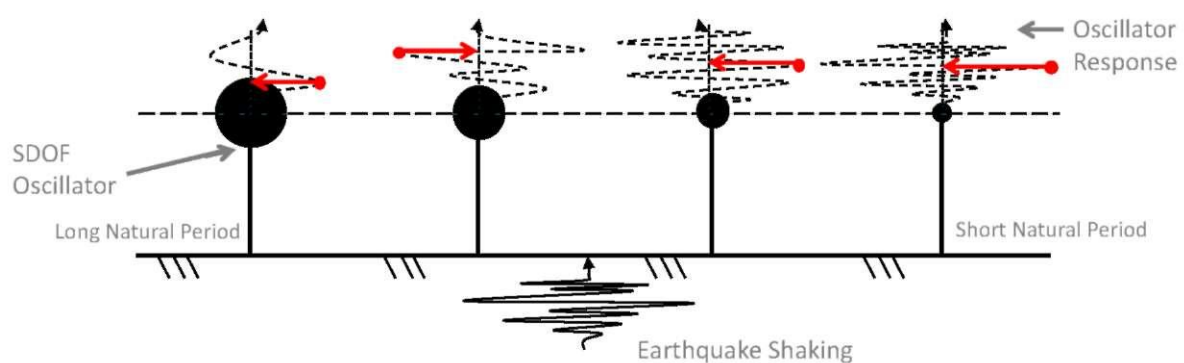


Figure 2.2. Schematic example of response spectra. Shaking occurs at the base. Single-degree-of-freedom (SDOF) damped oscillators of various natural period then respond to this shaking. The response spectrum is comprised of the peak response (red arrows) for each respective natural period.

### 2.1.2 Significant Shaking Duration

While peak motions are important in terms of structural response, high values alone do not necessarily lead to potential damage. For instance, a high PGA associated with a very short signal is associated to negligible displacement since displacement is a double integration (effectively a cumulative sum, twice) of acceleration over time. Similarly, high PGD could be related to a very long duration, which imposes negligible force [for example due to so-called *slow earthquakes* that often occur at subduction zones (Miller et al., 2002) and take place over hours or days]. It is therefore critical to account for duration of shaking in the assessment of seismic risk (Crowley et al., 2017).

Significant duration of shaking is defined in various ways. Typically, the Arias intensity (AI) (cumulative sum of squared acceleration over time) is determined, which can be thought of as a proxy of the energy in a record. Plotting the cumulative value of AI with respect to time, the duration between various intervals with respect to the total AI is then measured (e.g., 5 – 95% or 5 – 75%). Generally, earthquakes follow a predictable pattern in terms of the expected significant duration with a function of magnitude, distance (larger in both cases leads to longer duration) and, to a limited extent, site class or average shear-wave velocity in the upper 30 m ( $V_{s30}$ ). Empirical models exist that provide predictions for various measures of duration (e.g., Kempton and Stewart, 2006; Bommer et al., 2009), however, these tend to be for tectonic events with magnitudes greater than 3. For the very near-source and small magnitude events associated with induced seismicity it may be sufficient to consider the expected source duration itself, as given by simple models of earthquakes (Brune, 1970, 1971; Madariaga, 1976). These models relate the earthquake stress drop (see Section 2.2.4) to their source corner frequency and consequently signal duration.

### 2.1.3 Frequency Content

The frequency content of earthquake ground motions has an important bearing on their effect on structures. As noted previously, all structures have a natural period (the reciprocal of natural frequency) and are therefore sensitive to motions at these frequencies. Earthquake signals have a characteristic frequency amplitude spectrum (FAS: the distribution of amplitudes at various frequencies). The shape of an earthquake acceleration record FAS is approximated by a trapeze, with amplitudes increasing up to a first corner proportional to frequency squared, then flat, followed by an exponential decay at high frequencies (Figure 2.3). The spectral shape is, in general, defined by the first corner frequency, which is proportional to magnitude (Brune, 1970) (Figure 2.3, *right*) and the rate of high-frequency decay, known as  $\kappa$  (Anderson and Hough, 1984), which is proportional to distance (Figure 2.3, *left*).  $\kappa$  is also influenced by site type, with low  $V_{s30}$  sites (e.g., thick sedimentary deposits) leading to strongly damped signals and therefore a high rate of spectral decay. The combination of small magnitudes for induced seismicity and potentially high  $\kappa$  at low  $V_{s30}$  sites means that the characteristic spectral shape of these events is almost identical, only scaled in amplitude by magnitude.

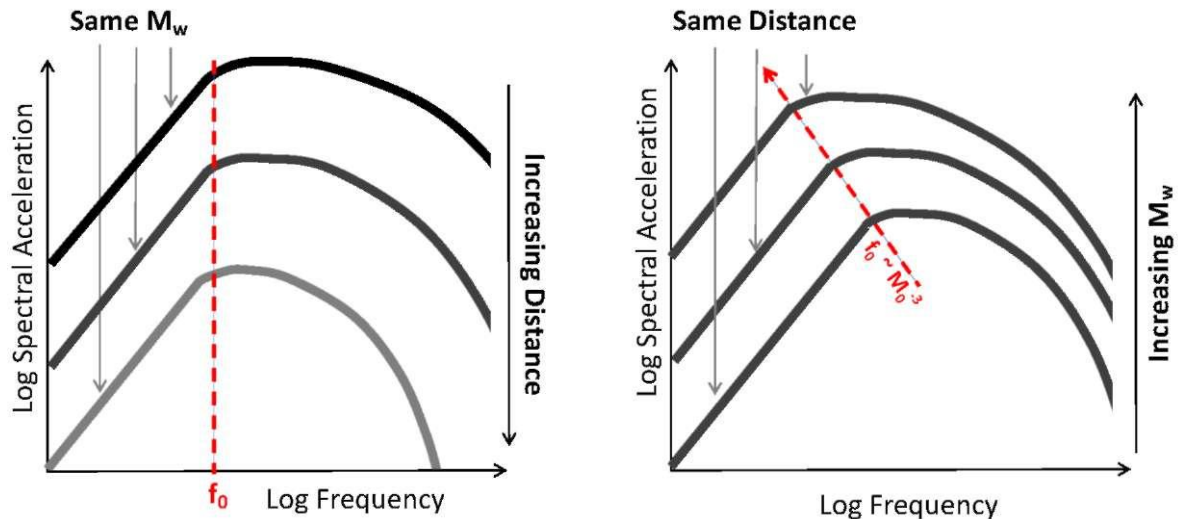


Figure 2.3. Schematic example of frequency content of earthquake records with (left) increasing distance for one event; (right) various magnitude events at the same distance. Note that this example (right) does not consider the effect of strong local damping (e.g., due to thick low velocity sediments), which may lead to a constant *apparent*  $f_0$  independent of earthquake magnitude.

While the ideal spectral shape is fairly simple, in reality the frequency content is more complex and may be influenced by other factors, such as site resonance and earthquake stress drop. The frequency content of earthquake ground motions is inherently included in ground motion prediction equations (see Section 2.3). Any systematic difference in the frequency content of records (e.g., due to particular site resonance effects, or to particularly high or low earthquake stress drop) at a particular location may lead to systematic over- or under-prediction of ground motion amplitudes. This is discussed further in Section 2.2.

#### 2.1.4 Variability

Earthquake ground motions are highly variable due to the complexities of fault rupture, and wave propagation through the heterogeneous subsurface (e.g., Edwards et al., 2019). The variability in ground motion due to this complexity is not captured in median predictions from GMPEs, which are designed to robustly determine ground motions given a set of limited predictor variables (magnitude,  $M$ , depth,  $H$ , distance to site,  $R$ , 30m average shear-wave velocity of site,  $V_{s,30}$ , etc.). Instead GMPEs capture random variability through standard deviations on their predictions. The determination of these standard deviations (aleatory variability) is as important as the median values themselves. The aleatory variability of a GMPE is commonly assumed to be lognormally distributed and split into two parts: between event (with standard deviation,  $T$ ), and within event ( $Q$ ), such that the logarithm of an arbitrary ground motion intensity is given by:

$$\log Y = f(M, R, H, V_{s,30}, \dots) + B(T) + W(Q). \quad (1)$$

For a given intensity measure, e.g., PGV, a single between-event term,  $S(T)$ , is sampled from a zero-mean Gaussian distribution with standard deviation  $T$  (accounting for the average difference of an event's ground motions with respect to the median predictions). Within-event

terms,  $W(q)$ , are event- and site-specific and are sampled from a zero-mean Gaussian distribution with standard deviation  $q$  for each record. Within event terms are assumed to be mainly related to site response/azimuthal variability and are spatially correlated.

### 2.1.5 Spatial Correlation

The variability of earthquake ground motions is spatially correlated. This means that similar deviations in peak motions (with respect to the median prediction) are likely to occur at sites in close proximity to one another. The degree (and length scale) of correlation depends on the complexity of the subsurface and, for locations near to the fault, directivity or radiation pattern effects. In addition, long-period motions (which are less effected by subsurface heterogeneity) are more strongly correlated than short-period motions. Generally, spatial correlation is important when considering aggregated risk (i.e., risk associated to defined groups of people or structures) rather than individual risk (the risk to one individual - who can only be in one place at once). Spatial correlation leads to a smoothing of ground motions over space, which leads to increased likelihood of regional damage patterns, rather than a heterogenous or random distribution. While the correlation of ground motions is region specific (dependent on geology, for instance, e.g., Stafford et al., 2019), usually there are not sufficient data to develop a local model. However, empirical models exist for the spatial correlation of ground motions (e.g., Jayaram and Baker, 2009, Figure 2.4, which is adopted here).

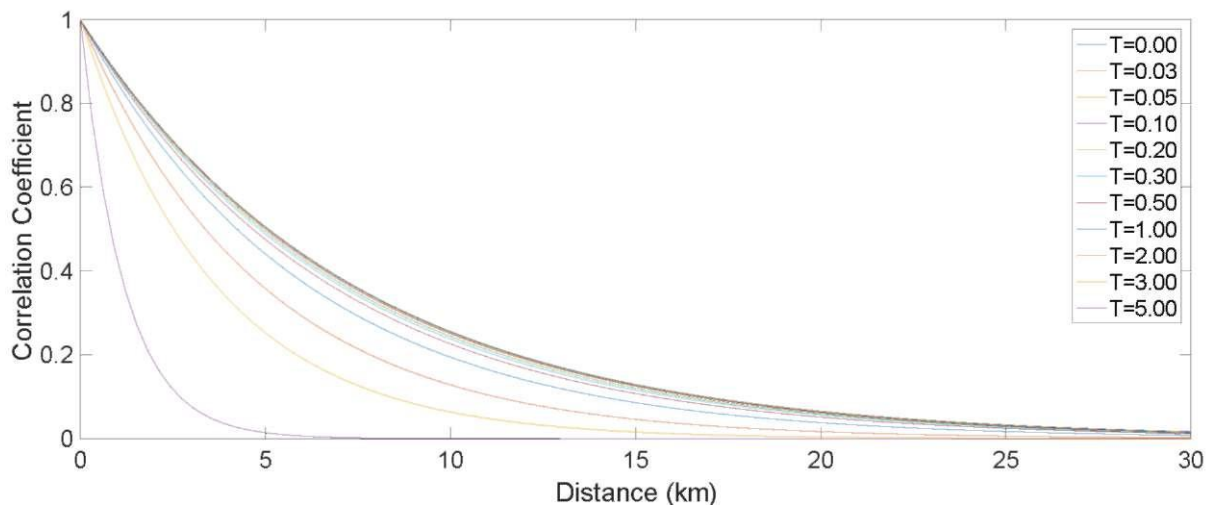


Figure 2.4. Spatial correlation coefficients versus distance for various vibration periods (Jayaram and Baker, 2009).

Where  $v_{s30}$  are expected to show clustering (as at PNR), Jayaram and Baker (2009) propose the correlation coefficient  $\rho$  is given by:

$$\rho = \exp\left(-\frac{3R}{b}\right) \quad (2)$$

where:

$$b = 40.7 - 15T \quad T < 1 \quad (3)$$

$$b = 22.0 - 3.7T \quad T \geq 1 \quad (4)$$

They propose that for application of their model, one should:

1. Obtain median ground-motion values at the sites of interest using a ground motion prediction equation (GMPE);
2. Probabilistically generate the GMPE inter-event term which follows a zero-mean univariate normal distribution;
3. Simulate the location-specific intra-event terms using the standard deviations from the ground-motion models and the respective correlation coefficients (Equation 1);
4. Combine the three terms generated in Steps 1–3 to obtain correlated ground-motions at the sites of interest.

## ***2.2 Factors Influencing Ground Motions***

The main contributors to the strength of earthquake ground motions are:

1. Earthquake magnitude;
2. Distance of site from earthquake source (attenuation);
3. The site's geology, specifically its shear-wave velocity profile;
4. Earthquake rupture properties (e.g., stress drop);
5. Wave propagation effects (e.g., focussing).

### *2.2.1 Earthquake Magnitude*

Earthquake magnitude can be considered the most direct factor influencing earthquake ground motion. An earthquake's magnitude describes its 'size' and works on a logarithmic scale. However, as with any size characterisation, there are a variety of ways that this is performed. Some measures (e.g., moment magnitude, denoted  $\mathbf{M}$  or  $M_w$ ; Hanks and Kanamori, 1979) relate to physical characteristics of the fault (crack) that generated seismic waves (and the resulting surface shaking). Other magnitudes (e.g., local magnitude,  $M_L$ ; Richter, 1935) effectively describe the surface effects (such as the peak ground displacement) normalized to a common reference distance, without consideration of the physical source itself.

$M_L$  is calculated for all located UK earthquakes by the BGS. Recently, the BGS has published an updated  $M_L$  model (Luckett et al., 2018), which is also valid at the very short distances typical for records of induced seismicity.  $M_L$  is based on the 'Wood-Anderson' amplitude, which is the displacement on a (simulated) Wood-Anderson seismograph (see Figure 2.1). Since the majority of GMPEs are based on moment magnitude,  $\mathbf{M}$ , these values must be converted.

Different earthquake magnitude scales ( $M_L$ ,  $\mathbf{M}$ ) are usually calibrated (over a limited range) to be consistent with one another. However, there is no guarantee that they are similar throughout—particularly at the low end ( $M_L < 2$ ) typical in induced seismicity (Edwards and Douglas, 2013; Dost et al., 2018, 2019). For instance, moment magnitude of induced earthquakes ( $M_L < 2$ ) is systematically higher than the local magnitude for a given event. The model of Gruenthal et al. (2009) converts between  $M_L$  and  $\mathbf{M}$  over a wide magnitude range (down to  $M_L$  -0.8, although with limited data below  $M_L$  1). At the low magnitude end the

gradient between  $M_L$  and  $M$  approaches 0.67. Numerous studies have shown consistency with this model (Dost et al., 2018, 2019), although small ( $< 0.1$  unit) region-specific offsets are sometimes apparent (e.g., Edwards et al., 2015). In the  $M_L < 1$  range, Deichmann (2017) showed that  $M \propto 2/3 M_L$  for  $M_L \ll 2$ , confirming the empirical observations.

To convert the  $M_L$  values of the PNR dataset, we therefore assume:

$$\mathbf{M} = 0.0376M_L^2 + 0.646M_L + 0.53 \quad (M_L \geq 2.5) \quad (\text{Gruenthal et al., 2009}) \quad (5a)$$

and

$$\mathbf{M} = \frac{2}{3}M_L + 0.833 \quad (M_L < 1.5) \quad (\text{Edwards et al., 2015}) \quad (5b)$$

with linear transition in the range  $1.5 \leq M_L \leq 2.5$ .

In July 2019 Cuadrilla Resources published their hydraulic fracture plan for PNR-2, this included an analysis of  $M_L$  and  $M$  for the PNR-1z data. They found, in the range  $-0.8 \leq M_L \leq 1.5$  that:

$$\mathbf{M} = 0.655M_L + 0.897 \quad (-0.8 \leq M_L \leq 1.5) \quad (\text{Cuadrilla Resources, 2019b}). \quad (5c)$$

The PNR-1z empirical model (Equation 5c) is remarkably similar to the empirical-theoretical model proposed by Edwards et al. (2015) (based on Deichmann, 2017) and adopted for this work (Figure 2.5) and therefore justifies the use of Equation 5b in the small magnitude range.

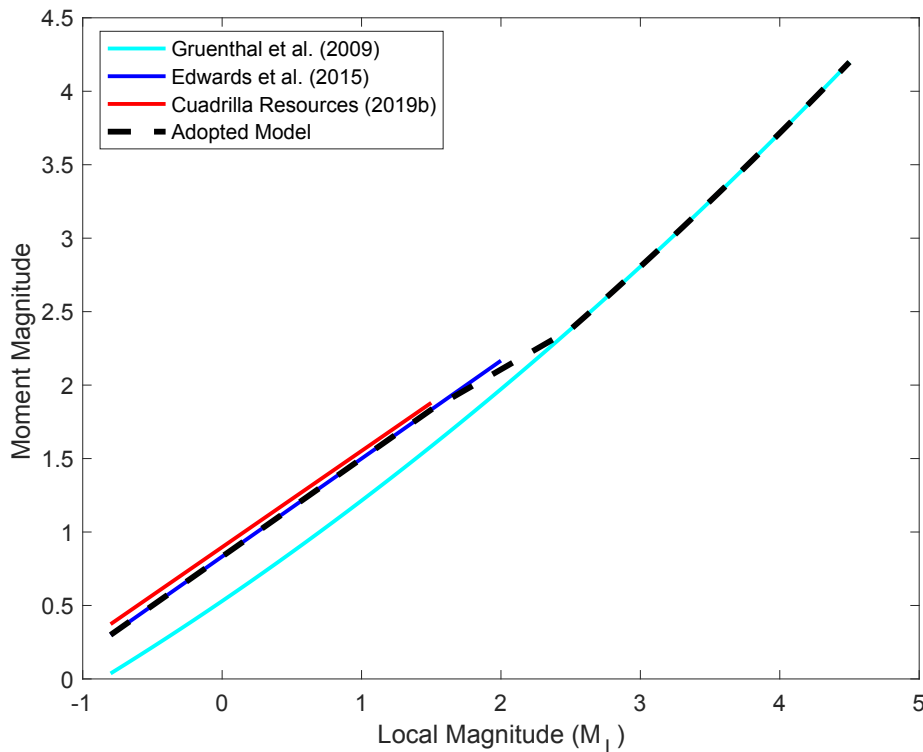


Figure 2.5. Local to moment magnitude conversions.

### 2.2.2 Attenuation

Earthquake ground motions diminish rapidly with distance from the epicentre, as evidenced both instrumentally and through felt intensity (Figure 2.6). This is due to geometrical decay and intrinsic attenuation. Geometrical decay is due to the fact that energy must be preserved over an increasingly large surface as the wavefield propagates away from the source. In a homogeneous medium this means that amplitudes must decrease proportional to distance (if distance doubles, amplitudes half).

Intrinsic attenuation is due to internal friction and scattering leading to frequency-dependent transfer to, for example, thermal energy (Knopoff, 1964). This is usually modelled as an exponential function, such that Fourier amplitudes are attenuated (in combination by geometric and intrinsic effects) by factor  $G$ :

$$G(f) = \exp\left(\frac{-\frac{\pi f R}{\beta Q(f)}}{R^\lambda}\right) \quad (6)$$

where  $R$  is the distance (in km),  $\beta$  is the average shear-wave velocity (typically 3.5 – 3.6 km/s),  $Q$  is the quality factor (a property of the rock) and  $\lambda$  is the rate of geometrical decay (usually in the range 0.5 – 1.5) depending on the wave type and distance. In terms of other intensity measures (PGA, PGV, response spectral ordinates) there is a magnitude dependence on the rate of decay due to a complex interaction of spectral shape and oscillator response, and at larger magnitudes due to near-field saturation as finite-fault effects come into play. This is captured by empirical GMPEs (see Section 2.3). However, all ground amplitude measures decay quickly, with seismic hazard rarely considered for tectonic events ( $M > 5$ ) at distances greater than approximately 200 km. As a result of attenuation any potential for structural damage (European Macroseismic Scale, EMS-98, intensity VII) due to induced seismicity is limited to epicentral regions. It should be noted, however, that site response (see Section 2.2.3) may lead to a local increase in ground motions outside of this general trend.

For induced seismicity, it has been noted that near-field motions tend to decay even more rapidly than  $1/R$  (e.g., Edwards et al., 2019; Atkinson, 2015). This is likely due to the stratified local geology and low  $Q$  materials in the upper layers. Atkinson (2015), for example, presents a model with decay proportional to  $1/R^{1.3}$ . However, one important question is whether this strong decay persists for larger faults associated with damaging events.

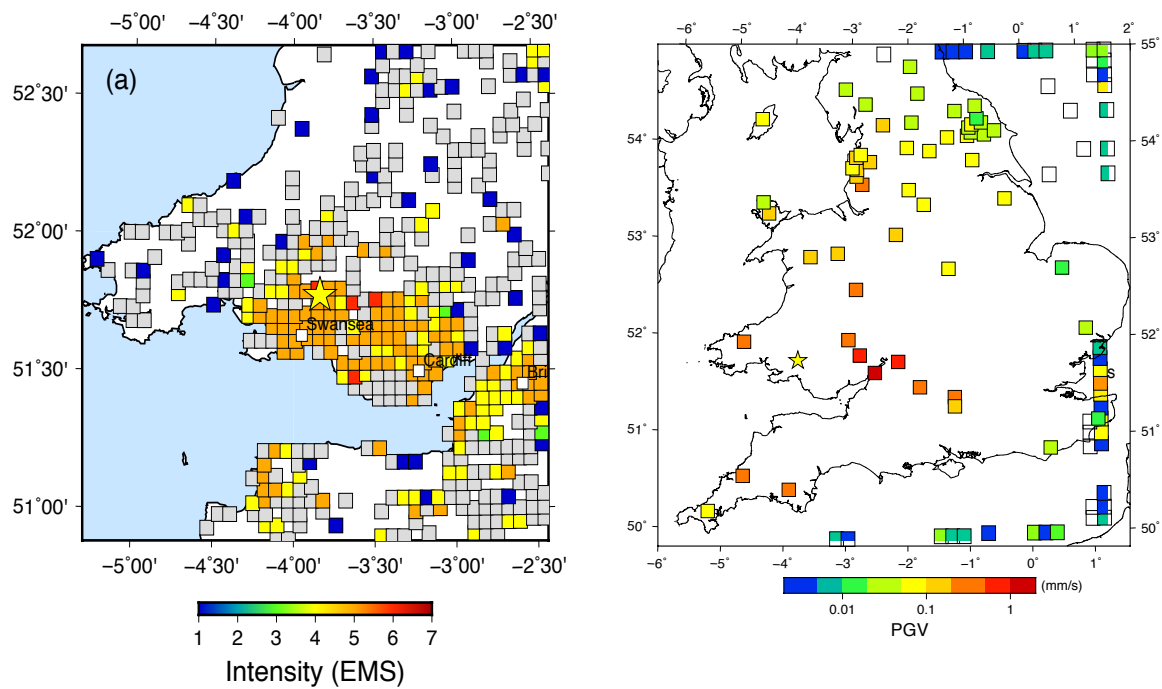


Figure 2.6. Example of ground motion attenuation in terms of (*left*) macroseismic (felt) intensity and (*right*) PGV for the  $M_L$  4.6 earthquake near Cardiff on 17/02/2018. Figure source: BGS.

### 2.2.3 Site Characteristics

The variability of near-surface geophysical properties of the soil and rock layers, primarily shear-wave velocity and to a lesser extent density, have a significant impact on the local ground motion field. The compaction of sediments increases with depth and therefore porosity decreases. As a general rule, therefore, shear-wave velocity and density of geological strata both increase with depth, with the lowest values confined to the uppermost tens to hundreds of metres, depending on the geology of the area. ‘Site effects’ describe the local effect of these uppermost layers of rock and soil on seismic waves propagating through them. While complex, and depending specifically on the subsurface shear-wave velocity and density profiles, the local site effects can be generalised in terms of a layer over halfspace (bedrock), with a defined resonance frequency ( $f_0$ ) that is approximated as:

$$f_{r,0} = \frac{V_s}{4H_B} \quad (7)$$

where  $V_s$  is the average shear-wave velocity of the overlying layer and  $H_B$  is the depth to the bedrock. For instance, for  $V_s = 200$  m/s and  $H_B = 20$  m we expect the fundamental resonance frequency at around  $f_{r,0} = 2.5$  Hz. Multiples then occur at 5 Hz, 7.5 Hz and so on. In application, site effects are often approximated by a ramp function (in the log frequency domain), since theoretical resonance is complicated by heterogeneous subsurface. The ramp broadly increases up to  $f_0$ , then remains constant. The amplitude of this amplification plateau is defined by the shear-wave velocity contrast between the bedrock and the superficial layers above, often using the square-root impedance for vertical incidence (e.g., Boore, 2013):

$$A(f) = \left( \frac{\rho_b V_{s,b}}{\rho_s V_{s,s}} \right)^{0.5} \quad (8)$$

with the impedance given by the product of average density,  $\rho$ , and shear-wave velocity in the layers above (subscript  $s$ ) and below (subscript  $b$ ) a frequency-dependent reference depth. This depth is defined (Joyner et al., 1981) as the quarter-wavelength depth, similar to Equation 7, such that the reference depth above/below which to calculate the averages is defined as:

$$H_s(f) = \frac{V_s}{4f}. \quad (9)$$

This implies that for a site with bedrock  $V_s$  of 2000 m/s and near-surface  $V_s$  of around 200 m/s (density tends to be a minor influence), amplification of the ground-motion field reaches a factor of around 3 on average, although this is usually exceeded locally at frequencies near  $f_0$  for sites with simple layered stratigraphy (Boore, 2013).

In addition to the amplification effect of decreasing seismic velocity toward the surface, a counteractive effect of damping,  $D(f)$ , applies at high frequency (Anderson and Hough, 1984):

$$D(f) = \exp(-\pi f \kappa_0) \quad (10)$$

where  $\kappa_0$  is a site specific damping term, related to  $Q$  (a property defining seismic attenuation per wave cycle). Near surface materials have low  $Q$ , which leads to strong damping of high-frequency motions as they propagate through the upper layers. Lower velocity materials (sediments, soil) lead to stronger damping. The combination of the amplification described above (e.g., Equations 8, 9) and damping effects (Equation 10) lead to an overall site effect approximated by an initial ramp, followed by exponential decay at high frequency. For low-velocity sites we observe strong amplification followed by strong attenuation as frequency increases. For high-velocity sites, we observe limited amplification but also only weak attenuation of amplitude at high frequency.

As a further generalisation for response spectra the upper 30 m average shear-wave velocity has been shown to correlate very well to averages over various depths  $V_{sx}$  and therefore amplification (Boore et al., 2011). As such modern GMPEs are normally constructed using  $V_{s30}$  as a predictor variable, with lower values (in general) leading to stronger predicted motions.

The site amplification discussed above concern what are referred to as linear effects—those independent of the input motion. As such, an amplification factor always applies, regardless of the scenario. In reality we observe that for strong motions on low velocity sites, amplification is typically reduced due to the non-linearity of soil response to shaking (e.g., Sandikkaya et al., 2013). As a result of this, low-velocity soils ( $V_{s30} < 300$  m/s) may lead to weaker amplification (or even de-amplification) for near-source moderate to large magnitude events than higher-velocity soil (the opposite to linear response, described previously). Non-linear effects are

typically included in modern GMPEs and are considered in the analysis presented later in this report.

#### 2.2.4 Earthquake Stress Drop

Earthquakes are typically characterised in terms of their moment magnitude ( $\mathbf{M}$ ), a logarithmic scale that describes the seismic moment ( $M_0$ ) of an event [ $\mathbf{M} = (2/3) \log(M_0) - 6.03$ , in SI units]. Seismic moment itself is defined by the product of average slip, fault area and the shear modulus (the latter being broadly constant within the crust). Therefore,  $\mathbf{M}$  is a static measure and independent of the kinematic or dynamic characteristics of the earthquake itself. For example, an earthquake with rupture area 60 x 15 km, average slip of 1.2m (and shear modulus of 32 GPa for the crust) will always be defined as  $\mathbf{M}$  7. However, in terms of ‘end-member’ possibilities  $\mathbf{M}$  7 events (or equally any large magnitude earthquake) can then be either potentially devastating when slip occurs over seconds to minutes (as ‘earthquake’ is typically understood), or practically unnoticed when a fault (with identical geometric properties) slips over hours or days (as observed for ‘slow’ earthquakes, Miller et al., 2002).

The dynamic stress drop ( $\Delta\sigma$ , the tectonic driving stress minus the dynamic frictional stress) helps us to further characterise a seismic event beyond its moment magnitude, and can be considered a proxy for energy release. The dynamic stress drop during a seismic event has a significant impact on the radiated wavefield. Returning to the previous example we observe  $\Delta\sigma \sim 1$  to 10 MPa for normal (potentially damaging) earthquakes, whereas for ‘slow’ earthquakes (with limited high-frequency energy released) we observe  $\Delta\sigma \sim 0.01$  to 0.1 MPa, two orders of magnitude smaller.

There are various ways of defining stress drop (or stress parameter), but as used in engineering seismology stress parameter effectively it defines the proportion of high-frequency radiated energy for a given magnitude, with higher stress drop events radiating more high-frequency energy (Figure 2.7, *left*). For increasing magnitude events, for a given stress parameter, the source corner frequency ( $f_c$ ), decreases (Figure 2.7, *right*), but magnitude dependent changes in stress parameter may give rise to a change in the reduction of  $f_c$  as magnitude increases.

In terms of response spectral ordinates, increase in stress parameter leads to stronger mid (e.g., PGV) to short period (e.g., PGA) ordinates. Potential regional variations in stress parameter may mean that GMPEs developed in other settings do not correctly predict median motions. Of particular relevance in induced seismicity, it is thought that earthquake stress drop is depth-dependent, with deeper earthquakes leading to higher stress drop. Some recent GMPEs account for this in their predictions (e.g., Chiou et al, 2014), but many do not. Since GMPEs are usually developed using predominantly deep tectonic events, this may lead to an overestimate when applied to shallow induced seismicity.

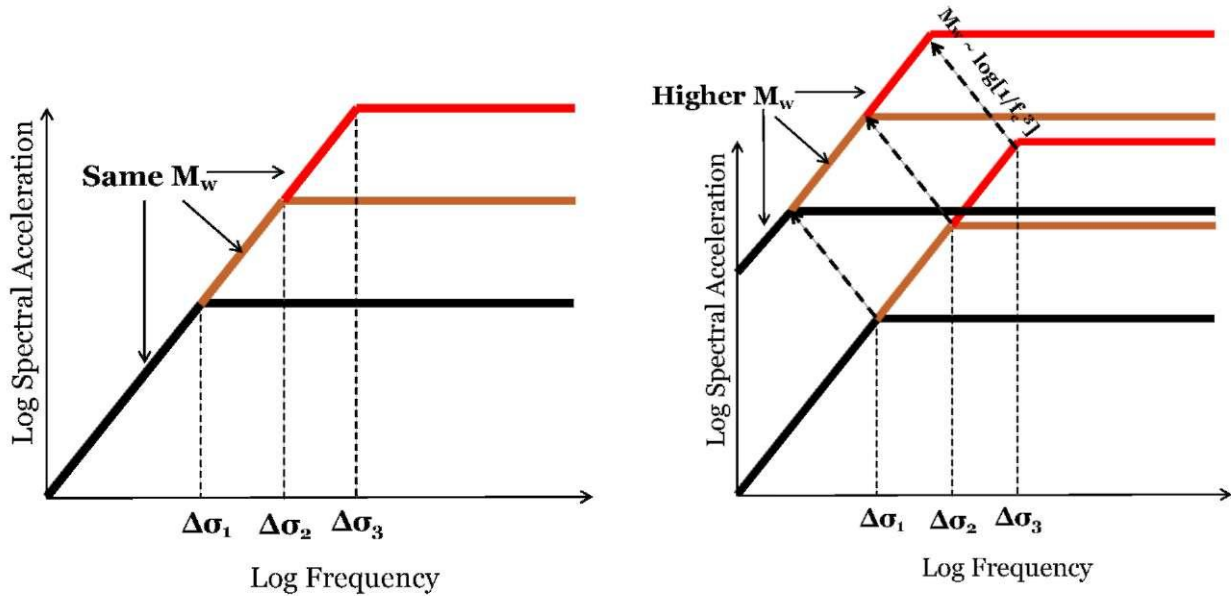


Figure 2.7. Schematic representation of the impact of stress drop (parameter) on Fourier spectral amplitudes.

### 2.3 Prediction of Ground Motions

Ground motions are predicted through ground motion models (GMMs). In its simplest form a GMM is a ground motion prediction equation (GMPE). GMPEs provide a statistical estimate of the expected median ground motion and its standard deviation due to a given earthquake scenario. GMPEs are developed for various ground motion intensity measures. For instance, 5% damped pseudo-spectral acceleration (PSA), which is given by the product of the squared angular frequency ( $\omega^2$ ) and the absolute spectral displacement (SD) of a simple harmonic oscillator, damped to 5% of critical, SD itself, pseudo-spectral velocity (PSV =  $\omega$ SD), peak ground acceleration (PGA) or peak ground velocity (PGV). Each ground motion measure has its own advantages and is selected depending on application.

The form of GMPEs is typically:

$$\log Y = F_{\text{source}} + F_{\text{site}} + F_{\text{site}} + B(T) + W(Q) \quad (11)$$

where Y is a ground motion intensity, predicted in terms of its natural or base-10 logarithm (since ground motion residuals are observed to be log-normally distributed). Units of ground motion provided by GMPEs are not standardized and may be in terms of SI units (m, m/s,  $\text{m/s}^2$ ), CGS units (cm, cm/s,  $\text{cm/s}^2$  or gal) or in units of gravity. A set of recommendations regarding selection of GMPEs (e.g., on functional form) are made by Bommer et al. (2010) and Cotton et al. (2006). Bommer et al. (2010) proposed to exclude GMPEs from probabilistic seismic hazard analyses if:

1. The model is derived for an inappropriate tectonic environment.
2. The model is not published in a Thomson Reuters ISI-listed peer reviewed journal (although an exception can be made for an update to a model that did meet this criterion).

3. The dataset used to derive the model is not presented in a table listing the earthquakes and their characteristics, together with the number of records from each event.
4. The model has been superseded by a more recent publication.
5. The model does not provide spectral predictions for an adequate range of response periods.
6. The functional form lacks either non-linear magnitude dependence or magnitude-dependent decay with distance.
7. The coefficients of the model were not determined with a method that accounts for inter-event and intra-event components of variability; in other words, models must be derived using one- or two-stage maximum likelihood approaches or the random effects approach.
8. Model uses inappropriate definitions for explanatory variables or models site effects without consideration of site characterization, such as  $V_{s30}$ .
9. The range of applicability of the model is too small to be useful for any relevant extrapolations.
10. Model constrained with insufficiently large dataset: fewer than 10 earthquakes per unit of magnitude or fewer than 100 records per 100 km of distance.

However, it should be noted that some of these considerations are not as relevant for induced seismicity. A comprehensive resource of available GMPEs is maintained by Dr John Douglas (University of Strathclyde) and is available online at [gmpe.org.uk](http://gmpe.org.uk) (last accessed 08/2019).

As noted by Bommer and Edwards (2018) there are several important considerations when selecting GMPEs specifically for induced seismicity, summarised here:

- **Magnitude:** due to close proximity to population centres, induced seismicity is typically considered as a risk at smaller magnitude than considered for tectonic seismicity (for the latter generally  $M > 4.5$ ). As a result, many GMPEs are not developed with a suitable range of magnitude and are therefore not technically applicable for induced seismicity. In fact there are very few models valid without adjustment at  $M < 3$ . Several studies have shown that the extrapolation (without adjustment of coefficients and/or functional form) of GMPEs to smaller magnitudes will generally lead to gross over-estimation of the predicted amplitudes (Bommer et al., 2007; Atkinson and Morrison, 2009; Chiou et al., 2010). Magnitude type also has an important impact on the predictions, particularly in the range  $M < 3$  where  $M$  is not equivalent, but proportional to  $0.67 ML$  (Dost et al., 2017). This difference in magnitude type may lead to incorrect conclusions where GMPEs apparently match at low  $M$  when wrongly assuming equivalence.
- **Depth:** induced seismicity tends to occur at shallow depths - at PNR around 2 to 3 km. On the other hand tectonic earthquakes (which the majority of GMPEs are developed with) typically occur at greater depths (around 10 km). Two considerations are necessary here: (i) due to their proximity to the surface they may lead to higher ground motions than for an equivalent tectonic event at greater depth; but counteracting this (ii) due to their shallow depth (and lower confining stress), their stress drop may be lower, leading to lower ground motions than for a deeper event of the same magnitude;

- Distance: hazards due to induced seismicity are focussed in the very-near epicentral region, a region where very little empirical data exists. As for magnitude (above) this means that many GMPEs are not technically applicable and must be extrapolated and/or adjusted beyond their valid range. Accounting for the importance of near-field prediction and the shallow depth sources, it is important to use a distance measure that reflects this such as hypocentral or rupture distance;
- Near source saturation: a common feature of many modern GMPEs is the phenomenon of near-source saturation, which is essentially a flattening of the attenuation curves at short distances. Since this is related to the dimensions of the earthquake source (i.e., fault rupture) the distance saturation is dependent on magnitude, with the flattened part of the attenuation curve extending over greater distances from the source for larger earthquakes. The magnitude dependence of the near-source distance saturation persists for moderate-magnitude earthquakes and it is important that the adopted GMPE is able to correctly model this feature in the magnitude range of applicability for induced seismicity (e.g., Yenier and Atkinson, 2014; Yenier et al., 2016).
- Site classification: GMPEs are typically developed either for a reference site or with a predictor variable that allows different site types to be considered. It is important that the GMPE selected is suitable for the  $V_{s30}$  in the region, since this can lead to significant differences in predictions.
- Other predictor variables: factors such as source mechanism are not considered as important as those above (since they generally lead to relatively minor changes in prediction) and may need to be assumed. It is therefore better to have a simple model form that can be easily adjusted at a later point.

There exist several hundred GMPEs in the literature, with many differences in parameterisation and model form. Based on a study conducted by Arup (Arup, 2014), the ground-motion prediction equation (GMPE) adopted for application at Preston New Road by the operator was the European model of Akkar et al. (2014). Shortcomings with this selection were, however, noted by Bommer and Edwards (2018) and the model is therefore not considered here. Instead, we focus on two GMPEs which are commonly used for predicting ground motions due to induced seismicity: Atkinson (2015) and Douglas et al. (2013). Their parameterisation, model form and consideration of uncertainty is discussed in the following. For more general review of development of GMPEs, the reader is referred to Douglas and Edwards (2016).

The GMPE of Atkinson (2015) was specifically developed for instances of induced seismicity. The model is developed using a high-quality earthquake ground motion database (NGA-West2, Anchetta et al., 2014) comprised of records from tectonic events ( $M$  3 to 6 at distances up to 40 km) worldwide. However, the majority of events for the smaller magnitudes are from tectonic (and not exclusively shallow) Californian earthquakes. The model has the form:

$$\log Y = c_0 + C_1 M + c_2 M^2 + c_3 \log R + B(\tau) + W(\varphi) \quad (12)$$

with  $Y$  the ground motion intensity (PGA, PGV, PSA at given period),  $\mathbf{M}$  is the moment magnitude (not necessarily equivalent to local magnitude) and  $R$  is the distance in km, given by:

$$R = \sqrt{R_{hyp}^2 + h_{eff}^2} \quad (13)$$

where  $R_{hyp}$  is the distance to the earthquake hypocentre and  $h_{eff}$  accounts for near-epicentre saturation of motions. Atkinson proposed two alternatives:  $h_{eff} = \max(1, 10^{-1.72+0.43M})$  and  $h_{eff} = \max(1, 10^{-0.28+0.19M})$ . The latter formulation is suggested by Bommer and Edwards (2018), and is used here. Logarithms are base 10 and the ground motion intensities are in  $\text{cm/s}^2$  for PGA, PSA, or  $\text{cm/s}$  for PGV.  $B(\tau)$  and  $W(\varphi)$  are samples from the log-normal distributions describing the within-event and between-event variability, respectively. The predictions are made for a reference  $V_{s30} = 760$  m/s. Predictions of other site types ( $V_{s30}$  values) is achieved using the site response model of Boore et al. (2014) and the appropriate reference rock  $V_{s30}$  (760m/s for Atkinson, 2015, and 1100 m/s for Douglas et al., 2013). We note that the model of Atkinson (2015) is specifically designed for use with the amplification model of Boore et al. (2014), whereas for the model of Douglas et al. (2013) we are making the assumption that the different reference rock condition can be adjusted through the use of appropriate reference rock  $V_{s30}$ .

Tables of coefficients ( $c_{0-3}$ ) and standard deviations ( $\tau$  and  $\varphi$ ) are provided by Atkinson (2015) based on regression to the dataset used in their study for several ground motion intensity values (PGV, PGA and PSA at selected periods). This GMPE follows a simple functional form, with reference motions implicitly defined at  $\mathbf{M} = 0$  and  $R = 1$  km as  $c_0$ . Quadratic magnitude scaling accounts for the increase of ground shaking with magnitude (the relative increase of motions from one magnitude to the next decreases for increasingly large events due to finite fault size effects).  $c_3 \log R$  accounts for the attenuation of ground motions with increasing distance, and is roughly equivalent to geometrical decay (see Section 2.2.2), with strong decay proportional to  $R^{-1.4}$  at long-periods. It is noted that this decay also includes the effect of the oscillator response and duration at short periods, however, which leads to increased rates of decay. Intrinsic attenuation is not directly considered in this model due to the near-source distances that it is focussed on ( $R_{hyp} < 40$  km). Variability in this model follows the standard form described in Section 2.1.4.

The GMPE of Douglas et al. (2013) is based on a ground motion dataset of shallow induced events (although some related to natural processes). The dataset included events with  $\mathbf{M}$  1 to 4 at distances up to 20 km. The authors produced a homogenised catalogue, with  $\mathbf{M}$  calculated consistently for all events. We use Model 1 of their work (two other models were produced to show the sensitivity of various assumptions). One model was produced without correction for site effects, and one with sites corrected to a reference rock with  $V_{s30} = 1100$  m/s. We present the latter, which can, as for Atkinson (2015), be used for various  $V_{s30}$  sites by using the Boore

et al. (2014) site response model (with  $V_{ref} = 1100$  m/s). The Douglas et al. (2013) model has the form:

$$\ln Y = a + b\mathbf{M} + c \ln R + dR_{hyp} + B(\tau) + W(\varphi). \quad (14)$$

In their model, ground motion units are SI (i.e.,  $m/s^2$  for PGA, PSA or  $m/s$  for PGV). They also use natural logarithms rather than base-10. The main difference in this model to Atkinson's is the lack of  $\mathbf{M}^2$  term. This is because it is based on data below the value where the term has an impact ( $\mathbf{M} > 4$ ). They use the same distance metric (Equation 13), although the  $h_{eff}$  term is period dependent in their model. Douglas et al. (2013) also define an 'intrinsic decay' term ( $d$ ), although at these short distances it is not clear how well resolved this is. Their model uses the standard within- and between-event variability. The values presented are much higher than Atkinson's however. This may be due to the various sources of data used, and potentially poor metadata for site characteristics and small magnitude events.

The above GMPEs are both directly applicable only to rock sites, specifically sites with  $V_{s30} = 760$  (Atkinson, 2015) or  $V_{s30} = 1100$  m/s (Douglas et al., 2013). In order to apply the GMPEs to sites with arbitrary site condition we use the site amplification model of Boore et al. (2014), which is additive to  $\ln Y$  (hence conversion of Equation 13 is required from base-10 logarithms). The linear site term (see Section 2.2.3) is:

$$\ln(F_{s,lin}) = c_{lin} \ln\left(\frac{\min(V_{s30}, V_c)}{V_{ref}}\right) \quad (15)$$

where  $V_{s30}$  is a property of the site under investigation (in m/s),  $c_{lin}$  and  $V_c$  are period dependent coefficients (see Boore et al., 2014) and  $V_{ref}$  is the reference velocity of the GMPE. At high ground motions, ground motion amplification is reduced by non-linearity of the soil, this is described by:

$$\ln(F_{s,nl}) = f_1 + f_2 \ln\left(\frac{PGA_r + f_3}{f_3}\right) \quad (16)$$

with:

$$f_2 = f_4[\exp\{f_5(\min(V_{s30}, 760) - 360)\} - \exp\{f_5(760 - 360)\}] \quad (17)$$

where  $f_{1-2}$  and  $f_{4-5}$  are period dependent coefficients defined in Boore et al. (2014) and  $PGA_r$  is the PGA value predicted for the relevant scenario ( $\mathbf{M}$ ,  $R$ , etc.) for a site with  $V_{ref} = 760$  m/s.

Notable here is that the GMPE of Atkinson (2015) is developed using  $\mathbf{M} > 3$  events and therefore not directly applicable to the seismicity at PNR. The Douglas et al. (2013) model is based on  $\mathbf{M} > 1$  data, so closer to the magnitude range of interest, but it is based on a mixture of various data sources with potentially poor quality metadata leading to high model variability.

The Atkinson (2015) model does not account for potentially lower stress drop events at shallow depth (being based on tectonic events at greater depth) and may therefore overestimate motions. The Douglas et al. (2013) model is based on shallow seismicity, so should implicitly account for this effect, however, its applicability at  $M > 4$  is limited by the lack of  $M^2$  term in the functional form and the fact that it did not use data in this range during development.

#### 2.4 Relationship between Ground Motions and Macroseismic Intensity

Instrumental ground motions (such as PGV, PGA, etc) and macroseismic intensity (which is a measure of quantifiable effects on people and structures) are inherently linked. Very broadly, one cannot increase macroseismic effects without increasing the underlying ground motions. Models exist which equate ground motions with macroseismic intensity and are referred to as ground motion to intensity conversion equations (GMICE).

##### 2.4.1 Macroseismic Intensity

Macroseismic intensity defines the effects of an earthquake on people and the built environment. The European Macroseismic Scale (EMS-98) defines a homogenised intensity scale used across Europe (Table 2.1). It is, however, broadly equivalent to macroseismic scale used in the US (Modified Mercalli Intensity, MMI).

The United States Geological Survey (USGS) uses *ShakeMap* (Wald et al., 2005; García et al., 2012) to visualise the spatial extent of felt effects (Figure 2.8). ‘Weak’ shaking (intensity II-III) is rarely reported by the public following a detected event. Light shaking (intensity IV, no damage) may be reported and corresponds to velocities exceeding 14 mm/s (Worden et al., 2012). Damage is predicted for moderate shaking (intensity V) and above, with velocities exceeding 47 mm/s.

Linking ground motion and macroseismic intensity at low intensities is complicated by the fact that felt intensity is typically biased upwards (people less often report not feeling a seismic event). Some ambiguity is also present in the definition of macroseismic intensity, with for instance, the Italian MCS scale typically leading to higher assigned values.

PERCEIVED SHAKING	Not felt	Weak	Light	Moderate	Strong	Very strong	Severe	Violent	Extreme
POTENTIAL DAMAGE	none	none	none	Very light	Light	Moderate	Mod./Heavy	Heavy	Very Heavy
PEAK ACC.(%g)	<0.05	0.3	2.8	6.2	12	22	40	75	>139
PEAK VEL.(cm/s)	<0.02	0.1	1.4	4.7	9.6	20	41	86	>178
INSTRUMENTAL INTENSITY	I	II-III	IV	V	VI	VII	VIII	IX	X+

Figure 2.8. USGS *ShakeMap* legend indicating shaking levels, Modified Mercalli Intensity (labelled instrumental intensity), and peak motions based on Worden et al. (2012). Note that intensity and corresponding PGA and PGV values differ to those adopted later in this report (see Caprio et al., 2015).

Table 2.1. Abbreviated European Macroseismic Scale (EMS-98)

<b>EMS intensity</b>	<b>Definition</b>	<b>Description of typical observed effects (abstracted)</b>
I	Not felt	Not felt.
II	Scarcely felt	Felt only by very few individual people at rest in houses.
III	Weak	Felt indoors by a few people. People at rest feel a swaying or light trembling.
IV	Largely observed	Felt indoors by many people, outdoors by very few. A few people are awakened. Windows, doors and dishes rattle.
V	Strong	Felt indoors by most, outdoors by few. Many sleeping people awake. A few are frightened. Buildings tremble throughout. Hanging objects swing considerably. Small objects are shifted. Doors and windows swing open or shut.
VI	Slightly damaging	Many people are frightened and run outdoors. Some objects fall. Many houses suffer slight non-structural damage like hair-line cracks and fall of small pieces of plaster.
VII	Damaging	Most people are frightened and run outdoors. Furniture is shifted and objects fall from shelves in large numbers. Many well built ordinary buildings suffer moderate damage: small cracks in walls, fall of plaster, parts of chimneys fall down; older buildings may show large cracks in walls and failure of fill-in walls.
VIII	Heavily damaging	Many people find it difficult to stand. Many houses have large cracks in walls. A few well built ordinary buildings show serious failure of walls, while weak older structures may collapse.
IX	Destructive	General panic. Many weak constructions collapse. Even well built ordinary buildings show very heavy damage: serious failure of walls and partial structural failure.
X	Very destructive	Many ordinary well built buildings collapse.
XI	Devastating	Most ordinary well built buildings collapse, even some with good earthquake resistant design are destroyed.
XII	Completely devastating	Almost all buildings are destroyed.

#### 2.4.2 Ground Motion to Intensity Conversion Equations

In order to convert between instrumental ground motion and macroseismic intensity we use GMICE. Due to the significant variability and scatter in both ground motion and macroseismic intensity data, the development of median models is not straightforward. The most common GMICE used in the US is Worden et al. (2012), which predicts MMI. Other recent European models include the Italian based model of Faenza and Michelini (2010). However, the latter use MCS intensity, which—while by definition broadly comparable with EMS-98 and MMI—has been shown to consistently lead to higher intensities assignments than other scales Musson et al. (2010).

Recent work by Caprio et al. (2015) has compiled various datasets (EMS-98, MMI and MCS) based on both expert assignments and from the “Did You Feel It?” public questionnaires and defined a regional and global GMICE. This model is reversible due to consideration of errors in both ground motion and intensity, with a generic (scale independent, EMS-98 equivalent) intensity defined as:

$$\begin{aligned} I &= a_1 + b_1 \log_{10} PGM & \log_{10} PGM &\leq t_{PGM} \\ I &= a_2 + b_2 \log_{10} PGM & \log_{10} PGM &> t_{PGM} \end{aligned} \quad (18)$$

where PGM is peak ground motion (largest of two horizontal components of either acceleration or velocity, PGA, PGV, respectively). The coefficients for Equation 18 are in Table 2.2.

Table 2.2. Coefficients for the global GMICE of Caprio et al. (2015), Equation 18.

<b>PGM</b>	<b><math>a_1</math></b>	<b><math>b_1</math></b>	<b><math>a_2</math></b>	<b><math>b_2</math></b>	<b><math>t_{PGM}</math></b>
PGA (cms <sup>-2</sup> )	2.270	1.647	-1.361	3.822	1.6
PGV (cms <sup>-1</sup> )	4.424	1.589	4.018	2.671	0.3

Since no UK-specific GMICE exists, we adopt the global model of Caprio et al. (2015) for the analyses later in this report. Macroseismic intensity (estimated from GMICE) provides a useful first order estimate of potential effects of scenario earthquakes. However, it is no replacement for a full investigation in terms of building stock and its vulnerability (see Section 2.6).

### ***2.5 Impact of Ground Motion Levels on People***

Ground motions can cause a nuisance to people even if they do not affect structures themselves. Here we consider these low-level ‘nuisance’ ground motions, while stronger motions are considered in the subsequent section. While ground motions that do not cause damage to buildings could be considered relatively benign, it is well known that continuous or repeated levels of vibration can cause a nuisance to the local populations and are actively avoided in various industries. A convenient way to assess the impact of induced seismicity on people’s wellbeing is to compare vibration levels to existing British Standards (which define acceptable levels for industry) and other anthropogenic sources (such as road traffic, construction, etc).

British Standard ISO 4866 (BSI, 2010) provides “extreme” examples of typical vibration sources (Table 2.3). It is noted that the values “refer to the response of structures and structural elements to a particular type of excitation and are indicative only”. Furthermore, while the source of these vibrations, in most cases, releases less energy than that released by an earthquake, the felt vibration (the amplitude of shaking) at the surface can be equated. The key difference is that earthquakes at depth disperse energy over a wide area—subjecting a large volume (and surface area) to vibration—while many other sources of vibration are more localised.

British Standard 5228-2 (BSI, 2014) states that the threshold of human perception is typically in the PGV range of 0.14 mm/s to 0.3 mm/s, well below any damage levels. However, we note

that this is below the levels typically associated to felt seismicity (e.g., Bommer et al., 2006). This may be due to the definition of perceived, where the activity being undertaken by the person will have an impact. We therefore presume the threshold in BS 5228-2 applies for a person in a quiet environment with no other noise disturbances. For instance, typical traffic induced vibrations are within this range [around 0.2 mm/s according to Edwards et al. (2018), or even higher according to British Standard 4866 (BSI, 2010)], and are not something that we would consider perceivable within the context of a person going about their day-to-day life.

Other impacts on people may be related to the impact of ‘sight and sound’ as well as vibration, with larger seismic events often being reported as ‘loud bangs’ or ‘crashes’. For instance, a recent  $M_L$  2.2 event in Cornwall (8<sup>th</sup> August 2019) was reported as a “sonic boom” or a “loud bang from beneath” according to news reports. The USGS (<https://earthquake.usgs.gov/learn/topics/booms.php>, last accessed 08/2019) note that “small shallow earthquakes sometimes produce rumbling sounds or booms that can be heard by people who are very close to them. High-frequency vibrations from the shallow earthquake generate the booming sound; when earthquakes are deeper, those vibrations never reach the surface. Sometimes the earthquakes create booming sounds even when no vibrations are felt.” Due to the shallow depth of induced seismicity (and generally higher frequency content due to their small magnitude—see Section 2.1.3), these events are therefore more likely to produce audible sound waves that can be heard at the surface.

The combination of possible felt (but non-damaging) and heard effects of induced seismicity certainly are cause for concern to the local population. Residents may be frightened by such effects and may be particularly concerned about the possibility of future, stronger events.

Table 2.3. Typical frequency, amplitude, velocity and acceleration levels as listed in BS ISO 4866:2010 (BSI, 2010). The lower and upper (corresponding to the amplitude range) equivalent local magnitudes (for vibrations at the epicentre with event depth at 2.5 km) has been calculated according to the updated (Luckett et al., 2018) BGS  $M_L$  scale used for the TLS.

	<b>Frequency range Hz</b>	<b>Amplitude range <math>\mu\text{m}</math></b>	<b>Particle velocity mm/s</b>	<b>Particle acceleration m/s<sup>2</sup></b>	<b>Magnitude <math>M_L</math> (low)</b>	<b>Magnitude <math>M_L</math> (high)</b>
<b>Traffic (road, rail)</b>	1 to 100	1 to 200	0.2 to 50	0,02 to 1	0.7	3.0
<b>Blasting vibration</b>	1 to 300	100 to 2 500	0.2 to 100	0.02 to 50	2.7	4.1
<b>Air over pressure</b>	1 to 40	1 to 30	0.2 to 3	0.02 to 0.5	0.7	3.0
<b>Pile driving</b>	1 to 100	10 to 50	0.2 to 100	0.02 to 2	1.7	2.4
<b>Machinery outside</b>	1 to 100	10 to 1 000	0.2 to 100	0.02 to 1	1.7	3.7
<b>Machinery inside</b>	1 to 300	1 to 100	0.2 to 30	0.02 to 1	0.7	2.7
<b>Human activities inside</b>	0.1 to 30	5 to 500	0.2 to 20	0.02 to 0.2	0.7	3.4

## ***2.6 Impact of Ground Motion Levels on the Built Environment***

This Section provides a summary of the impact of past events (induced and tectonic) with a magnitude of up to 4.8 (which is slightly higher than the largest scenario considered in Section 6), and with relatively similar building stock and socio-economic settings to those found in the United Kingdom (see Section 5.3). This summary has been taken from a report describing 21 case studies of damaging low to moderate magnitude events by Nievas et al. (2019) which was developed as part of the extensive studies into the impact of gas production in the Groningen field in the northern Netherlands. Readers are thus referred to that report for more detailed information on the events that are presented herein.

The damage states mentioned in the following and in the table below refer to the EMS-98 damage scale (Gruenthal, 1998) which describes 5 damage states for unreinforced masonry (URM) buildings (see Figure 2.9), where the first damage grade (damage state 1, DS1) refers to no structural damage and slight non-structural damage which is manifested through hairline cracks in walls and damage to plaster. The second damage grade (DS2) describes the initiation of structural damage, with cracks in many walls, many pieces of plaster falling and some partial collapse of chimneys. The third damage grade (DS3) corresponds to moderate structural

damage wherein most walls have large and extensive cracks, roof tiles may detach, chimneys fracture at the roof line, and non-structural elements such as partition walls of gable walls may fail. Damage grade 4 (DS4) occurs when very heavy structural damage is present, with serious failure of walls, and partial structural failure of roofs and floors. Finally, at damage grade 5 (DS5) total or near total collapse of the building is experienced.

The following events with magnitude less than 4.8 have been selected from the study by Nievas et al. (2019):

- M3.2 Basel earthquake, Switzerland
- M3.5 Huizinge earthquake, the Netherlands
- M3.6 Darmstadt earthquakes, Germany
- M3.9 Ischia earthquake, Italy
- M4.0 Folkestone earthquake, United Kingdom
- M4.8 Guy-Greenbrier (Arkansas) earthquake, USA
- M4.8 Liège earthquake, Belgium
- M4.8 Épagny-Annecy earthquake, France
- M4.8 Tbilisi earthquake, Georgia

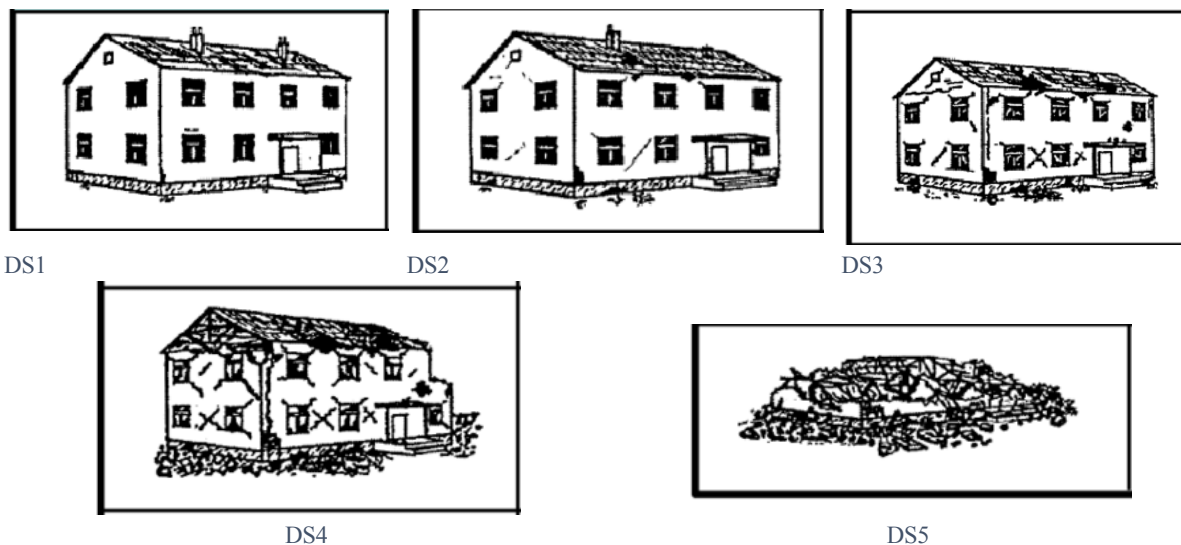


Figure 2.9. EMS damage grades for URM buildings (Grunthal, 1998). DS1: non structural damage, such as hairline cracks in plaster; DS2: initiation of structural damage, with cracks in many walls; DS3: moderate structural damage wherein most walls have large and extensive cracks; DS4: very heavy structural damage is present, with serious failure of walls, and partial structural failure of roofs and floors; DS5: near total collapse.

Three of these events led to large numbers of destroyed buildings and casualties directly attributable to the ground shaking (Ischia, Liège, and Tbilisi). In the case of Ischia and Tbilisi this can be attributed to the high vulnerability of the buildings due to poor quality materials, lack of maintenance and illegal construction. In Ischia the intensity of ground shaking was higher than expected for the event magnitude due to the shallowness of the event and site amplification due to the unconsolidated volcanic deposits. In Liège, the extensive mining exploitation that had taken place in the region for many years may have destabilised the zone and weakened the buildings. Extensive damage (though without any casualties) was observed in Épagny-Annecy, most likely due to increased site amplification within the Annecy basin. All of the above events had maximum macroseismic intensities of VII and VIII.

The remaining events (Basel, Huizinge, Darmstadt, Folkestone, and Guy-Greenbrier) had maximum intensities of V and VI. The Guy-Greenbrier event had a maximum intensity of V which is lower than would be expected for a M4.8 event, and this was likely to be due to the scarce population in the region that was hit and the presence of light wood frame buildings (although strictly, intensity assignment accounts for such factors), though the masonry buildings that were damaged did reach damage state 2 (DS2). The Basel event, which also had a maximum intensity of V, had many damaged buildings, but they were found to correspond to DS1. The other two events (Darmstadt and Folkestone) had a maximum intensity of VI and were mainly characterised by collapsed chimneys in addition to masonry buildings with DS2.

A comparison between the damage estimates made for the scenario events at PNR and these damaging earthquakes is made later in this report.

Date and Time (UTC)	Place	M	Depth (km)	Maximum Intensity	Induced tectonic /	Deaths (due to shaking)	Injured (due to shaking)	Buildings damaged	Buildings destroyed	Losses (10 <sup>6</sup> USD)	Comments
08/12/2006 16:48	Basel, Switzerland	3.2	5.0	V (EMS-98)	Induced (water injection)	0	0	40 – 2000 (based on damage claims)	0	6.5 – 8.3	Creaking of woodwork and rattling of doors and windows alarmed the population. Most damage was cracked plasterwork of brick masonry buildings (DS1)
12/08/2012	Huizinge, the Netherlands	3.5	3.0	VI (EMS-98)	Induced (gas extraction)	0	0	2000 (based on damage claims)	0	Not available	Majority of damage was cracked plasterwork of brick masonry buildings (DS1), mainly in older farmhouse buildings. Damage numbers based on claims rather than evaluation of the damage (which may also have been due to settlement due to soft soils).
17/05/2014 16:46	Darmstadt, Germany	3.6	5.0	VI (EMS-98)	Tectonic	0	0	154	0	1.36	Dislodged, cracked or partially collapsed chimneys (36), dislodged roof tiles, cracked plasterwork (about 27% with DS1 and 7% with DS2).
21/08/2017 18:57	Ischia (Napoli), Italy	3.9	1.7	VIII (EMS-98)	Tectonic	2	39-42	349 - 1000	688	8 - 140	Very shallow event with localised high intensity in a hilly area with unconsolidated volcanic deposits leading to high amplification of ground motions. A handful of collapsed (DS5) buildings (leading to 1 death) and many buildings with significant diagonal cracking and chimney failure (DS3). The other death was due to falling cornice of a church. Building stock reported to have had many illegal extensions and poor-quality materials.
28/04/2007 07:18	Folkestone, United Kingdom	4.0	5.3	VI (EMS-98)	Tectonic	0	1	807 - 1300	0	60	Minor head injury due to falling masonry. Dislodged, cracked or collapsed chimneys, dislodged roof tiles (DS1-2), cracked plasterwork (DS1). Many chimneys were in need of repointing

Date and Time (UTC)	Place	M	Depth (km)	Maximum Intensity	Induced tectonic /	Deaths (due to shaking)	Injured (due to shaking)	Buildings damaged	Buildings destroyed	Losses (10 <sup>6</sup> USD)	Comments
											before the event. Pre-existing flood and settlement damage may also have been present.
28/02/2011 05:00	Guy-Greenbrier (Arkansas), USA	4.8	3.8	V (MMI)	Induced (wastewater injection)	0	0	14	0	1.0	Scarcely populated area led to reduced number of damaged buildings (brick masonry), cracked walls, doorframes out of plumb (DS2). Light wood frame buildings are common in the building stock, which may also have helped reduce the extent of damage.
15/07/1996 00:13	Épagny-Annecy, France	4.8	4.0	VIII (MSK64)	Tectonic	0	1	11,800	3	70-100	High intensity attributed to site amplification in the Annecy basin. Injury due to broken glass, panic of locals due to low seismic risk awareness. Dislodged, cracked or collapsed brick chimneys (600), dislodged roof tiles, cracked plasterwork (DS 3-4).
08/11/1983 00:49	Liège, Belgium	4.8	5.8	VII (EMS-98)	Tectonic	1	25-30	13,000 – 16,000	25 - 205	50 - 80	In a region of extensive mining exploitation which may have destabilised the zone and weakened the buildings. Death due to a falling ceiling, injuries due to falling masonry elements as people fled the buildings. Collapse of chimneys, roofs and walls (DS4-5) of some older masonry buildings, though most experienced DS3.
24/11/2004 22:59	Tbilisi, Georgia	4.8	6.0	VII-VIII (EMS-98)	Tectonic	4	30-70	11,780 – 50,000	2319 - 4208	180 - 350	Deaths due to falling debris (3) and collapse of a roof (1). Extensive damage to low-rise brick and stone buildings (low quality construction and lack of maintenance of buildings observed). Series of aftershocks, continuous heavy rains and snowfalls caused additional damage.

### 3. Ground Characterisation at PNR

As summarised in previous sections, the  $V_{s30}$  value of a site is a critical predictor of the degree of local amplification to ground motions. Predictions of spectral ordinates can increase by up to factors of 3 or more for the lowest  $V_{s30}$  sites, compared to a rock reference site. It was considered a fundamental first step in this work, therefore, to estimate an appropriate value for the PNR sites—both at the locations of seismometer instruments—and more generally, across the local region.

#### 3.1 Site Characterisation Measurements Undertaken at PNR

To determine appropriate  $V_{s30}$  we have undertaken three measurement campaigns (sites L001, L003 and L009). The technique used to determine shear-wave velocity depth-profiles and subsequently  $V_{s30}$  was multi-channel analysis of surface waves (MASW, Miller et al., 1999).

MASW is a non-invasive geophysical method to determine the subsurface structure of the upper tens of metres of soil and rock. Surface waves generated by a seismic source (a hammer strike) using a line of geophones are recorded (Figure 3.0). From the dispersion of these waves as they travel we can determine shear-wave velocity,  $V_s$ , (and to a lesser extent compressional velocity,  $V_p$ ) of the subsurface.

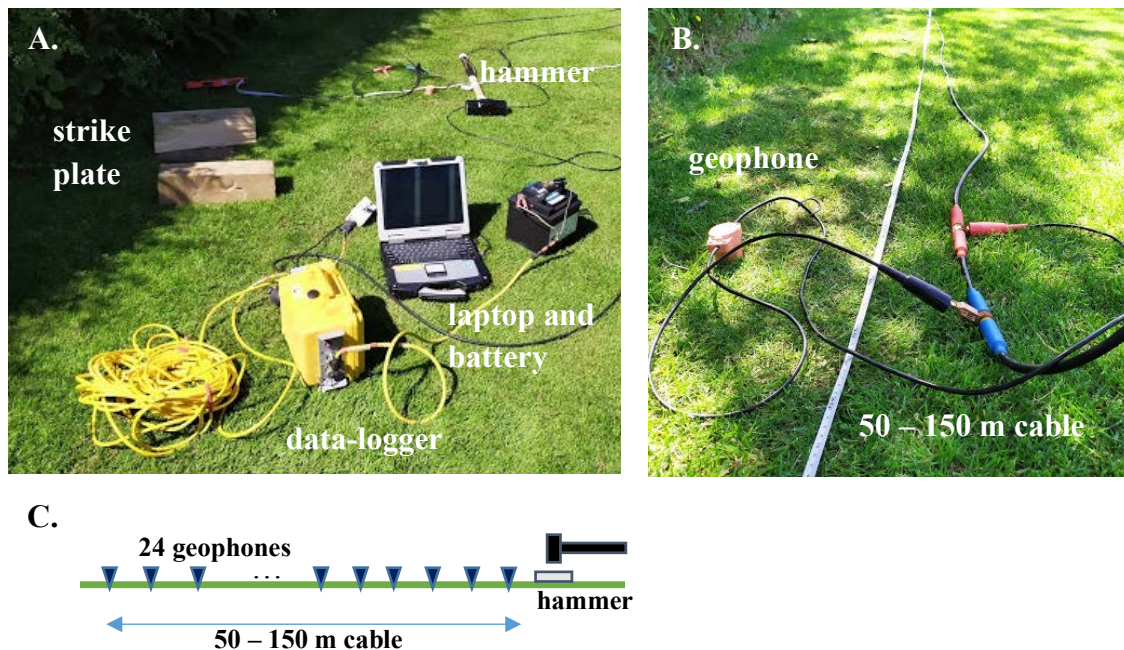


Figure 3.0. A. Equipment used for MASW survey; B. geophone cable array; C. Schematic of MASW layout.

For the MASW surveys we use standard seismic refraction survey equipment:

- A 6.4 kg sledge hammer (used to hit the strike plate and generate a seismic signal)
- A strike plate (a 30 cm square HDPE plate, which is placed at various locations along the survey line)
- A field laptop computer and data-logger

- 50 – 150 m geophone cable (laid on the ground surface)
- 24 vertical 4.5 Hz geophones.

For planning and deployment of the MASW measurements we follow the guidance detailed in Foti et al. (2017). The dispersion of seismic surface waves is determined through cross correlation of the recorded data, as described by Miller et al. (1999). In all cases either 1 or 2 second post-trigger records (at sample intervals of 0.00625 and 0.0125 s respectively) were taken, depending on the record length required to capture the full surface-wave train during the survey. Processing of the collected data for dispersion characteristics is performed in the software package ‘geopsy’ ([www.geopsy.org](http://www.geopsy.org), last accessed 08/2019). A model for the subsurface velocity ( $V_p$  and  $V_s$ ) is then generated through inversion that explains the dispersion behaviour of the Rayleigh waves using the software ‘d inver’ (Wathelet, 2008, Wathelet et al., 2004).

The strategy for measurement in the short timeframe available here was to target specific superficial geology that is present in the area. The predominant superficial deposits near to the PNR site are: (i) blown sand; (ii) till; and (iii) peat and alluvium. Space and landowner consent also played a role in the choice of measurement sites. The selected sites cover the appropriate geological zones (i – iii), allowing a certain degree of inference as to the  $V_{s30}$  for a given superficial geology.

### 3.1.1 Site L001

Site L001 lies on till deposits (Figure 3.1) according to the BGS superficial geology map and is less than 5 km from the PNR site and associated seismicity. Several borehole lithological logs are available within 1 km of this site (Figure 3.2). We use logs 1419 and 18458993 as the nearest open access logs obtained through the BGS single onshore borehole index (SOBI) database. These are shown in Appendix A. SOBI: 1419 indicates till deposits (sand, gravel, clay) to 29 m, overlaying mudstone, while SOBI: 18458993 (although less detailed) also documents clay, sand and gravel deposits to 35 m, overlaying mudstone. Therefore, sites in this area comprise of around 30 m of sand, gravel and clay overlying a more consolidated mudstone.

Data provided by the operator (Figures 3.3, 3.4) from both refraction low velocity later (LVL) analyses and borehole investigations indicates the depth of a first refractor at between 4.5 and 11.9 m. Based on the lithological logs, this is likely to be a transition between clay and sand layers rather than the deeper mudstone. More distant survey points from the same analyses indicate a second refractor resolved at between 17 - 30 m depth, although at most survey locations LVL investigations were unable to resolve to this depth.

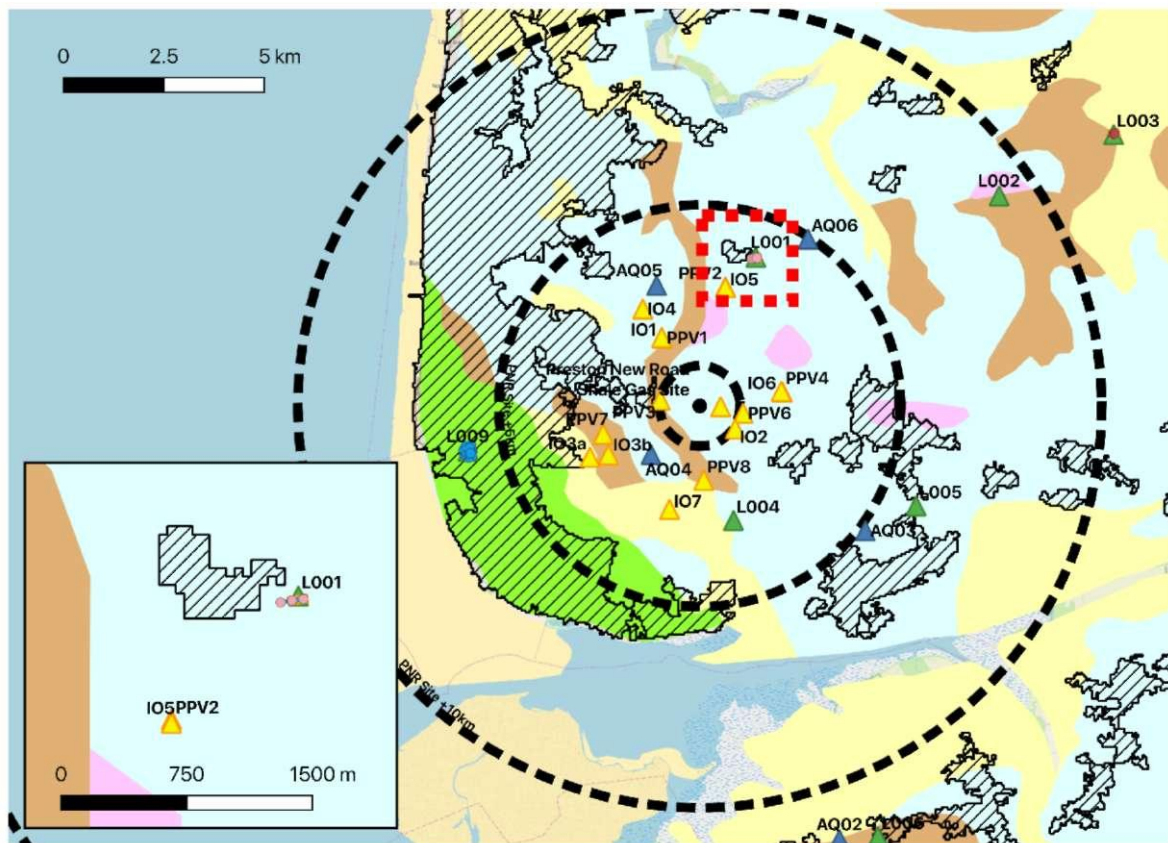


Figure 3.1. Location of MASW measurement at L001 (red dashed square). The PNR site along with 3, 5, 10 km zones around it are shown (dashed concentric rings). The base-map is the BGS 625k superficial deposit map: green is blown sand; light blue is till; brown is peat and cream is alluvium. Built up areas are highlighted by cross-hatched regions. Inset: Location of MASW measurement points (circles) and surrounding region.

Two MASW lines were measured: one at 3m geophone spacing (69 m total length, Figure 3.5); and one at 6 m (138 m total length, Figure 3.6). Both lines share the same easternmost point. Various shot offsets were used, with the optimal location being offset 5 m from the first geophone based on visual inspection of the traces and dispersion.

The dispersion for the 5 m offset shot is shown in Figure 3.7. The aim of the longer MASW transect is to resolve lower frequency dispersion and therefore image deeper structure. It appears that the dispersion is indeed resolved below the 5 Hz limit (Figure 3.7, left) seen for the shorter MASW transect, although caution is required in interpreting dispersion much below 5 Hz frequency due to (i) the source not generating sufficiently low frequency waves; (ii) the short duration of the signal; (iii) the sensitivity of the geophones (Foti et al., 2017). Nevertheless, using this information, it appears that the dispersion can be observed down to approximately 4 Hz.

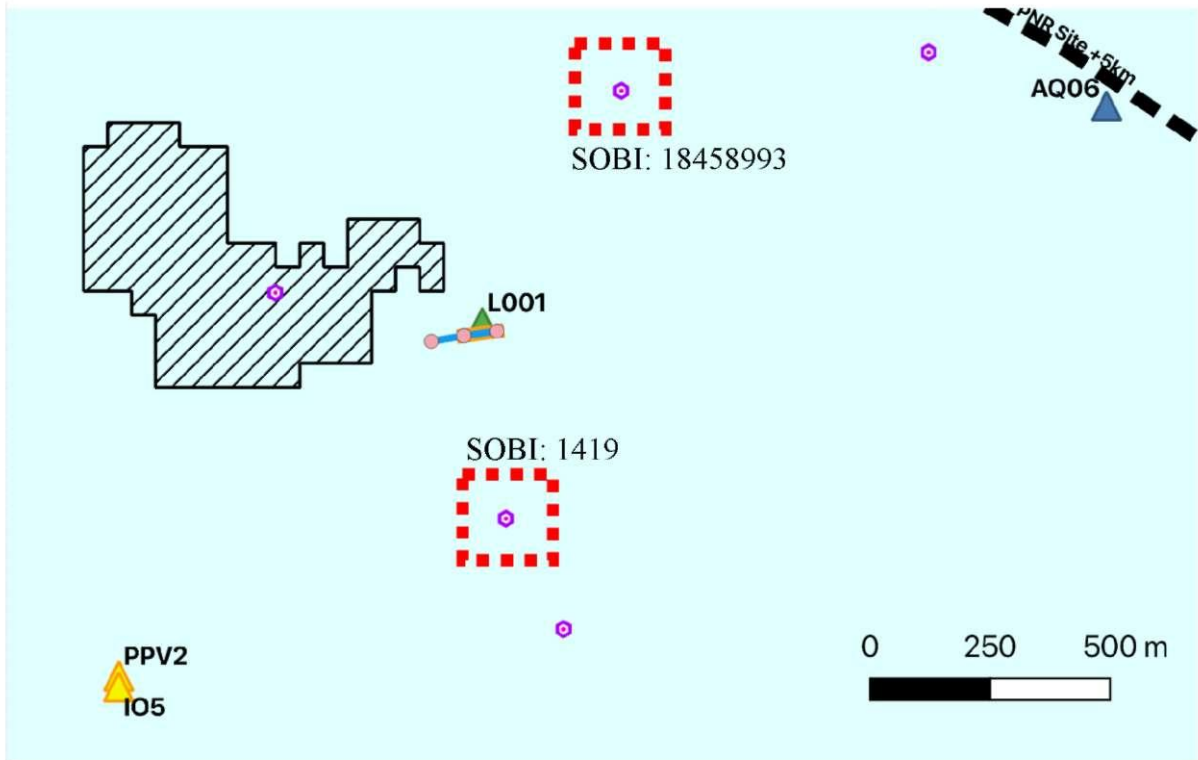


Figure 3.2. MASW line at site L001 (blue: 138 m; yellow: 69 m). Instrument sites IO5 and AQ06 are also nearby. The SOBI borehole log locations are indicated with purple circles. Hatched areas indicate populated regions. The background is the BGS superficial geology map. The highlighted SOBI locations indicate those in the text. Note: the SOBI IDs reveal confidential location information and should not be reproduced,

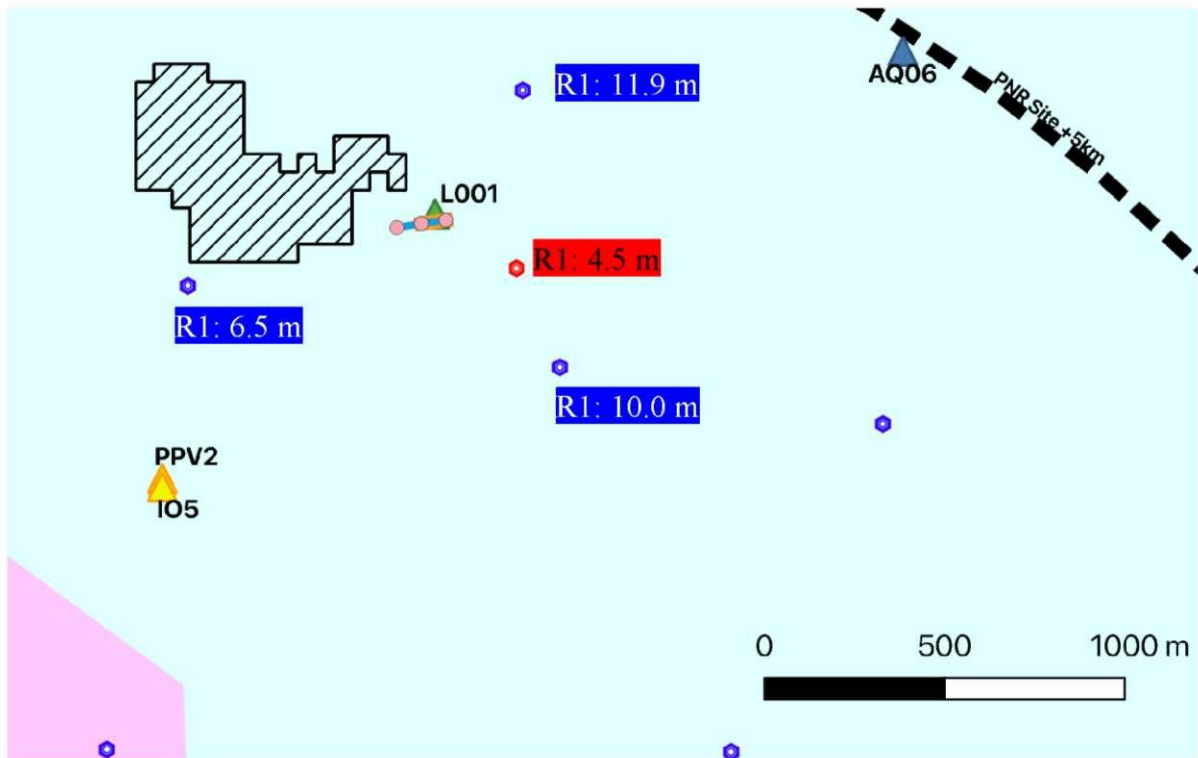


Figure 3.3. As previous, but showing location of low velocity layer refraction survey (blue) and borehole investigations (red) carried out on behalf of the operator. Depth to refractor 1 (R1) is indicated.

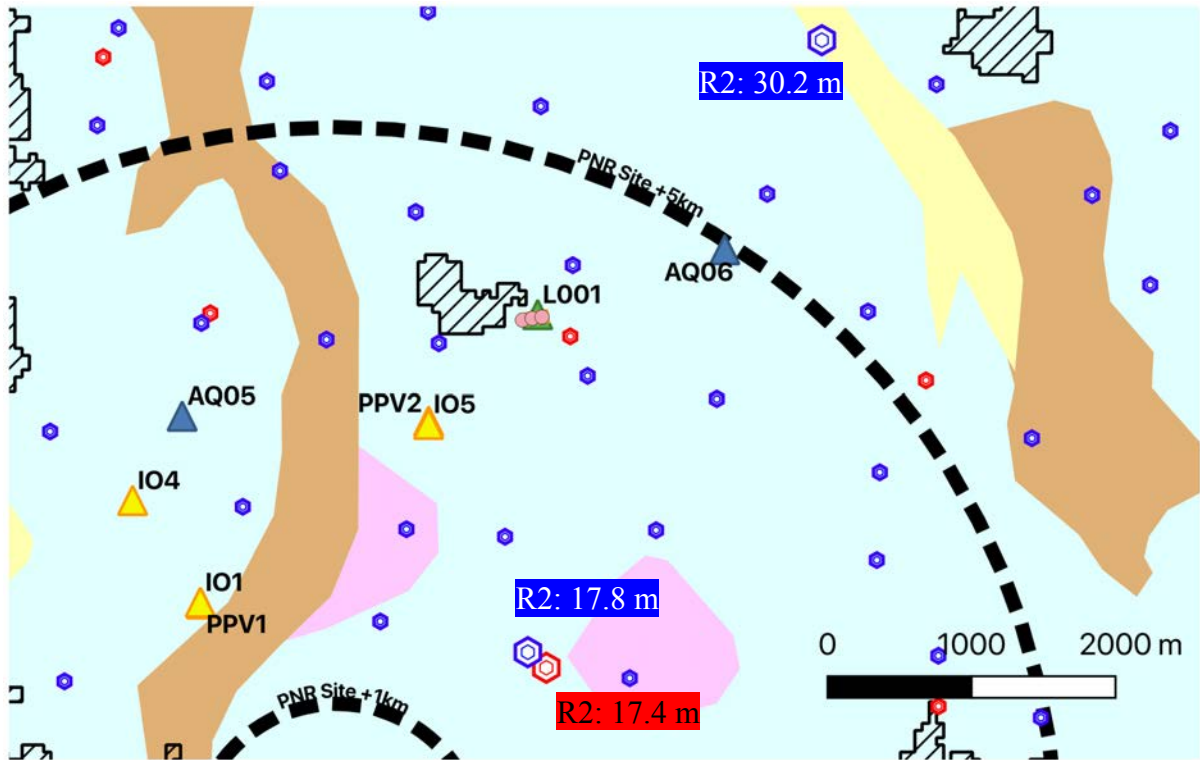


Figure 3.4. As previous, but showing location of more distant low velocity layer refraction survey (blue) and borehole investigations (red) carried out on behalf of the operator. Survey points with resolved refractor 2 depths (R2) are indicated.

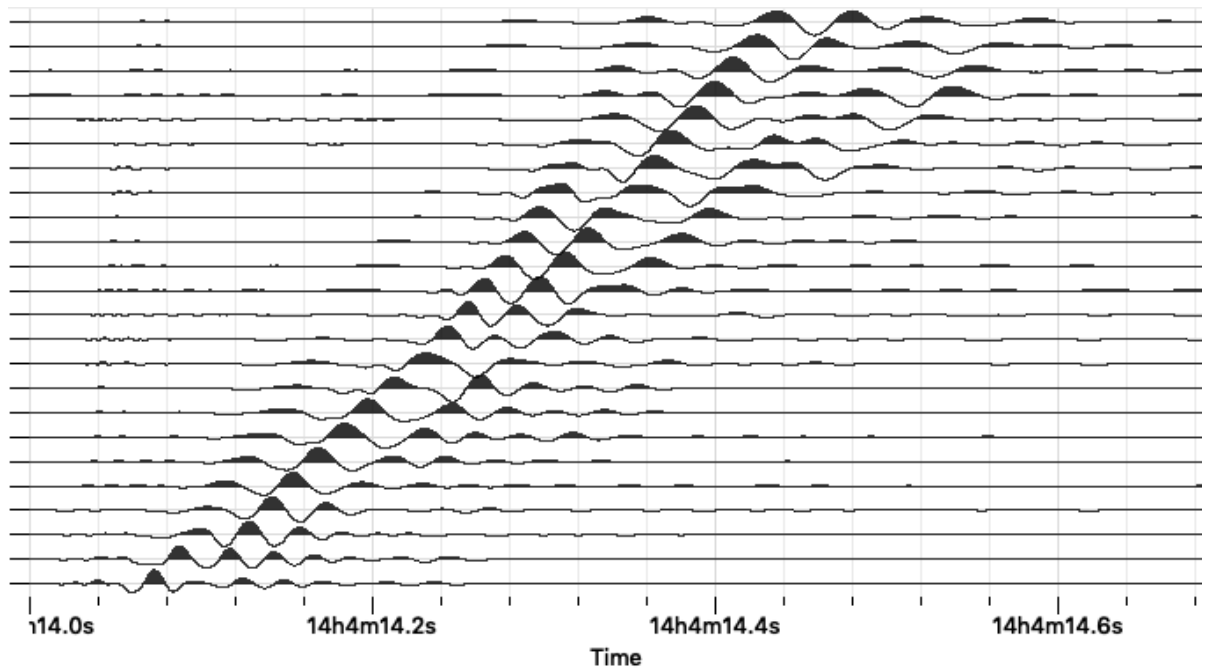


Figure 3.5. 24 geophone records (bottom nearest source), with 3 m spacing at site L001.

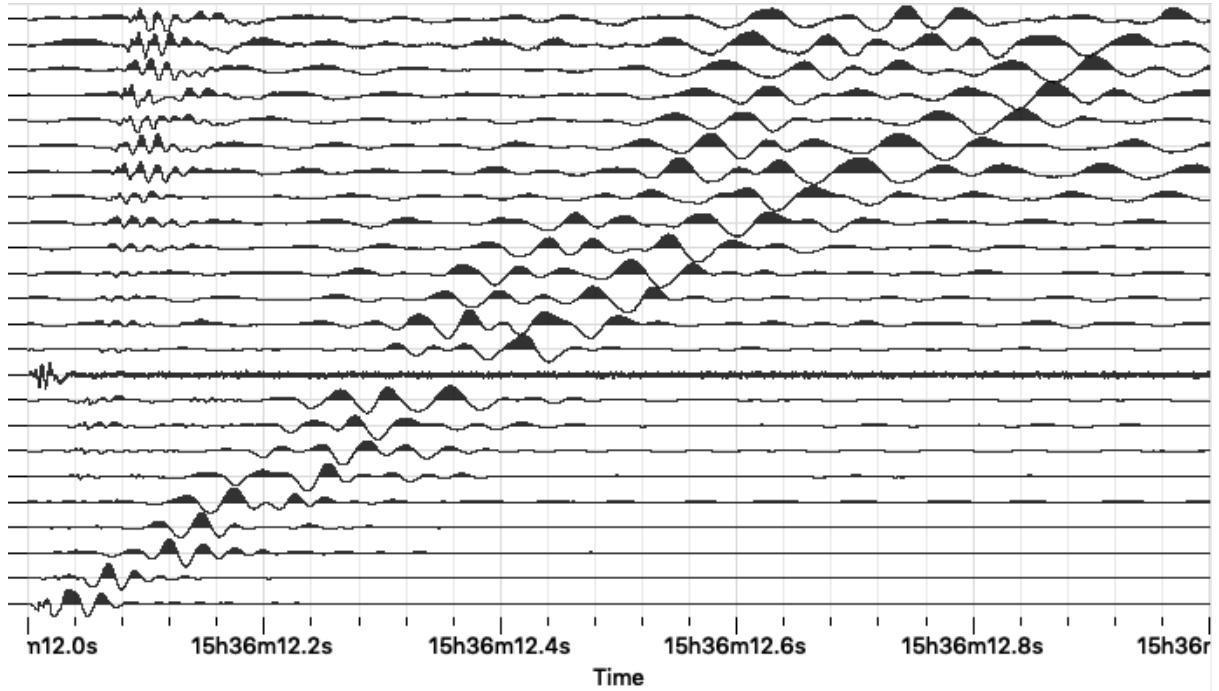


Figure 3.6. 24 geophone records (bottom nearest source), with 6 m spacing at site L001. Note geophone 15 is inactive during this measurement due to location constraints.

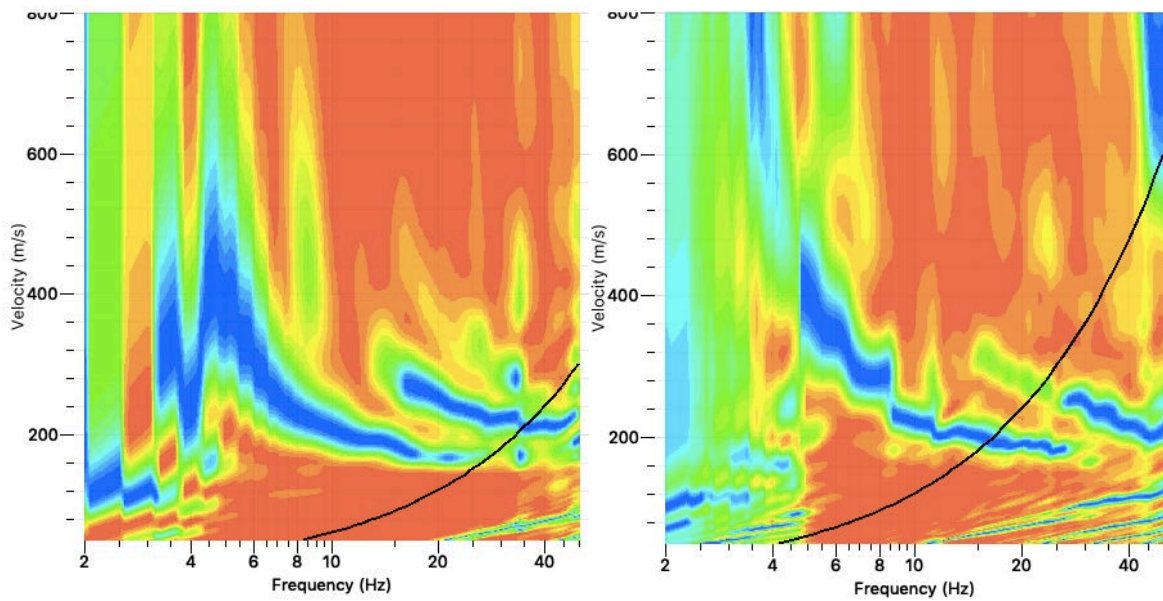


Figure 3.7. Dispersion plots for the MASW lines with (left) 3 m spacing and (right) 6 m spacing with 5 m shot offset. Aliasing limits are shown by the black lines.

### 3.1.2 Site L003

Site L003 lies on peat and alluvial deposits (Figure 3.8, inset) and is around 12 km from the PNR site and associated seismicity. One MASW line was measured with 2 m geophone spacing (46 m total length). Other regions within 5 km of PNR lie on similar geology (Figure 3.8), although the majority of the region is similar to site L001 (i.e., till deposits). As at the previous site, various shot offsets were used, with the optimal location being offset 5 m from the first geophone. Two nearby lithological logs were located in the SOBI (see Appendix A, IDs: 4838, 4495, Figure 3.9). The lithological logs indicate layers of soil followed by sand gravel and clay with increasing hardness down to about 20 m, overlying 'very hard clay gravel boulder stone'. No L V L or borehole information from the 3D seismic survey campaign was available in this area, however, the general trend over the wider survey of two refractors, the first around 5 to 12 and the second around 17 to 30 m is considered.

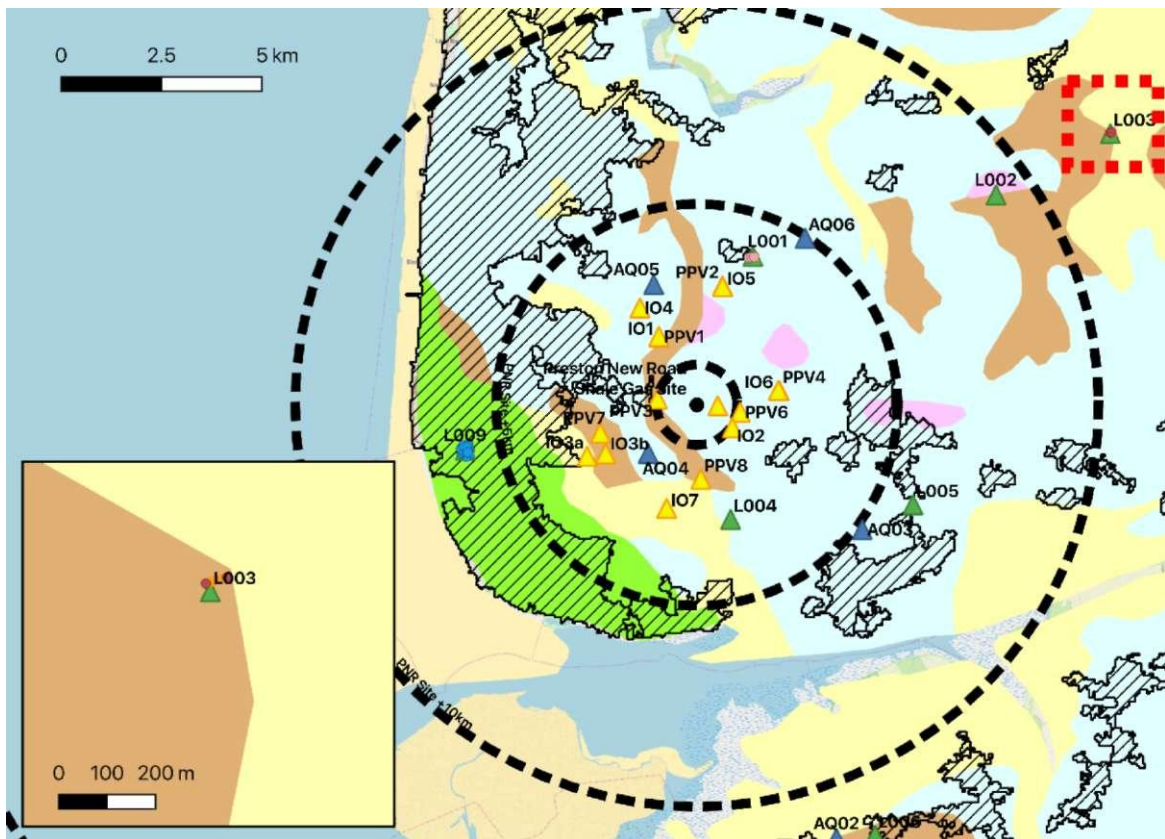


Figure 3.8. Location of MASW measurement at L003 (red dashed square). The PNR site along with 3, 5, 10 km zones around it are shown (dashed concentric rings). The base-map is the BGS superficial deposit map: green is blown sand; light blue is till; brown is peat and cream is alluvium. Built up areas are highlighted by cross-hatched regions. Inset: Location of MASW measurement points (circles) and surrounding region.

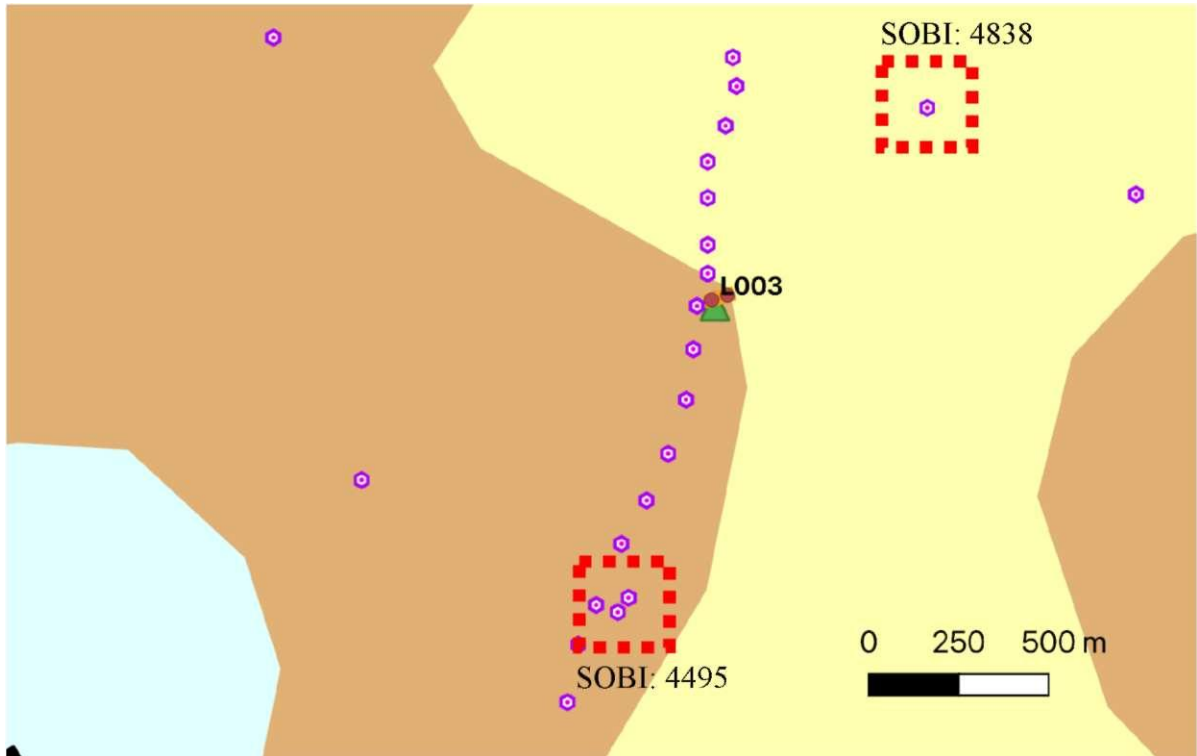


Figure 3.9. MASW line at site L003 (red circles mark end points). The SOBI borehole log locations considered in the analyses are indicated with purple circles. The background is the BGS superficial geology map. The highlighted SOBI locations indicate those in the text.

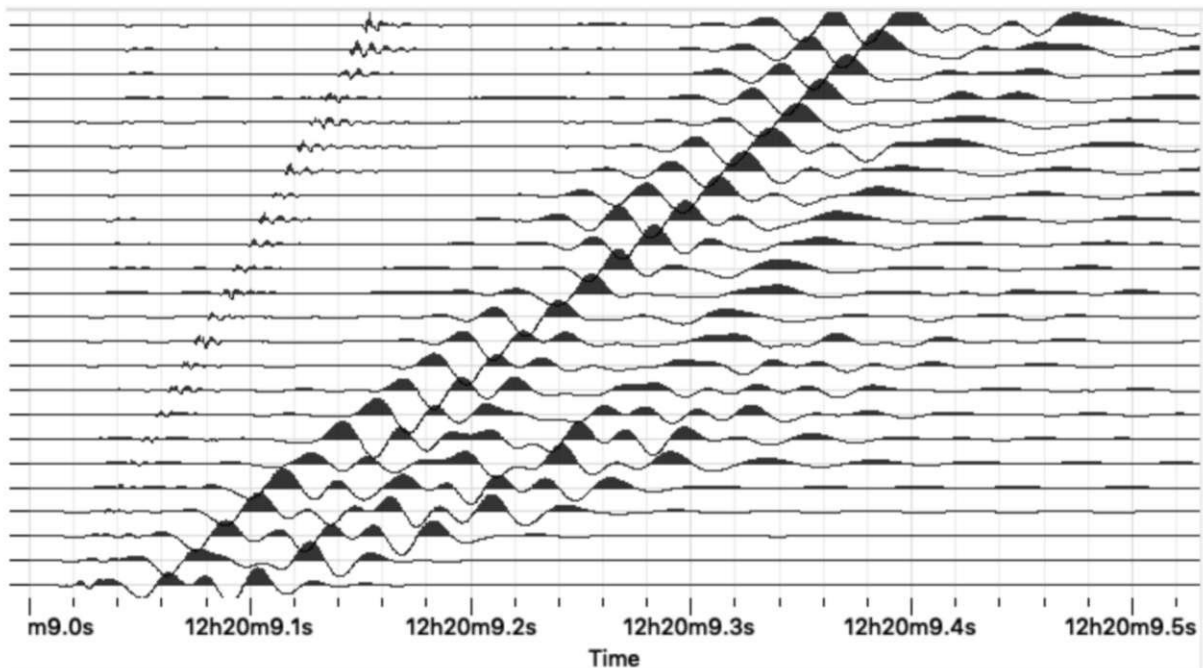


Figure 3.10. 24 geophone records (bottom nearest source), with 2 m spacing at site L003.

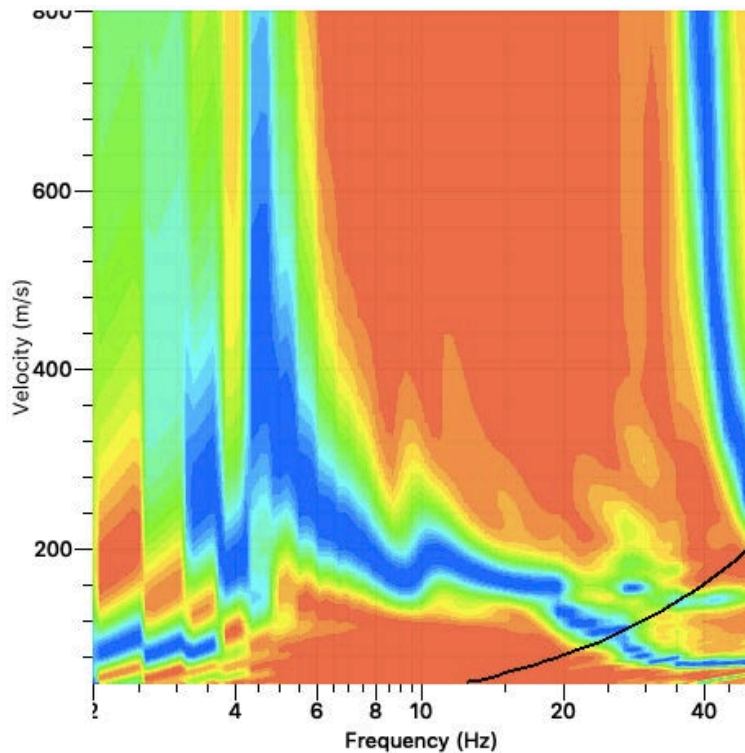


Figure 3.11. Dispersion plot for the MASW line at L003 with 2 m spacing and 5 m shot offset. The spatial aliasing limit is shown by the black line.

The recorded MASW data for L003 are shown in Figure 3.10 and the dispersion in Figure 3.11.

### 3.1.3 Site L009

Site L009 lies on blown sand deposits (Figure 3.12) and is around 6 km from the PNR site. Two borehole lithological logs were located in the SOBI within 250 m of the measurement site, which indicate the site comprises of mostly sand and sandy clay down to 26 m, where the boreholes end. One MASW line was measured with 3 m geophone spacing (69 m total length). Various shot offsets were used, with the optimal location (based on visual inspection of the traces and dispersion) being offset 5 m from the first geophone. The recorded MASW data are shown in Figure 3.13 and the dispersion in Figure 3.14.

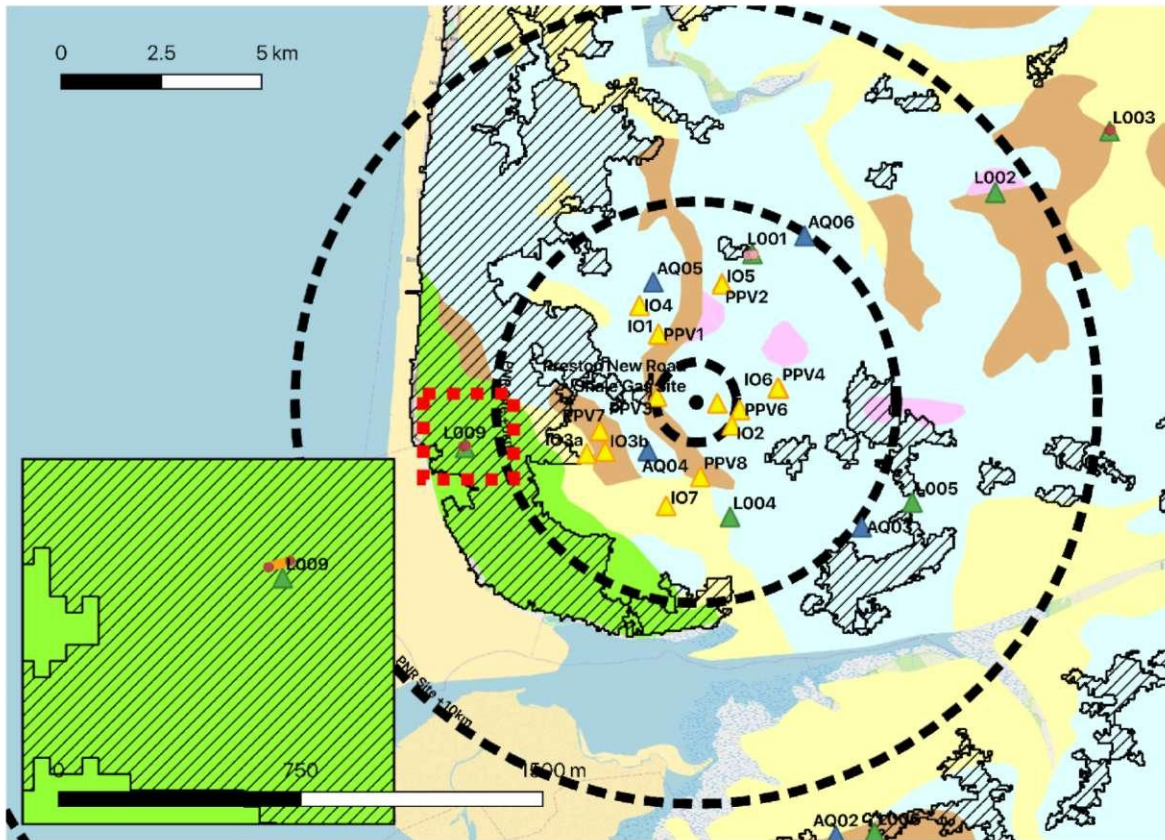


Figure 3.12. Location of MASW measurement at L009 (red dashed square). The PNR site along with 3, 5, 10 km zones around it are shown (dashed concentric rings). The base-map is the BGS superficial deposit map: green is blown sand; light blue is till; brown is peat and cream is alluvium. Built up areas are highlighted by cross-hatched regions. Inset: Location of MASW measurement points (circles) and surrounding region.

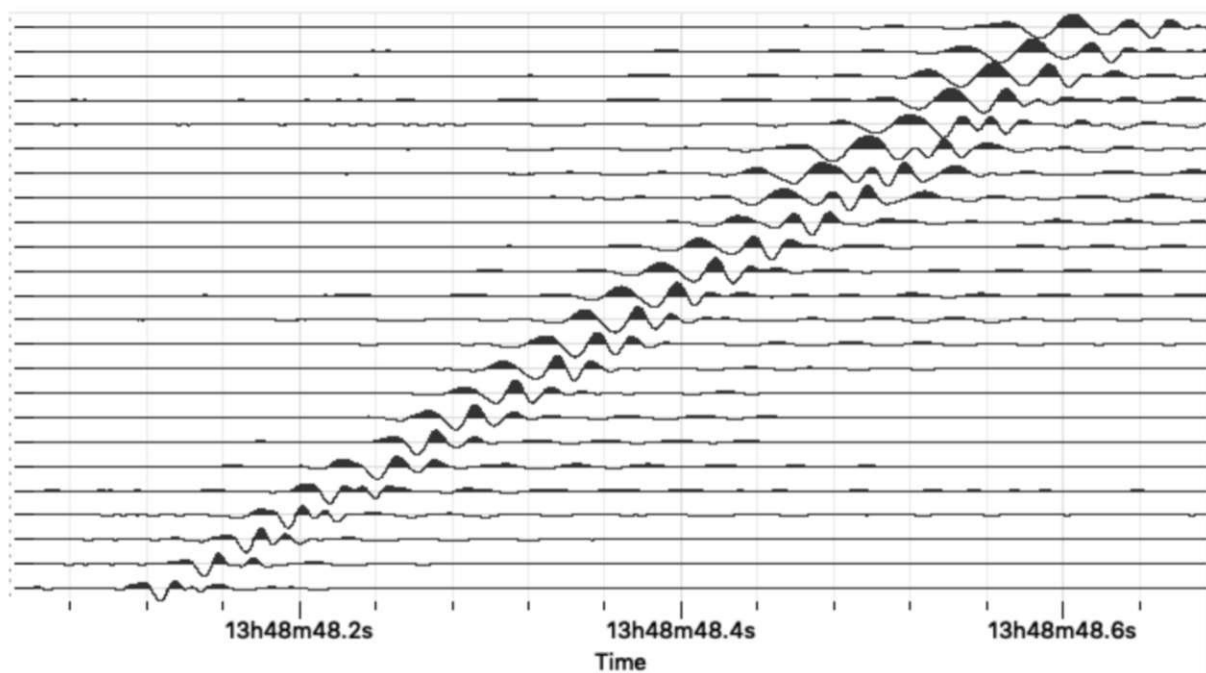


Figure 3.13. 24 geophone records (bottom nearest source), with 3 m spacing at site L009.

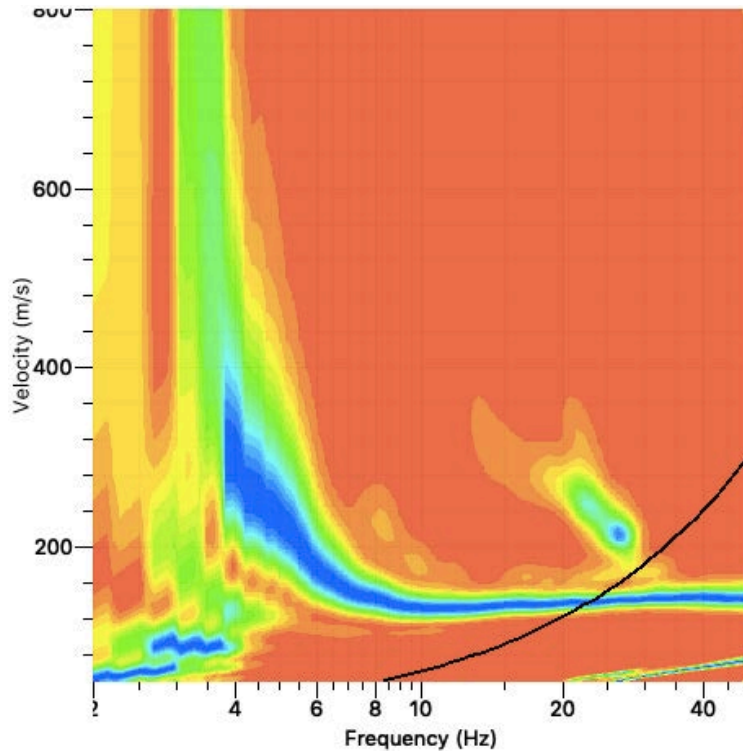


Figure 3.14. Dispersion plot for the MASW line at L009 with 3 m spacing and 5 m shot offset. Aliasing limit is shown by the black line.

### 3.2 Shear-Wave Velocity Model for Selected PNR sites

#### 3.2.1 Till deposit sites (L001)

Using the available lithological logs for site L001, along with the Rayleigh wave dispersion (Figure 3.7, Section 3.1.1) an initial model layering was defined (with tolerance of  $\pm 2$  m, increasing to  $\pm 4$  m at depth) for the inverted subsurface profiles. The fundamental mode Rayleigh dispersion was inverted (Figure 3.15) to provide  $V_s$  following the approach detailed in Wathelet (2008) and Wathelet et al. (2004), through software ‘dinver’ (part of the geopsy programme package). Poisson’s ratio was allowed to vary between 0.2 and 0.5,  $V_p$  was allowed to vary between 80 and 5000 m/s,  $V_s$  between 50 and 1500 m/s (i.e., velocity was almost unconstrained) and density was set at 2000 kg/m<sup>3</sup>. The most sensitive parameter in the inversion of Rayleigh wave dispersion is  $V_s$ , with  $V_p$  and density poorly resolved. In addition to the lithologically based model, a simple model with 5 m layers is presented (Figure 3.16).

In Figure 3.15 the full suite of inverted dispersion curves is shown. The ‘best fitting’ models encapsulating the observed dispersion (misfit < 0.05) are shown in terms of the corresponding  $V_s$  in Figure 3.16. Note the change in colour scale.

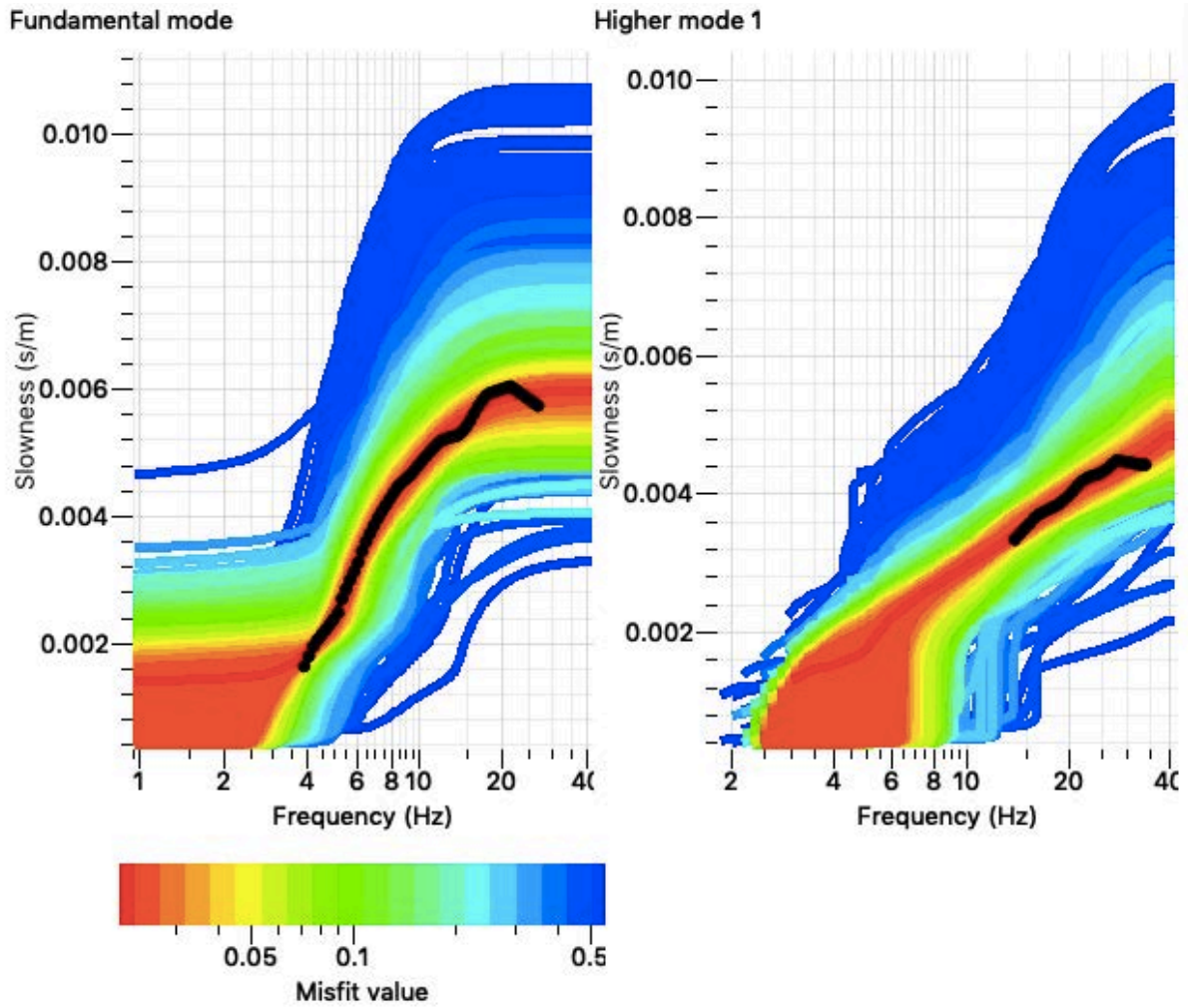


Figure 3.15. Inverted dispersion for site L001 using the lithological based layering. The black symbols indicate the picked dispersion from Figure 3.7, while the coloured lines indicate the dispersion corresponding to the full suite of randomised velocity profiles. The best-fitting (misfit < 0.05)  $V_s$  models are presented in Figure 3.16.

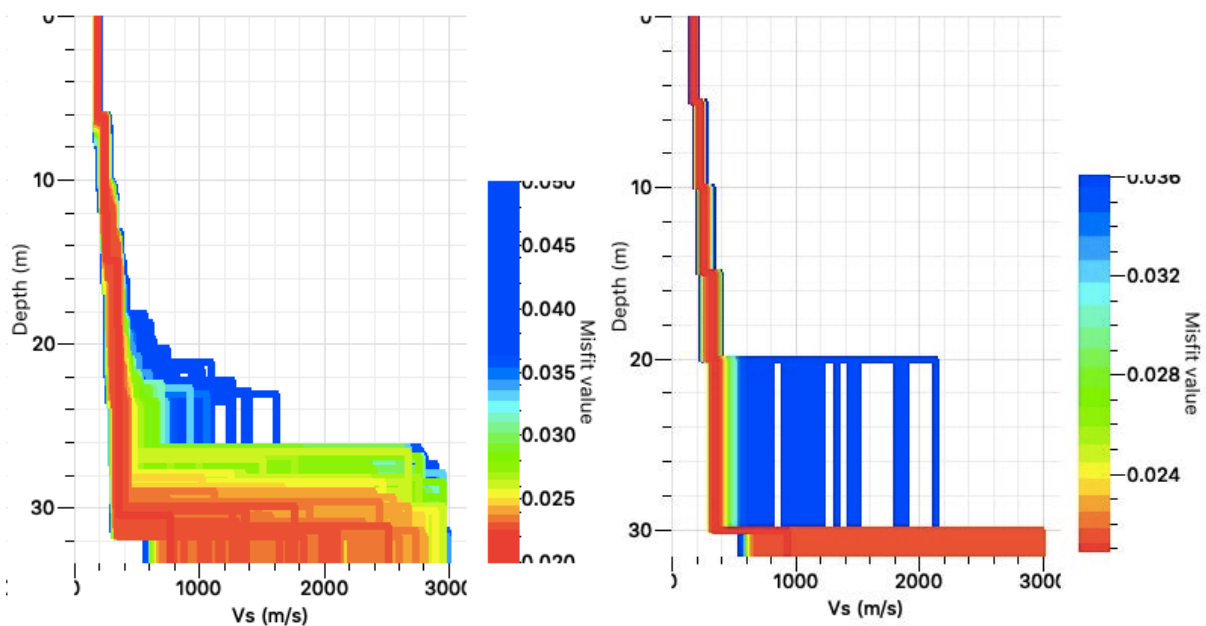


Figure 3.16. Inverted ground profile ( $V_s$ ) for site L001 using the lithological based layering (left) and 5m layering (right).

This site exhibits slowly increasing velocity with depth (Figure 3.17), from values around 180-200 m/s at the surface, to 300-400 m/s at or around 30 m. A first possible refractor is evident at around 5 - 6 m, consistent with the LVL survey data, with a second possible at around 16 m. A clear interface is evident at around 29 – 32 m consistent with the transition from till to mudstone in the lithological logs. The velocity of the mudstone is poorly constrained, but is likely to be above 600 m/s.

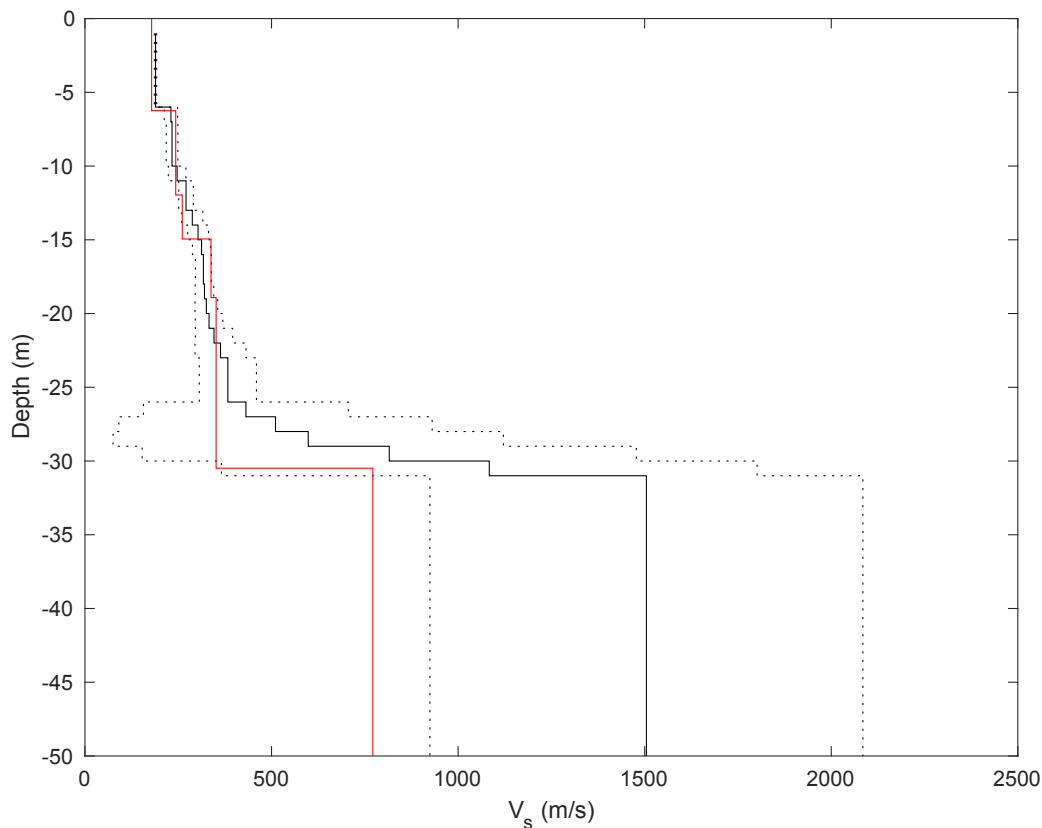


Figure 3.17. Mean and standard deviation assuming normal distribution (from all models using the lithological layering with misfit  $< 0.05$ , Figure 3.16, black) and the best-fitting single model (red) for site L001. Note that the resolution below 30 m is very poor and therefore  $V_s$  unreliable.

### 3.2.2 Peat/Alluvium Deposit Sites (L003)

At L003, only the fundamental mode dispersion was evident and was therefore used as the inversion target. Using the available lithological logs for site L003, along with the Rayleigh wave dispersion (Section 3.1.2) an initial layering was defined (with tolerance of  $\pm 2$  m, increasing to  $\pm 4$  m at depth) for the inverted subsurface profiles. As for all sites, Poisson's ratio was allowed to vary between 0.2 and 0.5,  $V_p$  was allowed to vary between 80 and 5000 m/s,  $V_s$  between 50 and 1500 m/s (i.e., almost unconstrained) and density was set at  $2000 \text{ kg/m}^3$ . In addition to the lithologically based model, a simple model with 5 m layers is presented.

In Figure 3.18 the full suite of inverted dispersion curves is shown. The 'best fitting' models (misfit  $< 0.07$ , encapsulating the empirical dispersion curve) are shown in terms of the corresponding  $V_s$  in Figure 3.19. Note the change in colour scale.

The profile in this case shows evidence for a small increase in  $V_s$  at about 6 m and again at 15 – 17 m (as for the previous site). The deeper 30 m refractor (as observed at the previous site at around 30 m) is not resolved, however, the uncertainties at increase significantly from about 25 m (Figure 3.20), slightly shallower than at site L001.

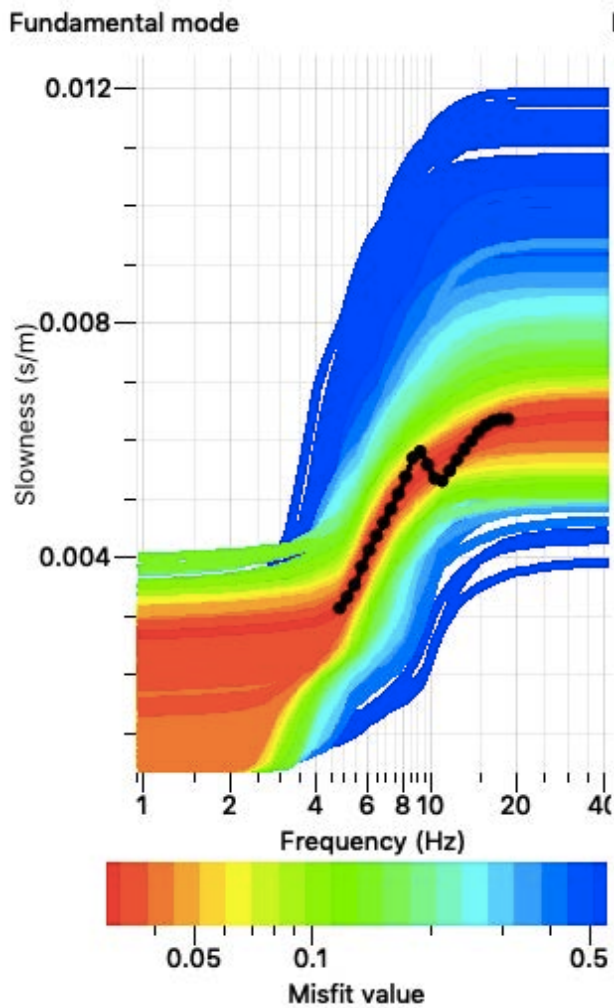


Figure 3.18. Inverted dispersion for site L003 using the lithological based layering. The black symbols indicate the picked dispersion from Figure 3.11, while the coloured lines indicate the dispersion corresponding to the full suite of randomised velocity profiles. The best-fitting (misfit < 0.07)  $V_s$  models are presented in Figure 3.19.

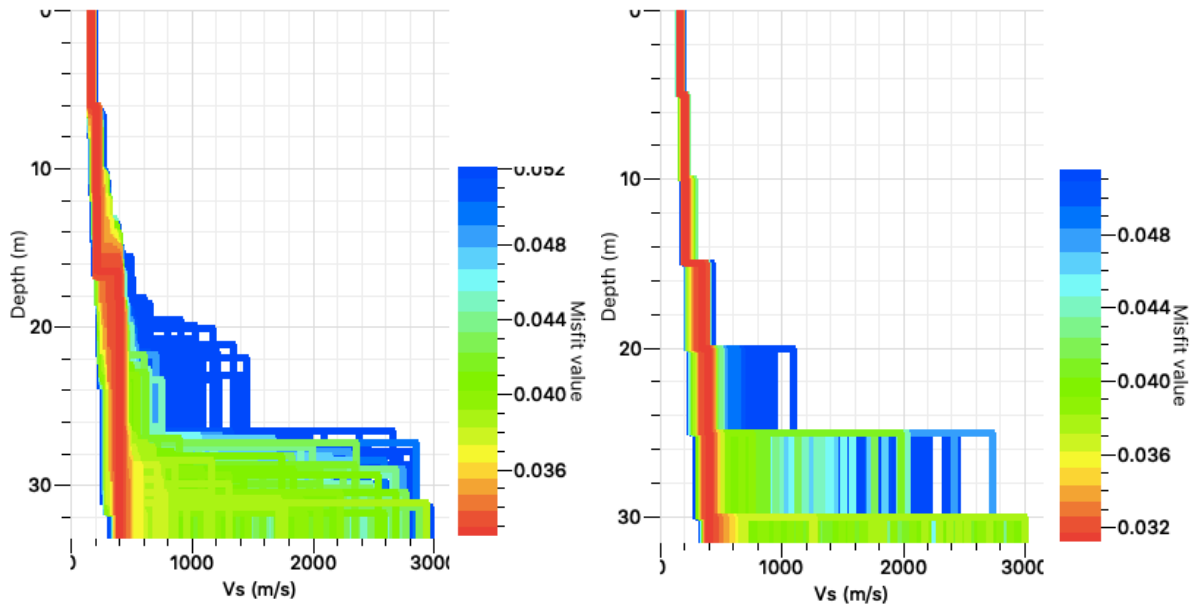


Figure 3.19. Inverted ground profile ( $V_s$ ) for site L003 using the lithological based layering (left) and 5m layering (right).

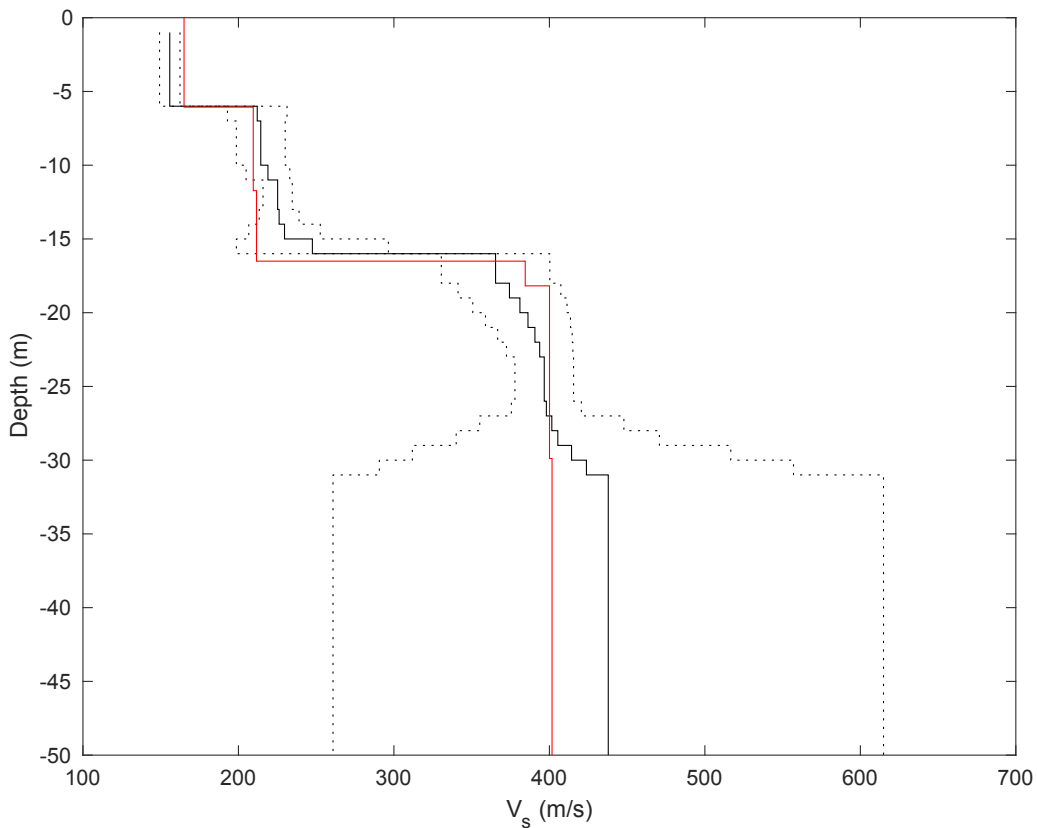


Figure 3.20. Mean and standard deviation assuming normal distribution (from all models with misfit < 0.07, black) and the best single model (red) for site L003. Note that the resolution below 30 m is very poor and therefore  $V_s$  unreliable.

### 3.2.3 Blown sand deposit sites (L009)

At site L009 only the fundamental dispersion curve was observed using the MASW. Using the available lithological logs for the site, along with the Rayleigh wave dispersion (Section 3.1.3) an initial layering was defined (with tolerance of  $\pm 2$  m, increasing to  $\pm 4$  m at depth) for the

inverted subsurface profiles. In this case, since no basement rock was evident in the logs, we allow for a final layer at anywhere below 20 m. Poisson's ratio was again allowed to vary between 0.2 and 0.5,  $V_p$  was allowed to vary between 80 and 5000 m/s,  $V_s$  between 50 and 1500 m/s (i.e., almost unconstrained) and density was set at 2000 kg/m<sup>3</sup>. In addition to the lithologically based model, a simple model with 5 m layers is presented.

In Figure 3.21 the full suite of inverted dispersion curves is shown. The 'best fitting' models (misfit < 0.06) are shown in terms of the corresponding  $V_s$  in Figure 3.22. Note the change in colour scale. The average model, based on the lithological layering is shown in Figure 3.23 and essentially comprises of two layers with an interface at around 13 m.

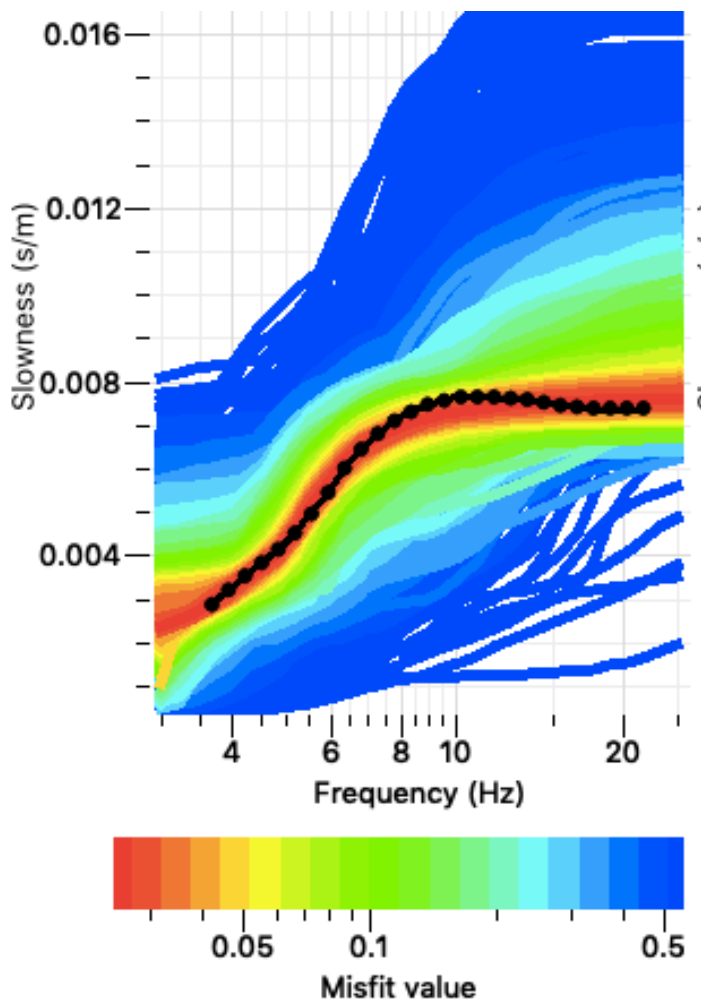


Figure 3.21. Inverted dispersion for site L09 using the lithological based layering. The black symbols indicate the picked dispersion from Figure 3.14, while the coloured lines indicate the dispersion corresponding to the full suite of randomised velocity profiles. The best-fitting (misfit < 0.06)  $V_s$  models are presented in Figure 3.22.

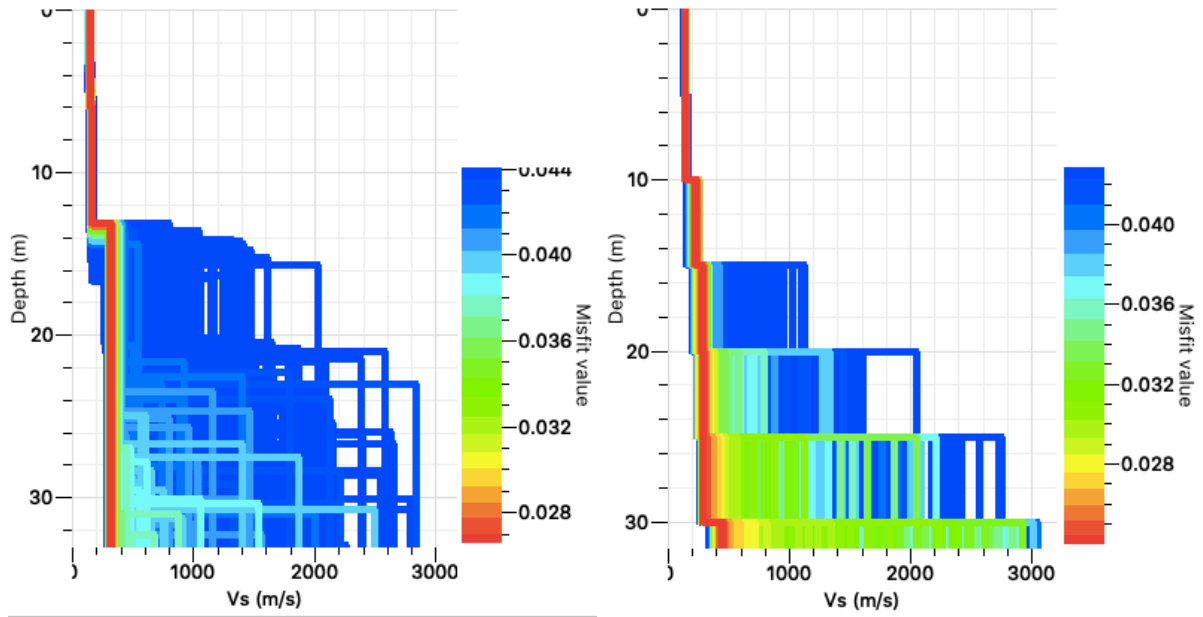


Figure 3.22. Inverted ground profile ( $V_s$ ) for site L009 using the lithological based layering (left) and 5m layering (right).

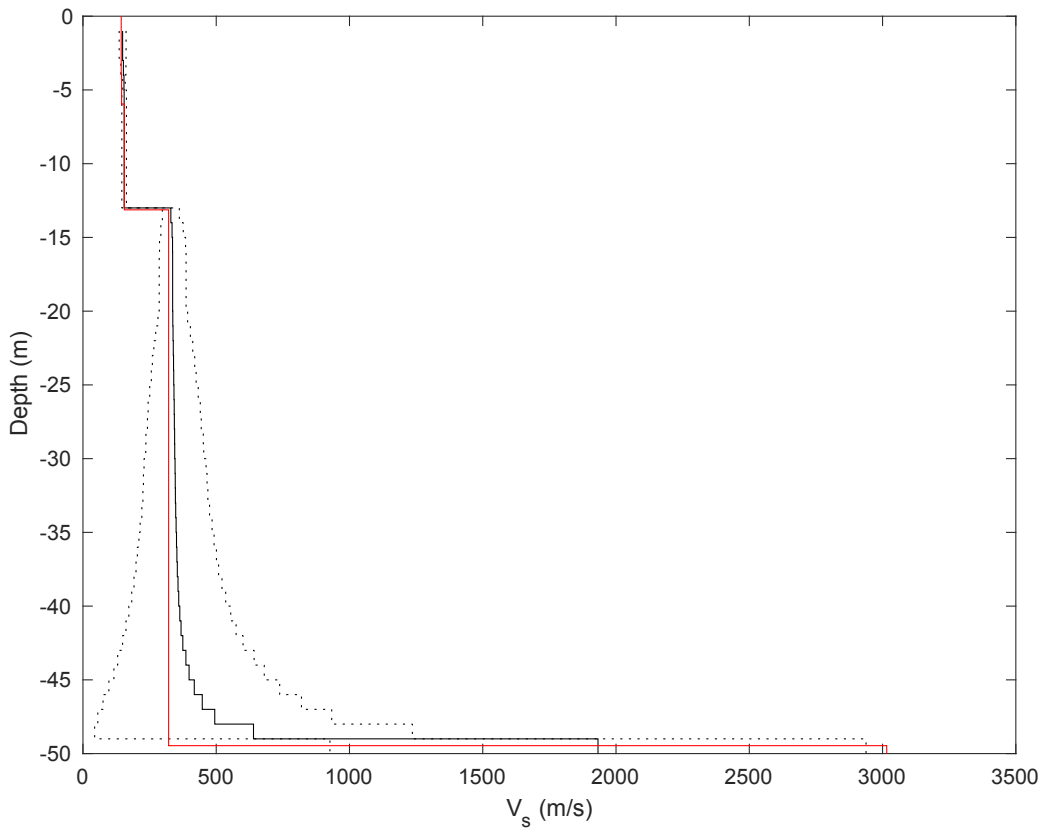


Figure 3.23. Mean and standard deviation assuming normal distribution (from all models with misfit < 0.06, black) and the best single model (red) for site L009. Note that the resolution below 30 m is very poor and therefore  $V_s$  unreliable.

### 3.3 $V_{s30}$ for PNR sites

Using the shear-wave velocity profiles estimated in the previous section we can directly calculate travel time average velocity to depth  $x$  using:

$$V_{s,x} = \frac{x}{\sum_{i=1}^N \frac{h_i}{V_{s,i}}} \quad (19)$$

where there are  $N$  layers, with defined thickness of the  $i^{\text{th}}$  layer  $h_i$ , and shear-wave velocity  $V_{s,i}$ . The 30 m shear-wave velocity profile is therefore discretised in to  $N$  layers of constant velocity and  $V_{s30}$  calculated. Since a range of possible models are produced (within a defined misfit) an uncertainty on  $V_{s30}$  is obtained in terms of its standard deviation.

An alternative method to estimate  $V_{s30}$  is based on correlations to the dispersion of Rayleigh wave phase velocity of the 40 – 45 m wavelength signal,  $V_{R,40-45}$ , approximated by:

$$V_{s30} = V_{R,40-45} \quad (20)$$

(Foti et al., 2017). Generally,  $V_{R,40}$  is more appropriate at sites with shallow groundwater, as expected here. Table 3.1 summarises the  $V_{s30}$  values using the various approaches detailed above. Covering the range of  $V_{s30}$  values, we defined three equally spaced values for scenario calculations as 200, 240 and 280 m/s.

Table 3.1.  $V_{s30}$  values (mean and plus/minus one standard deviation).

Surface Deposit	Lithological Depths	Site	$V_{s30}$ from $V_{R,40-45}$	$V_{s30}$ from $V_s(z)$ (median)	$V_{s30}$ from $V_s(z)$ (16 <sup>th</sup> - percentile)	$V_{s30}$ from $V_s(z)$ (84 <sup>th</sup> - percentile)
Till	Yes	L001	269.0	257.1	251.7	264.4
	No			249.7	247.6	252.8
Alluvium /Peat	Yes	L003	244.3	240.0	237.3	244.3
	No			234.0	233.3	235.7
Sand	Yes	L009	213.3	205.3	203.3	205.5
				195.5	194.1	196.0

#### 4. Induced Events and Ground Motions Observed at PNR

57 seismic events ( $-0.8 \leq M_L \leq 1.5$ ) were detected in close proximity to the PNR site by the BGS during the period 15<sup>th</sup> October to 17<sup>th</sup> December (Figure 4.1, Figure 4.2).

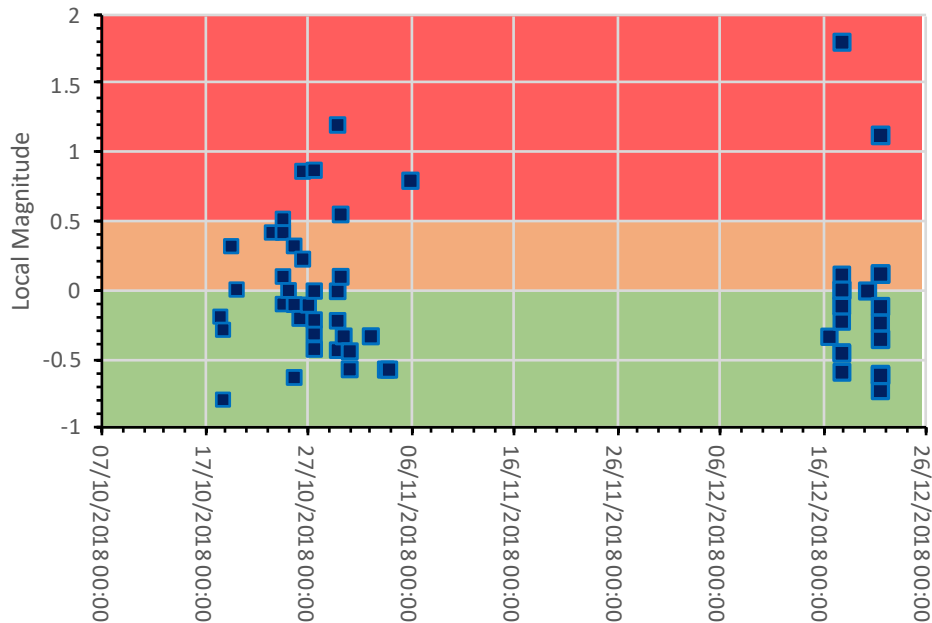


Figure 4.1. Timeline for the PNR induced events indicating the TLS *magnitude* categories (note this does not distinguish pumping and trailing events as required in the TLS event classification).

Previous activity in the area was almost negligible: although the magnitude of completeness for most of the UK is around  $M_L$  2, the monitoring networks were in place prior to the onset of fracking. The 57 events detected at the surface were clearly, therefore, a direct result of the fracking operations at PNR. In addition to these events detected at the surface, thousands of additional micro-seismic events ( $M_L < 0$ ) were detected and located by the operator using a downhole instrument array. However, these are not the focus of this analysis, as they are too small to be of any interest to seismic hazard, at the surface or at depth. Important to note is that the magnitude of completeness of the surface seismic network is *around*  $M_L$  0 (pers. comm. BGS). It is therefore not unlikely that additional events may be detected that fall into the TLS amber category (e.g., during particularly noisy time periods). Nevertheless, the 57 events catalogued to date provide ample data to analyse in order to assess the ground shaking within the context of seismic hazard and model performance for possible future scenario events. In the following section we detail the analysis performed on the data recorded at the surface, and the available macroseismic information from felt reports.

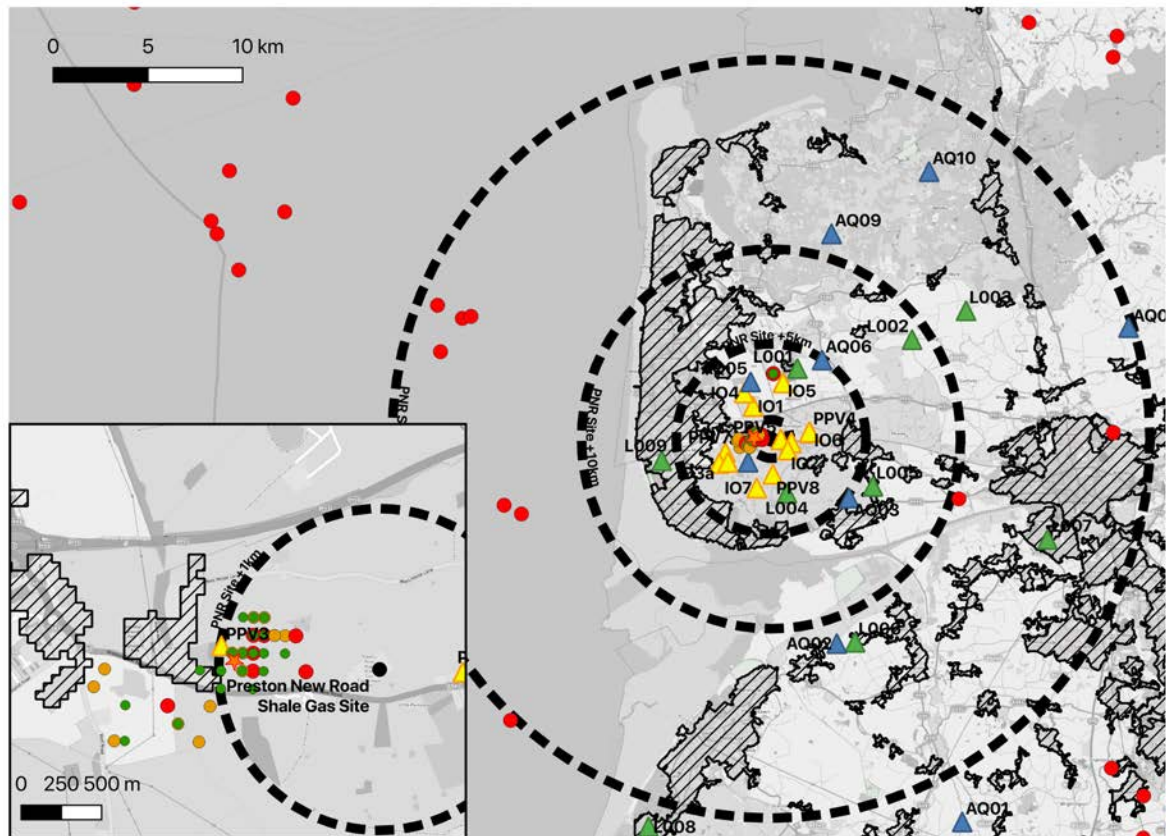


Figure 4.2. Overview of PNR seismicity (inset, colours according to the TLS magnitude classification) in addition to the wider region historical seismicity and the monitoring networks in place (yellow: Cuadrilla; Green: University of Liverpool; Blue: BGS). Detected seismic events are shown according to their TLS magnitude category, as in Figure 1.1. Note PPV stations are not used in this analysis due to concerns as to their reliability (Bommer and Edwards, 2018).

#### 4.1 Macroseismic Data for the Events

The British Geological Survey regularly provide macroseismic intensity (see Section 2.4.1) for UK earthquakes. These intensity estimates, which aim to quantify the potential ‘felt effects’ and damage from earthquakes are based on (i) ‘did you feel it’ web questionnaires submitted to the BGS ([www.earthquakes.bgs.ac.uk/questionnaire/EqQuestIntro.html](http://www.earthquakes.bgs.ac.uk/questionnaire/EqQuestIntro.html)) and, in the case of larger events (ii) damage surveys. In addition, macroseismic intensity can be estimated using equations that link recorded motions (GMICE, see Section 2.4.2) or to magnitude (e.g., Musson, 2003).

For the two larger events that occurred during hydraulic fracturing of PNR-1z, macroseismic intensities were assigned by the BGS (Table 1.1). Both events were assigned European macroseismic intensity II, which equates to “Scarcely felt – Felt only by very few individual people at rest in houses”. In order to supplement this data, we have collated all epicentral intensity estimates for UK earthquakes from the BGS macroseismic intensity database (Figure 4.3). These data include, for instance the recent Newdigate seismic sequence in 2018 and 2019 that comprised of tightly clustered events at about 2 km depth (Hicks et al., 2019). This shows that previous events in the  $M_L$  1 to 1.5 range have been assigned intensities of between II (the lowest that is assigned), and IV+, with ‘+’ indicating a mid-way point between two intensities.

Intensity VI is considered the threshold of minor cosmetic damage in the EMS-98 scale. It can therefore be generalised that events with  $M \leq 2$  have not been associated with cosmetic damage in the UK.

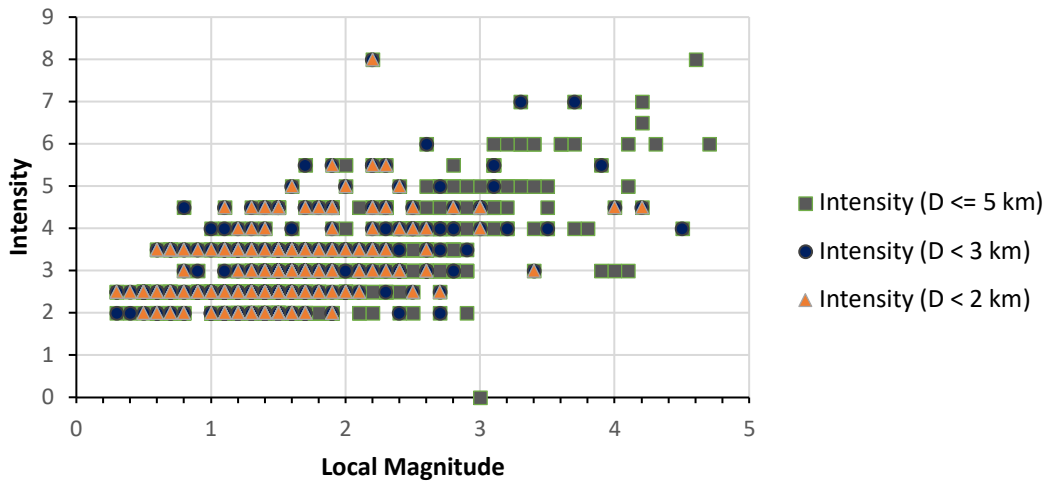


Figure 4.3. Epicentral intensity for UK events with shallow focal depths ( $D < 5$  km) versus magnitude.

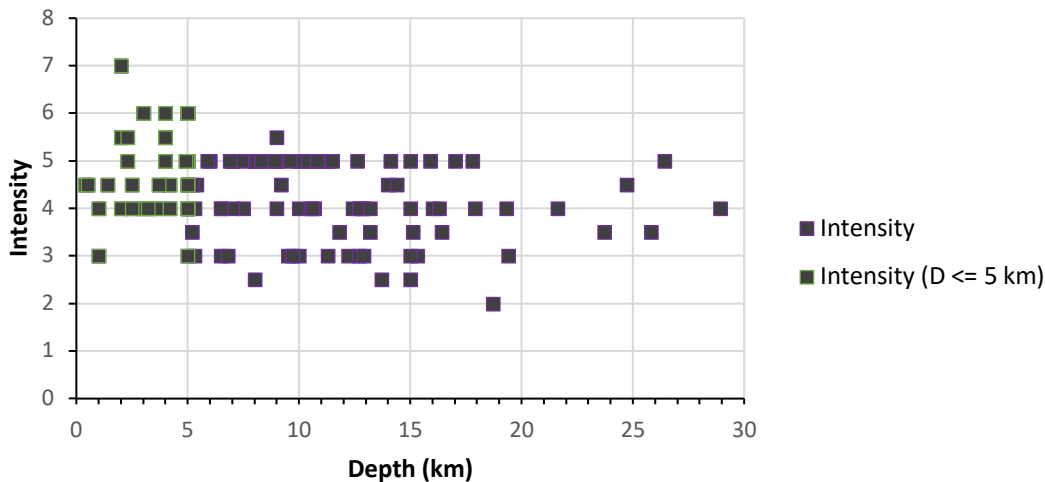


Figure 4.4. Epicentral intensity for UK events with  $M_L$  3 to 4 versus depth.

There appears to be no clear depth dependence on the intensity values (with decreasing depth to 2 km), which may give some support to the fact that shallow focus earthquakes have lower stress drops than larger events (Hough, 2014), since otherwise we would expect higher intensities for increasingly shallow events. However, looking at intensities for deeper events within a defined magnitude range of 3 to 4 (Figure 4.4), we observe an apparent increase of epicentral intensity for sources with depth less than 5 km. It should be noted, however, that the highest intensities often correspond to historical events with highly uncertain depths (and intensities), therefore this apparent trend is debatable. Whether depth dependent stress drop for UK events is an issue is therefore not clear. What can be generalised from this data, however, is that for events with  $M_L$  3 to 4 we expect higher intensities (generally IV to VI) for shallow induced events, than for typical tectonic events (which typically occur around 10 km depth). Intensity V and VI would imply strong shaking to minor cosmetic damage respectively. For

induced events with  $M_L < 3$  macroseismic intensity is unlikely to exceed V+ based on existing data.

Outlier observations exist that are of interest in Figures 4.3 and 4.4. The first is an intensity VII event in Figure 4.4. This was a  $M$  3.3 earthquake in Mansfield on 04/04/1924 (Figure 4.5). Its intensity has been assigned through historical documents and reports and may therefore be less reliable than more recent data. Its intensity of VII indicates that it was damaging with “many well built ordinary buildings suffering moderate damage: small cracks in walls, fall of plaster, parts of chimneys fall down; older buildings may show large cracks in walls and failure of fill-in walls.” This event occurred after a similar sized event in the same location the previous month (06/03/1924), which may have weakened some vulnerable structures and led to the higher than expected epicentral intensity. Compounding of reported effects for these closely spaced events may also have led to the appearance of more significant damage for the later event. A  $M$  2.2 event with intensity VIII is also of interest. This event occurred in Barrow-in-Furness on 1865-02-15 and led to heavy damage in the village of Rampside and liquefaction in the tidal area according to Musson (1996). Musson (1996) assigns a magnitude of  $M_L$  2.5 to 3.5. This is, however, highly unusual for such a small event (as noted by Musson himself), which opens the question as to whether, for instance, the assigned magnitude is too low. In fact, the intensity VIII assignment is highly contentious, with Green and Bommer (2019) recently challenging the interpretation of this event. Finally, the  $M$  2.6 event with intensity VI was the 1750-02-08 event that occurred in London. This was a very shallow event (2 km) that occurred in a densely populated area with likely mixed levels of construction quality, which may therefore be attributed to its high intensity.

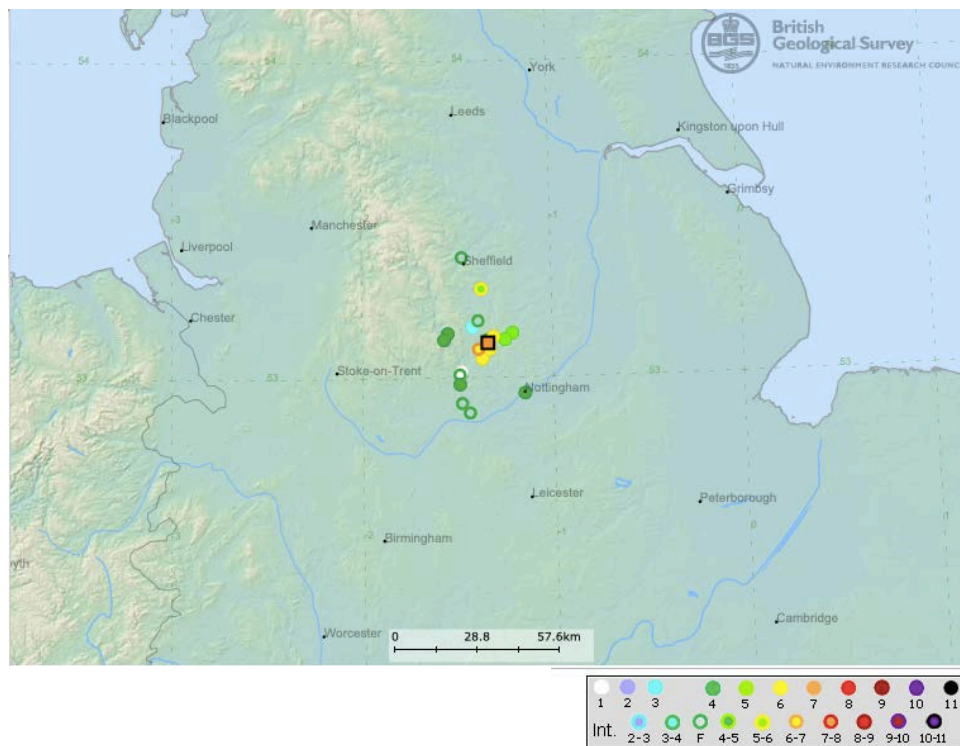


Figure 4.5. Epicentral intensity for the M 3.3 Mansfield earthquake. Image source: BGS.

#### 4.2 Surface Ground Motion Recordings from PNR Events

In total 26 seismometers were in operation within 25 km of the PNR site. Nine were operated by the BGS, 9 by the University of Liverpool (UoL) and 8 by the operator (Figure 4.2). The instruments were all high-quality broadband sensors with data recorded on high dynamic range digital dataloggers. BGS and UoL operated continuous datalogging at 100 sample per second on 24 bit instruments. The operator recorded at 200 sps, which technically allows higher frequency signals to be observed. However, most of this signal is dominated by noise for surface records. UoL operates Nanometrics 3-component Trillium compact 120 broadband instruments, while BGS use 3-component Guralp broadband sensors. All these sensors can be considered to produce equivalent scientific quality records. The station distribution is dominated by the operator's instruments in the nearest 5 km, with BGS and UoL having a more disperse network over a 20 km radius.

Data from the 57 events recorded on 26 seismometers (a total of 1482 3-component records) has been reviewed through visual inspection. In case there was a clear uncorrupted signal the record was retained for further analyses: 758 of the three-component records passed this initial inspection. The resulting data distribution is relatively uniform between local magnitude -0.8 and 1.5 and epicentral distances 1 to 20 km (Figure 4.6).

While the data is visually acceptable, it is important to define usable frequency ranges for each of the records. This is achieved through signal-to-noise ratio (SNR) analysis, whereby a pre-event portion of the time-series signal is compared to the event waveform in the Fourier (frequency) domain. The continuous frequency range where the signal exceeds the baseline noise level by a factor 3 is considered the usable Fourier domain frequency range ( $f_{low}$  to  $f_{high}$ ) (Figure 4.7). Plots of the time series, FAS, response spectra, and corresponding usable frequencies and periods are included in Appendix B.

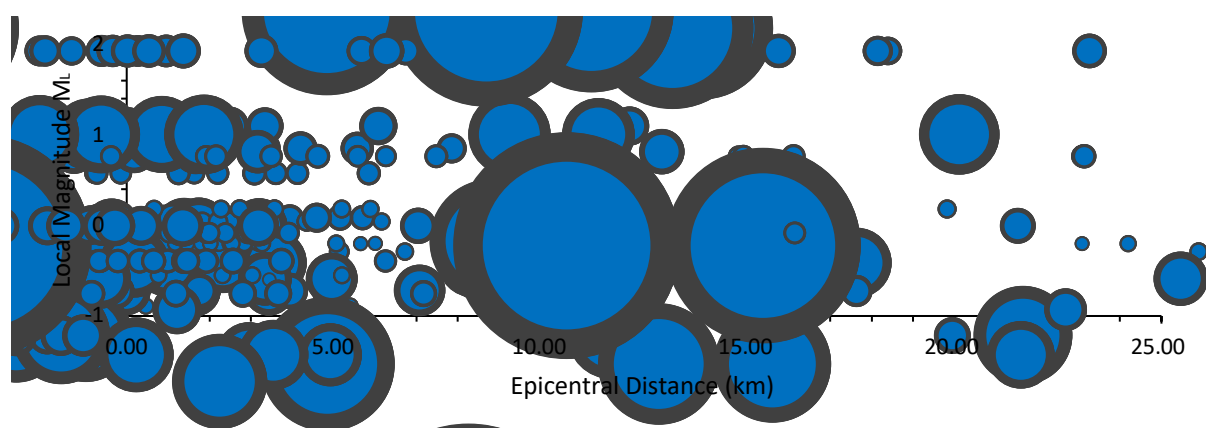


Figure 4.6. Distribution of 'usable' data in terms of distance and magnitude.

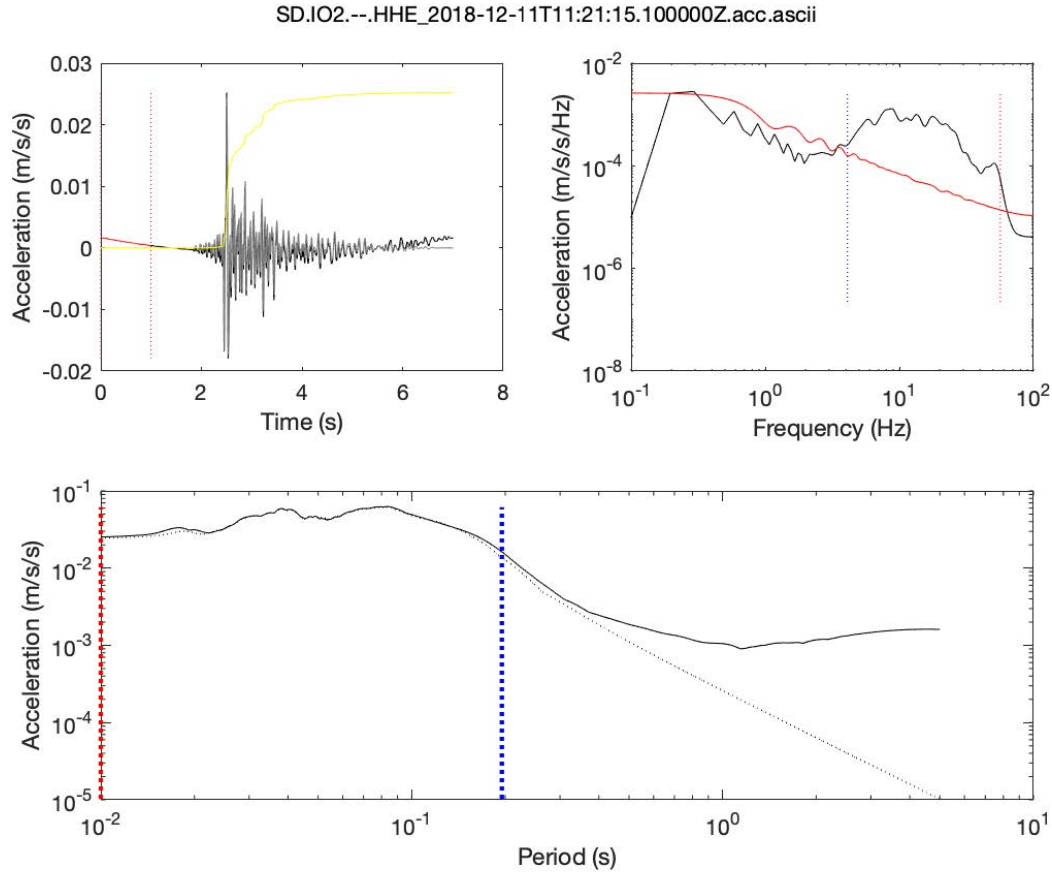


Figure 4.7. Example SNR analysis of a record of the 2018-12-11 11:21  $M_L$  1.5 event. Top left: waveform indicating pre-event noise (red) and cumulative Arias intensity (yellow) along with filtered record (grey). Top right: Fourier amplitude spectrum of acceleration time series (black) and of only the noise (red). Blue and red dotted vertical lines indicate usable range  $f_{low}$  to  $f_{high}$ . Bottom: 5% damped response spectrum of the acceleration time series (solid black line) along with usable period range  $T_{min}$  (red) to  $T_{max}$  (blue). The dotted black line is the response spectrum of the filtered time series.

Based on the SNR analysis, the usable period range for the response spectrum can be defined, which is not equivalent due to the complex interaction of input and oscillator motion (Bora et al., 2016). Based on analyses by Akkar and Bommer (2006) and Boore and Douglas (2011) we define the usable period range as  $T_{max} = 0.8/f_{low}$  and  $T_{min} = 0.01$  s (assumed equivalent to PGA) respectively. Records with  $f_{high} < 10$  Hz are discarded. For valid PGV we additionally require  $T_{max} > 0.1$  and  $f_{high}/f_{low} > 2$ .

Since the events here are small magnitude ( $M_L < 1.5$ ), they are dominated by high-frequency ( $f > 5$  Hz) signals. The usable period range is therefore limited, with no data for  $T > 2$  s (Figure 4.8). A table of usable frequency range for each record is included in Electronic Appendix C.

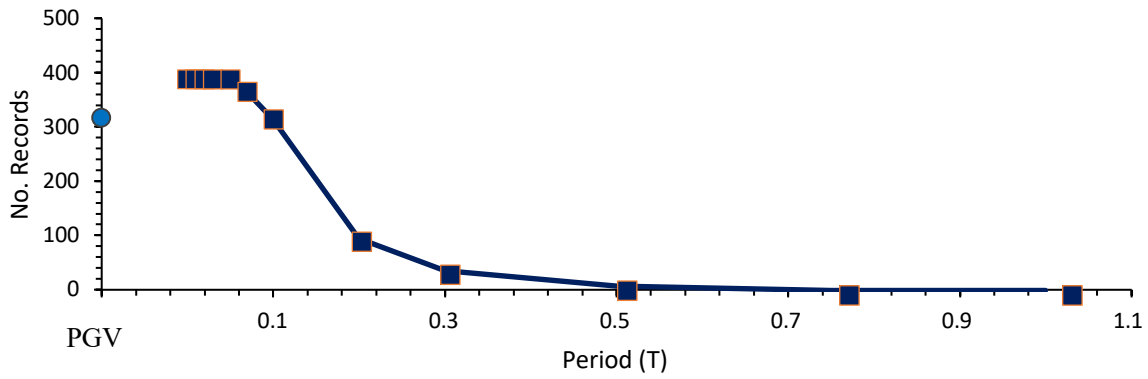


Figure 4.8. Number of usable records at selected oscillator periods.

### 4.3 Assessment of Predictive Models for PNR Ground Motions

All ground motions (within their usable period limits) have been compared to the predictions from GMPEs of Atkinson (2015) and Douglas et al. (2013) (see Section 2.3.1). Both GMPEs require moment magnitude ( $M$ ) rather than  $M_L$  which is available for the PNR events at the time of writing (see Section 2.2.1). Two conversion equations have been tested: Edwards et al. (2015) (as proposed in Section 2.2.1 for this magnitude range) since it is very similar to the empirical data from PNR-1z subsequently presented by Cuadrilla Resources (2019b), and Gruenthal et al. (2009), which is based on tectonic European events. An example is shown for the  $M_L$  1.5 event in Figure 4.9.

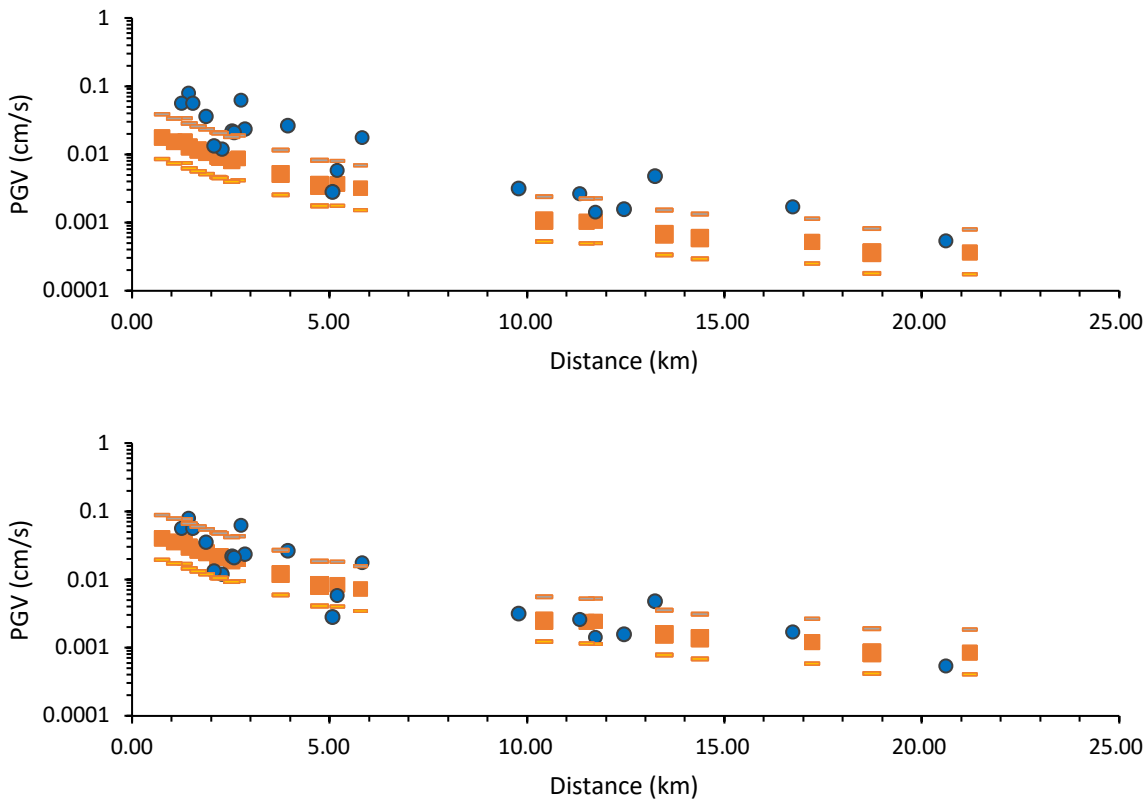


Figure 4.9. Example of recorded geometric mean horizontal PGV data (blue) and the model of Atkinson (2015) (orange, square: median; line: plus/minus one sigma). Assuming a conversion to  $M$  from  $M_L$  using (*top*) Gruenthal et al. (2009) and (*bottom*) Edwards et al. (2015).

In order to assess the full dataset, residual plots are presented (log-observed minus log-predicted spectral ordinate), using both GMPEs along with the conversion equations from  $M_L$  to  $M$  of Gruenthal et al. (2009) and Edwards et al. (2015). In the following only PGA, PGV and 0.3s PSA are presented for brevity. PSA at 0.1 and 0.2 and 0.5s are also shown in Appendix D. It should be noted that the Atkinson GMPE was calibrated only down to  $M = 3$ . We are therefore relying on a significant extrapolation in predicting motions at PNR. The Douglas et al. (2013) model was calibrated using data down to  $M = 1$ , and so relies on less extrapolation, but predictions below  $M = 1$  should still be viewed with caution.

#### 4.3.1 Atkinson (2015) GMPE using Gruenthal et al. (2009) $M$

In general, these models lead to systematic underprediction of up to a log10 unit (i.e., factor of 10). The underprediction decreases with increasing magnitude, distance and period, but always leads to biased residuals (Figures 4.10 – 4.12).

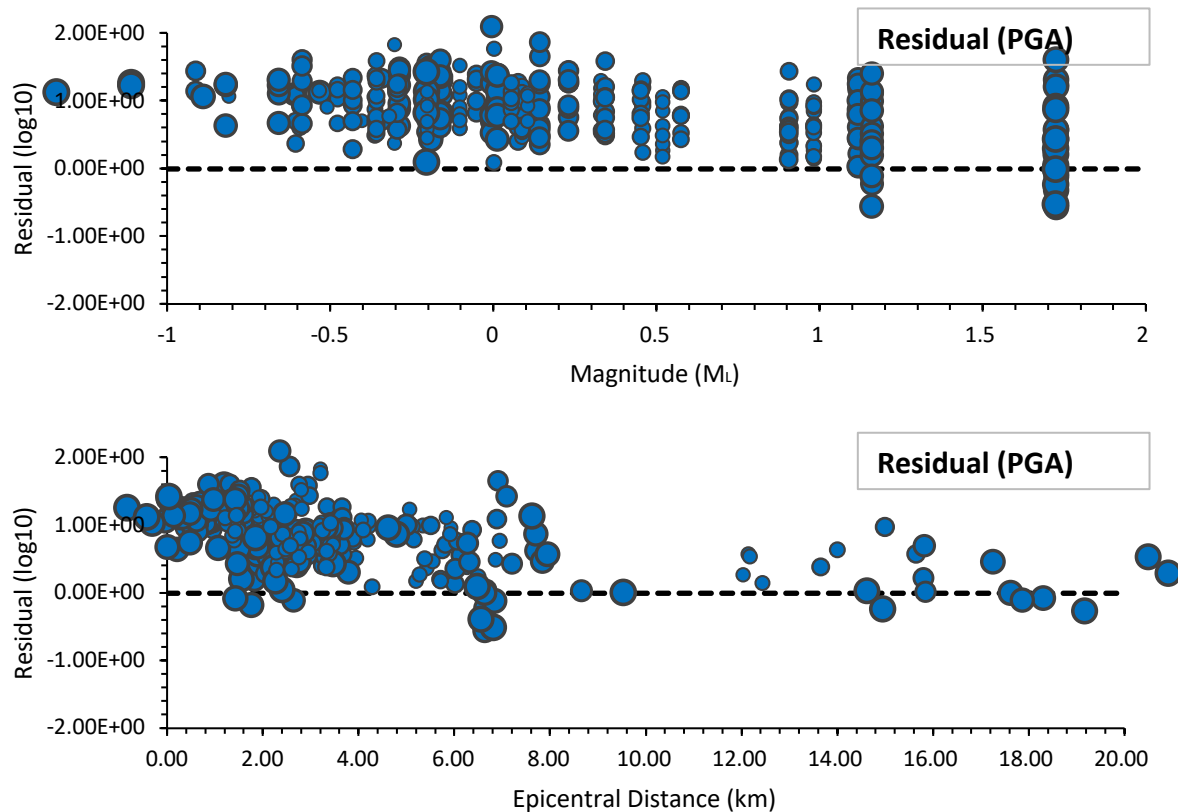


Figure 4.10. Residuals (observed – GMPE) for PGA using the Atkinson (2015) GMPE with Gruenthal et al. (2009).

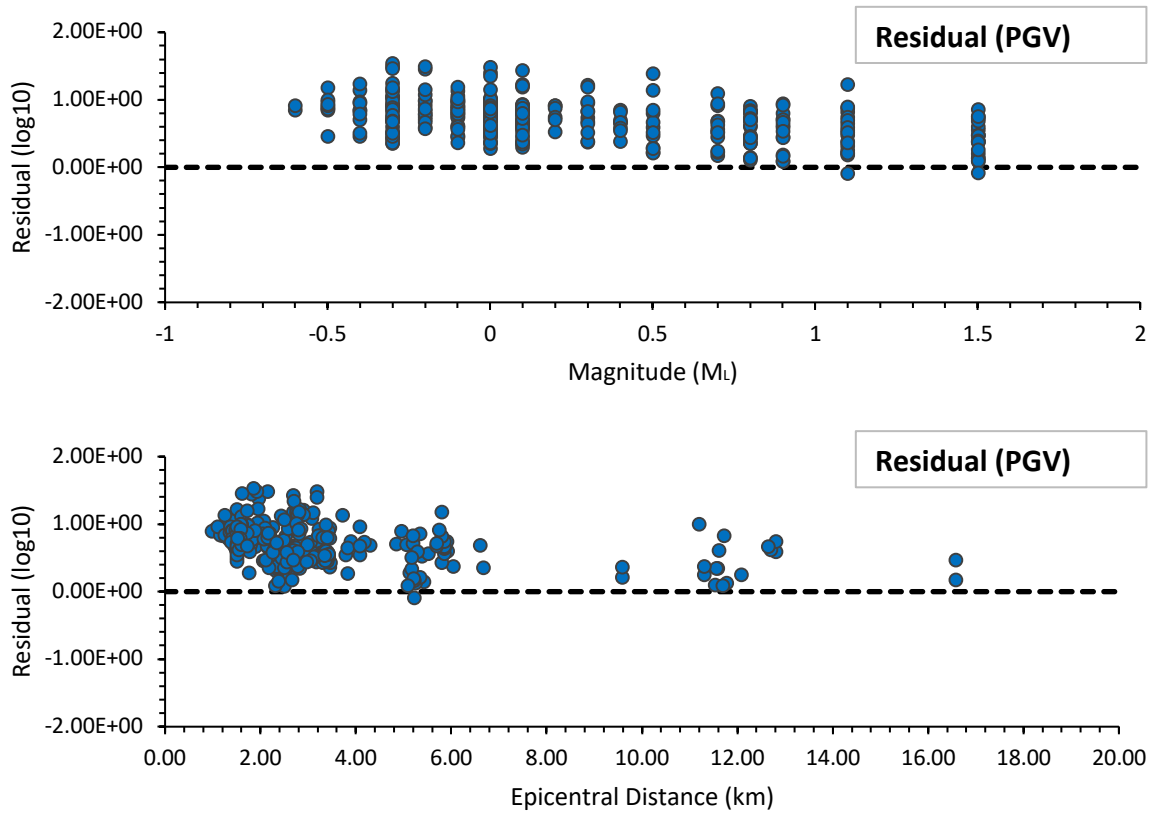


Figure 4.11. Residuals (observed – GMPE) for PGV using the Atkinson (2015) GMPE with Gruenthal et al. (2009).

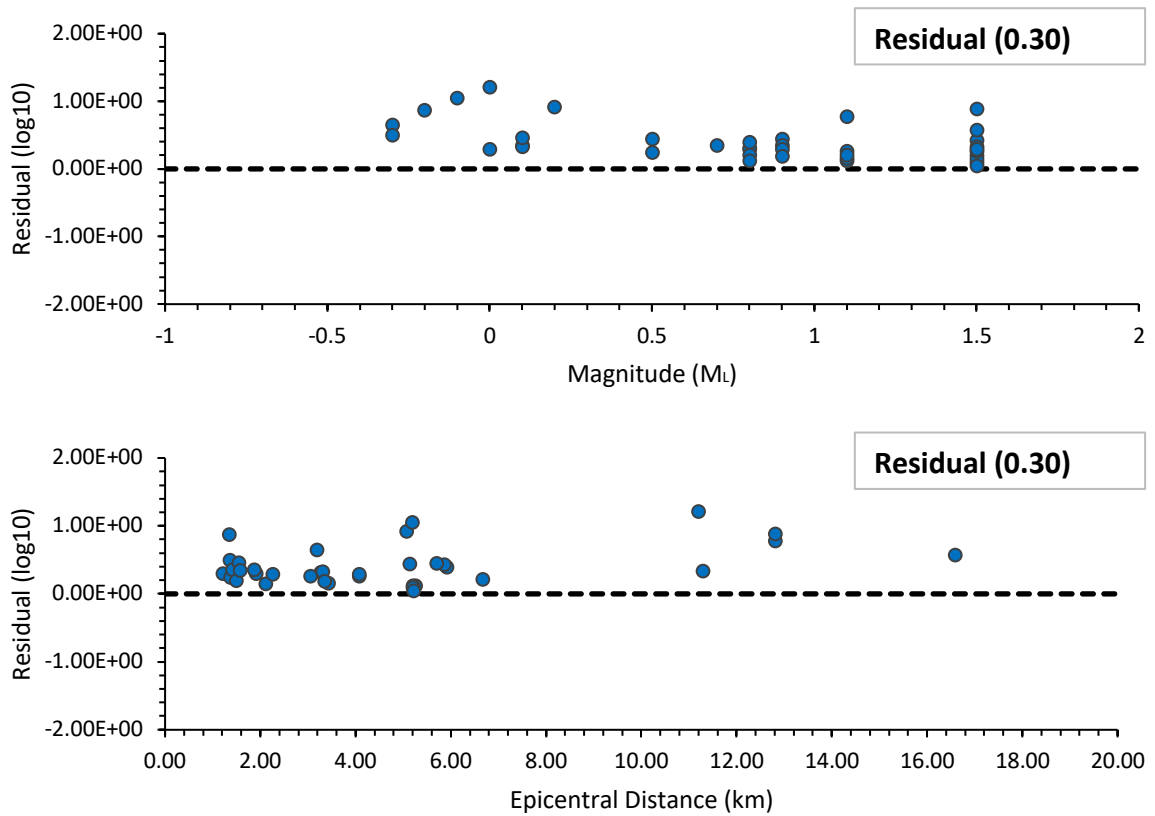


Figure 4.12. Residuals (observed – GMPE) for 0.3s PSA using the Atkinson (2015) GMPE with Gruenthal et al. (2009).

#### 4.3.1 Atkinson (2015) GMPE using Edwards et al. (2015) M

Using the ML to M conversion of Edwards et al (2015) the predictions are much closer to the observed values, with residuals centred particularly for distances greater than a few km and  $M > 0.5$ . Mid- to long-period motions (e.g.,  $T = 0.3$  s) are predicted with minimal bias across the range of magnitude and distance available in the observed data. Short to mid-period motions (including PGA, PGV) tend to show a rapid decay in the first few kilometres, with motions tending to be underpredicted (Figures 4.13 - 4.15). We note two significant outliers in Figure 4.13 and 4.14 (almost a factor 100 above the prediction, or around six standard deviations according to Atkinson, 2015). These residuals correspond to two very small events ( $M_L = 0.5$  and  $-0.2$ ) recorded at a relatively distant station (12 km away) and are likely to be noise contaminated (e.g., due to vibrations from a passing vehicle). Note that these residuals are present in all residual plots for PGA and PGV presented here (they are off-scale in Figures 4.10 to 4.11).

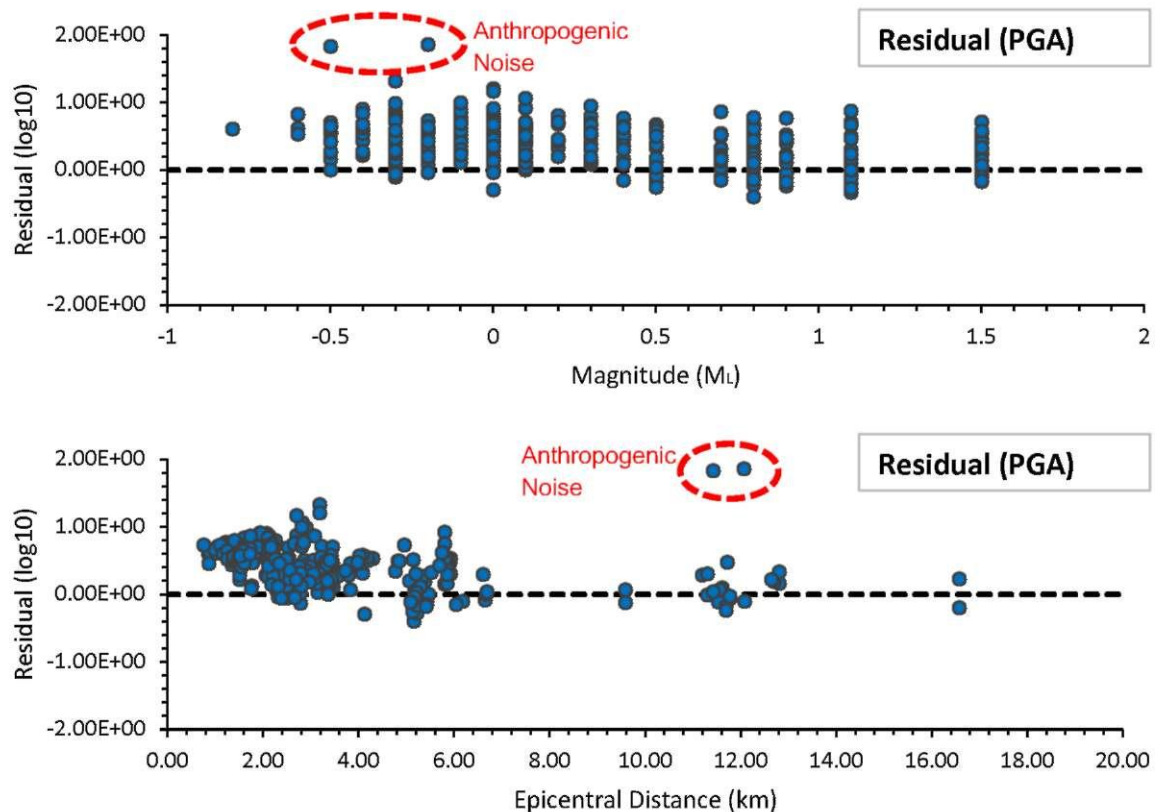


Figure 4.13. As Figure 4.10, but using the Edwards et al. (2015) ML to M conversion.

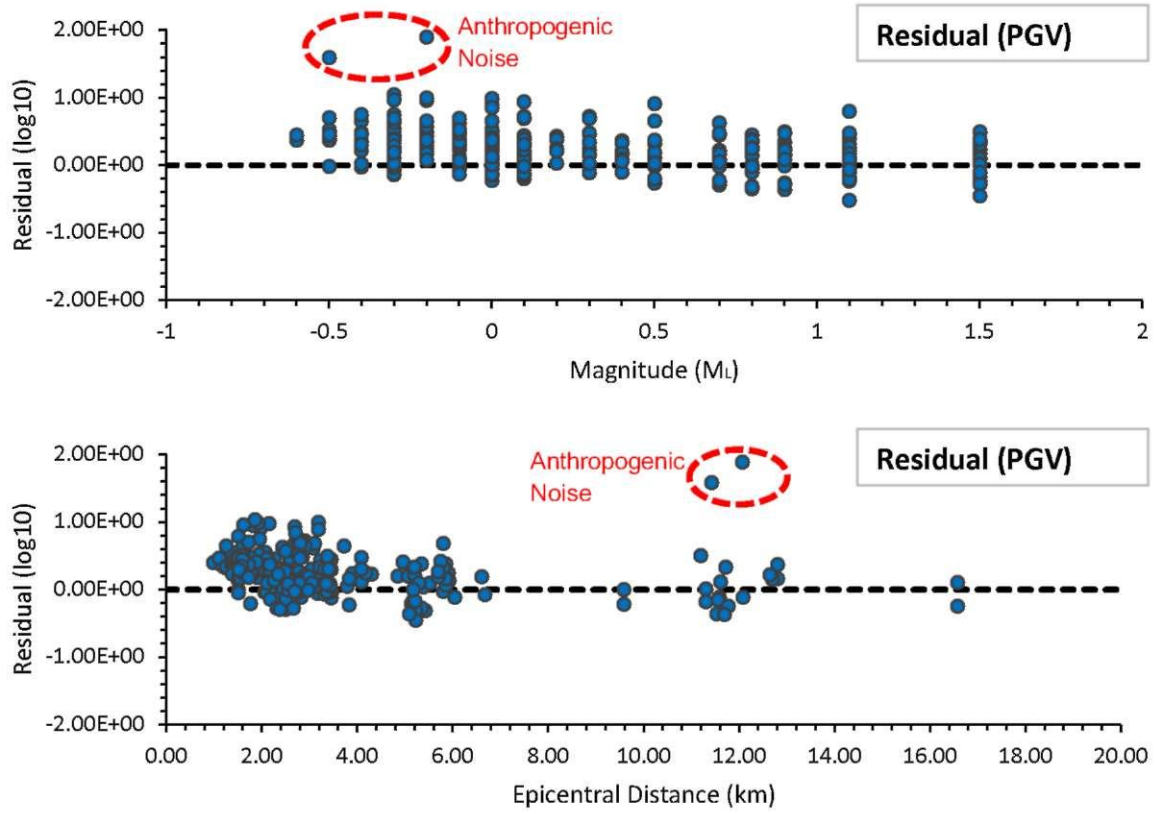


Figure 4.14. As Figure 4.11, but using the Edwards et al. (2015) M<sub>L</sub> to M conversion.

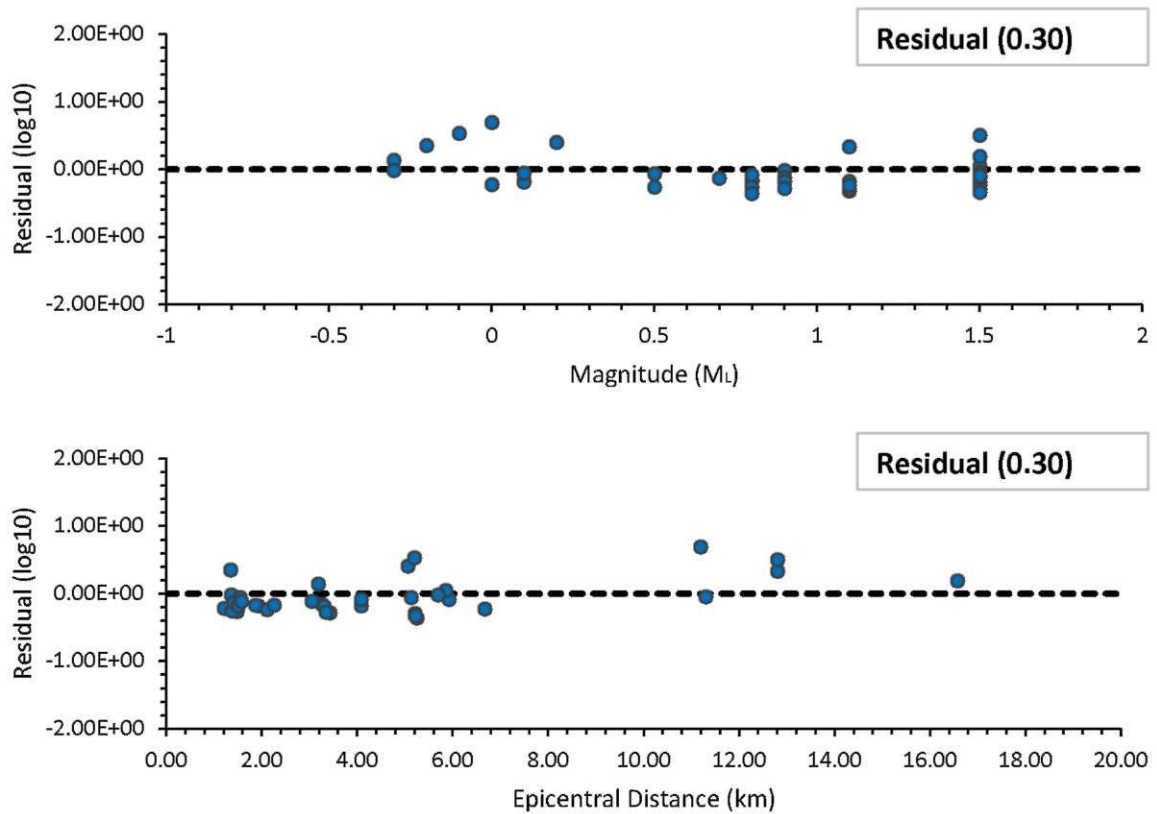


Figure 4.15. As Figure 4.12, but using the Edwards et al. (2015) M<sub>L</sub> to M conversion.

4.3.2 Douglas et al. (2013) GMPE using Gruenthal et al. (2009)  $M$

The Douglas et al (2013) model exhibits the opposite behaviour to Atkinson for PGA and PGV, with significant overprediction in the magnitude-distance range available. For the longer period ( $T = 0.3$  s) PSA, the residual behaviour is similar to that of the Atkinson (2015) model, with systematic underprediction using Gruenthal et al. (2009) conversion to  $M$  (Figures 4.16 – 4.19).

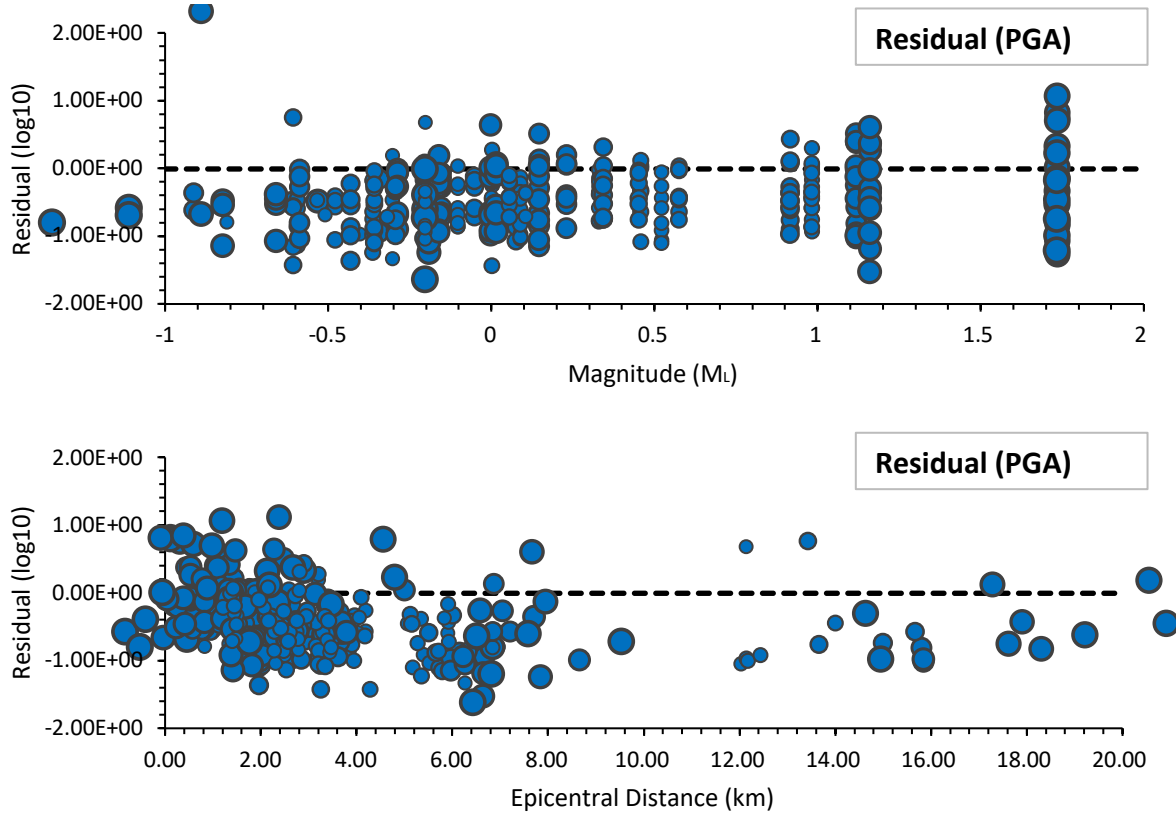


Figure 4.16. Residuals (observed – GMPE) for PGA using the Douglas et al. (2013) GMPE with Gruenthal et al. (2009).

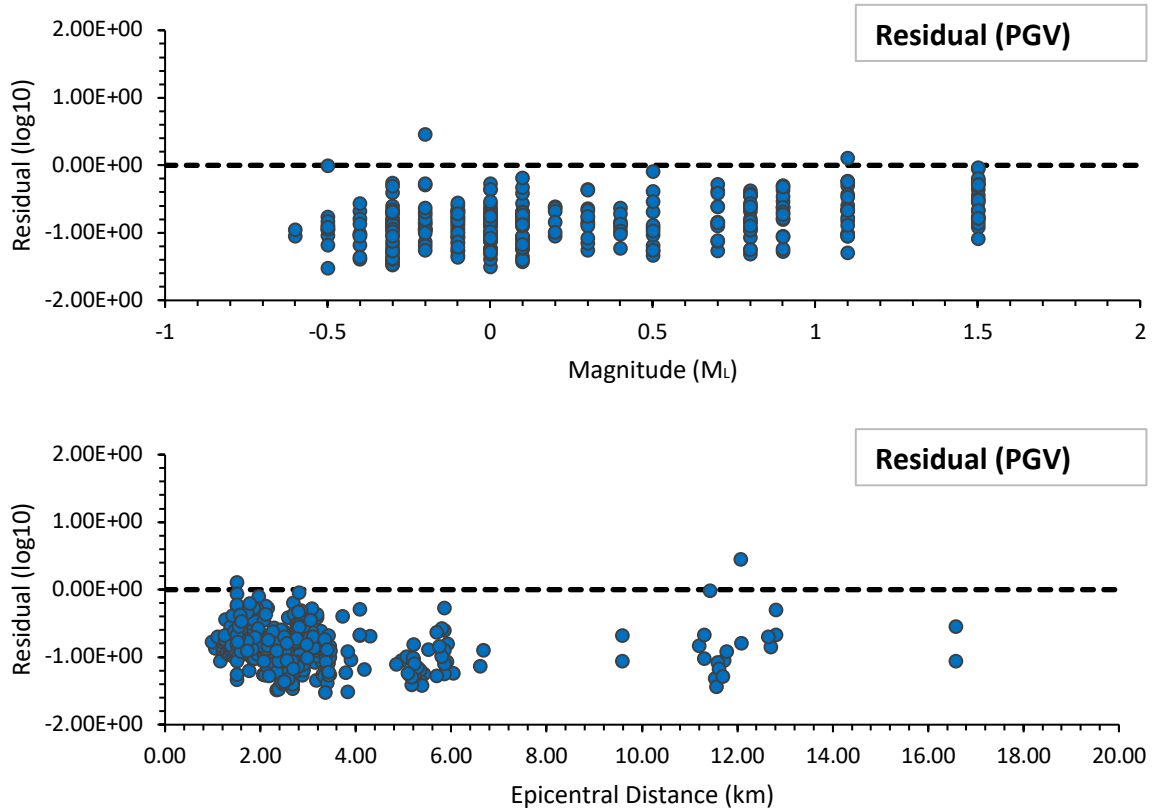


Figure 4.17. Residuals (observed – GMPE) for PGV using the Douglas et al. (2013) GMPE with Gruenthal et al. (2009).

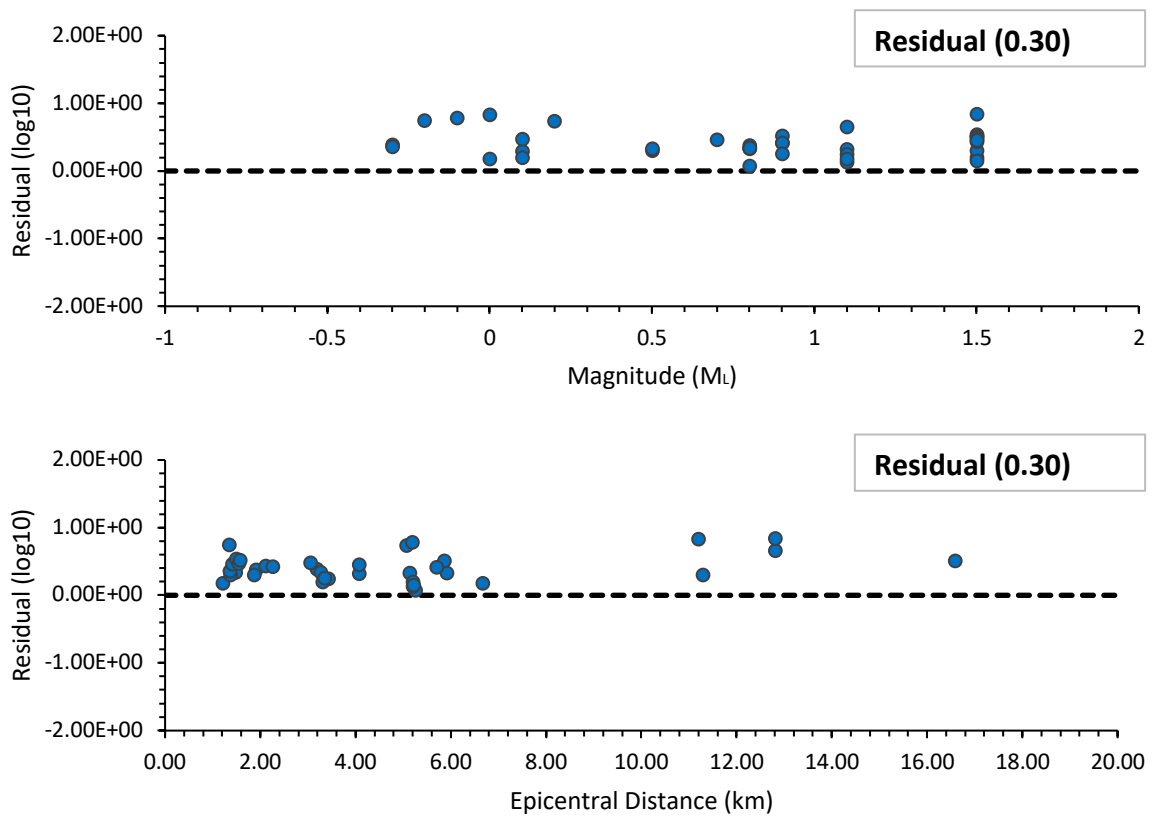


Figure 4.18. Residuals (observed – GMPE) for 0.3s PSA using the Douglas et al. (2013) GMPE with Gruenthal et al. (2009).

4.3.3 Douglas et al. (2013) GMPE using Edwards et al. (2015)  $M$

Using the Edwards et al. (2015)  $M_L$  to  $M$  conversion makes the residuals for PGA and PGV worse for the Douglas et al. (2013) model (Figures 4.19 – 4.21). The predictions at mid- to long-periods (e.g.,  $T = 0.3$  s) is in this case, however, unbiased. A trend in the residuals at very short distance (as for the Atkinson model) indicates rapid decay of the amplitudes with distance in the near-epicentre region, which is not captured in the models.

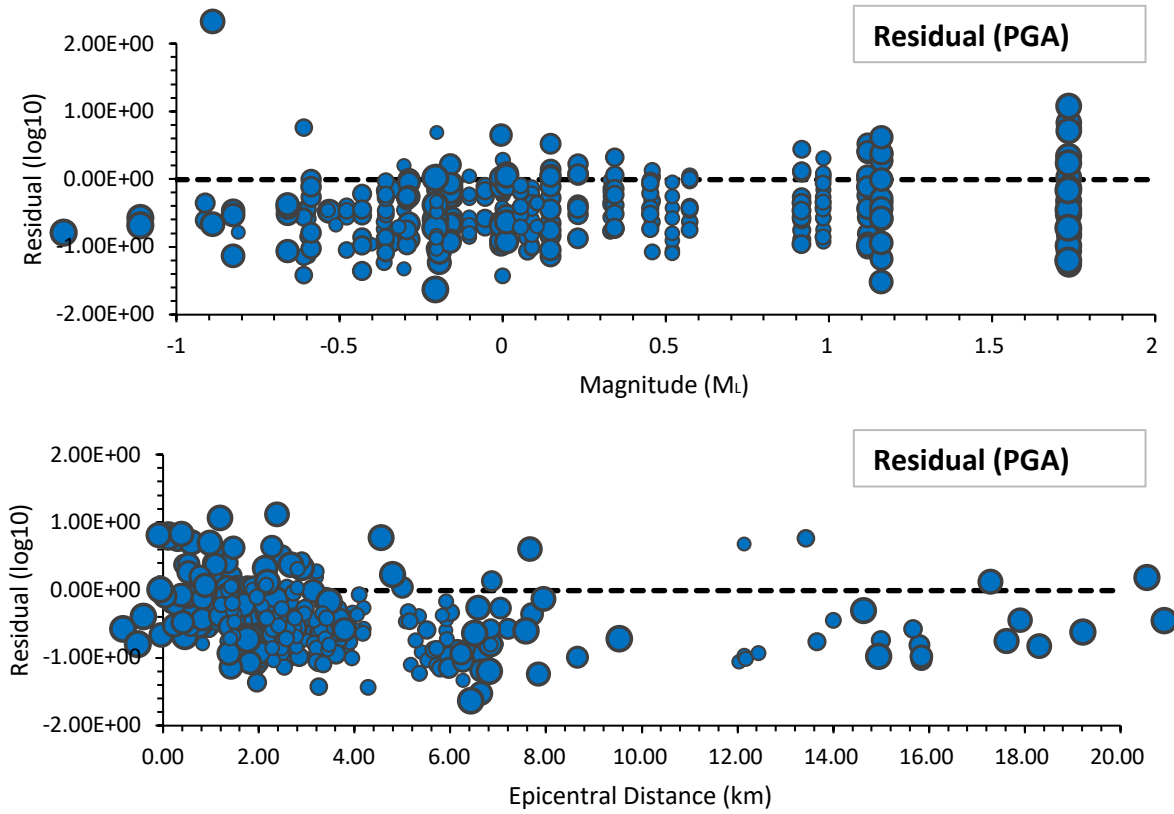


Figure 4.19. As Figure 4.16, but using the Edwards et al. (2015) conversion from  $M_L$  to  $M$ .

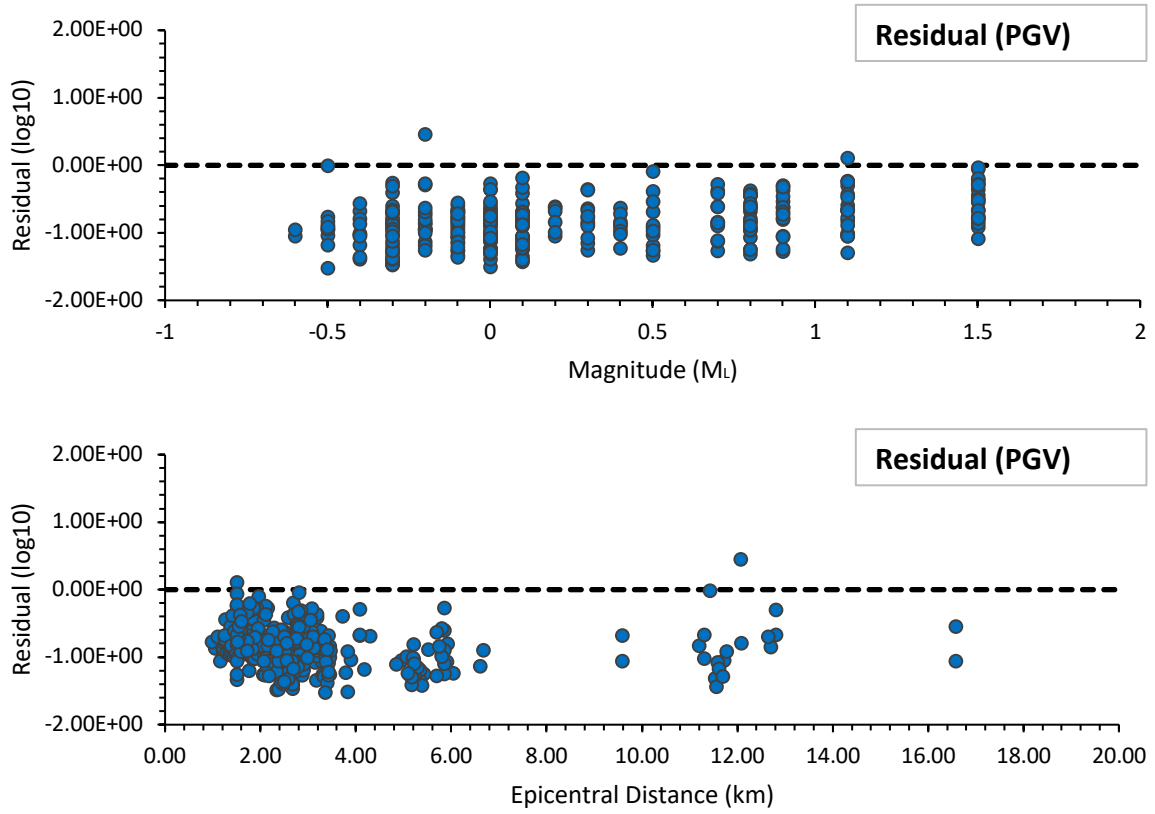


Figure 4.20. As Figure 4.17, but using the Edwards et al. (2015) conversion from  $M_L$  to  $M$ .

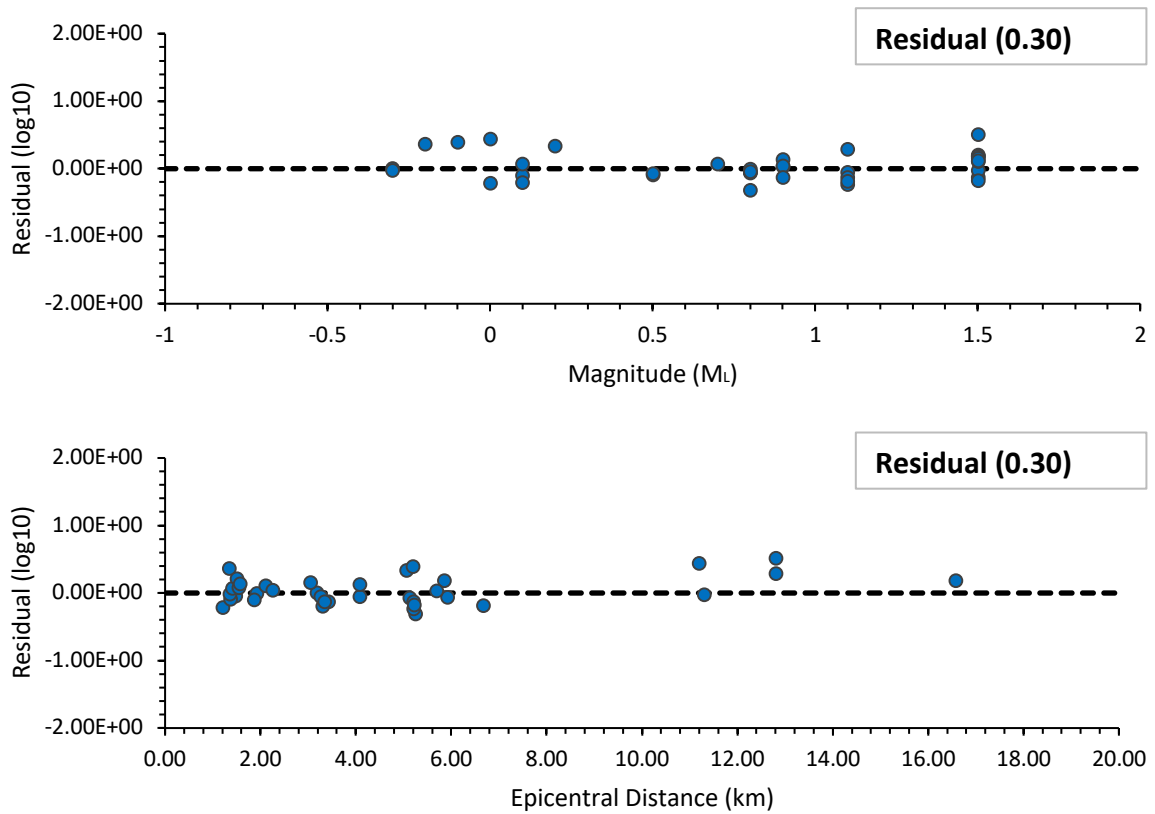


Figure 4.21. As Figure 4.18, but using the Edwards et al. (2015) conversion from  $M_L$  to  $M$ .

#### 4.3.4 Summary of Comparison

In summary, the best approach for predicting ground motions from the PNR-1z seismicity is to use the Atkinson (2015) GMPE along with the Edwards et al. (2015)  $M$  (see Section 4.3.1). Using these models the ground motions are broadly unbiased apart from at short periods, low magnitude ( $M_L < 0.5$ ) and short distance ( $R < 3$  km). Neither the Atkinson (2015) or Douglas et al. (2013) models present unbiased residuals using the Gruenthal et al. (2009)  $M_L$  to  $M$  conversion equation. Differences of up to a factor of 10 in the median observed and median predicted ground motions are evident in this case. This is at least in part due to the fact that the GMPEs are not calibrated at magnitudes as small as those at PNR so are technically not valid without careful adjustment. Overall both GMPEs seem to perform better using the conversion from  $M_L$  to  $M$  of Edwards et al. (2015), which estimates higher  $M$  (by about 0.3 units) for a given  $M_L$ . Their model was based on data from induced seismicity and focuses on events with  $M_L < 2$ , whereas the Gruenthal model is based on data dominated by larger events with  $M_L > 2$ . Reasons for different conversions are due to differences in local attenuation or source effects. Ideally, a local UK- (or PNR-) specific  $M_L$  to  $M$  equation should be defined (e.g., Dost et al., 2018). Subsequent to this analysis being completed, Cuadrilla Resources (2019b) published empirical  $M_L$  and  $M$  values for the PNR-1z dataset, which confirmed the Edwards et al. (2015) model is suitable for predicting  $M$  in the magnitude range  $M_L < 2$  (Figure 2.5).

Despite the Atkinson (2015) model being based on data  $M > 3$ , it performs the best over a wide magnitude, distance and period range. This may be due to the fact that Atkinson (2015) used a more complex functional form, including an  $M^2$  term and magnitude dependent near-field saturation of ground motions. Douglas et al. (2013) only account for linear  $M$  dependence and have no magnitude dependence in the near-field saturation term. The quadratic term captures more complex magnitude scaling behaviour, and therefore leads to better extrapolation potential. Based on these observations, while noting the limitations of comparing predictions outside the valid range, we make the following suggestion for predicting larger magnitude events at PNR.

- The Atkinson (2015) model should be used along with the  $M_L$  to  $M$  conversion of Edwards et al. (2015) for predicting ground motions from small events ( $M_L < 1.5$ ).
- Above  $M_L 2.5$ , the Gruenthal (2009) model should be used since it known to work well for UK events in this range (Rietbrock and Edwards, 2019). A transition between the conversions in the range  $M_L 1.5$  to  $2.5$  should be included to avoid a step in the  $M_L$  to  $M$  conversion relation (Figure 2.5).

The approach suggested here results in predictions for  $M_L \leq 1.5$  that are shown to be broadly unbiased with respect to recorded data at PNR. It also ensures that predictions at  $M_L > 2.5$  are well calibrated to data (albeit natural earthquakes) and use a  $M_L$  to  $M$  relation that has been shown to be suitable across the UK and Europe in the  $M_L > 2$  range. In the case that enough locally recorded events become available in the higher magnitude range ( $M_L > 1.5$ ) and the data support a revision to the approach above, the transition points between the two conversion relations can simply be revised, whilst maintaining the same rationale.

An improved, but more involved approach to local ground motion prediction (and not undertaken here due to time constraints) would be possible by adjusting the Atkinson (2015) model to fit the PNR data at low magnitude as shown by Bommer et al. (2006). This adjustment should also take into account the following:

1. Potentially lower stress drop sources for induced (shallow) events;
2. The rapid decay of motions in the near-field (distances less than 4 – 5 km).

It should be noted that the PNR ground motions may simply be characteristically different to those modelled by Douglas et al. (2013). This could, for instance be due to site effects (e.g., resonance, see Section 2.2.3) or source effects (e.g., high or low stress drop, see Section 2.2.4). Analysis beyond the scope of this work is required to determine this, however.

#### ***4.4 Comparison of Observed Motions with Anthropogenic Sources of Vibration***

Ground motions can be compared against other anthropogenic sources of vibration as a means to provide a context for the level of shaking. Construction sites and other industrial activities, for instance, generate vibrations which are limited by thresholds defined in British Standards. In addition, everyday activities, from dropped objects to desk fans and coffee machines, generate vibrations. Figure 4.22 shows a variety of shaking levels for anthropogenic sources, along with those recorded at the PNR site for the  $M_L$  1.1 and 1.5 events. Generally, the motions can be considered as almost imperceptible and well below the level of vibration that people experience going about everyday activities.

British Standard 6472 (BSI, 2008) lays out a range of acceptable maximum levels of PGV for blast-type vibrations (no more than three per day), which is appropriate for induced seismicity (Table 4.1). For residential properties a PGV of 6 – 10 mm/s are deemed acceptable during the day, reduced to 2 mm/s at night. A scaling factor is provided to reduce the acceptable levels when more than 3 ‘events’ (i.e., in this case felt earthquakes) per day are expected.

British Standard 7385-2 (BSI, 1993) defines acceptable thresholds for vibration and the levels at which cosmetic damage may occur (Figure 4.23). Finally, BS 7385-2 notes that the probability of damage approaches zero at PGV of 12.5 mm/s, consistent with the *ShakeMap* intensity IV (light shaking, no damage). British Standard 5228-2 (BSI, 2014) notes that minor damage is possible at vibration amplitudes which are greater than twice the threshold for cosmetic damage, and major damage to a building structure can occur at values greater than four times these values.

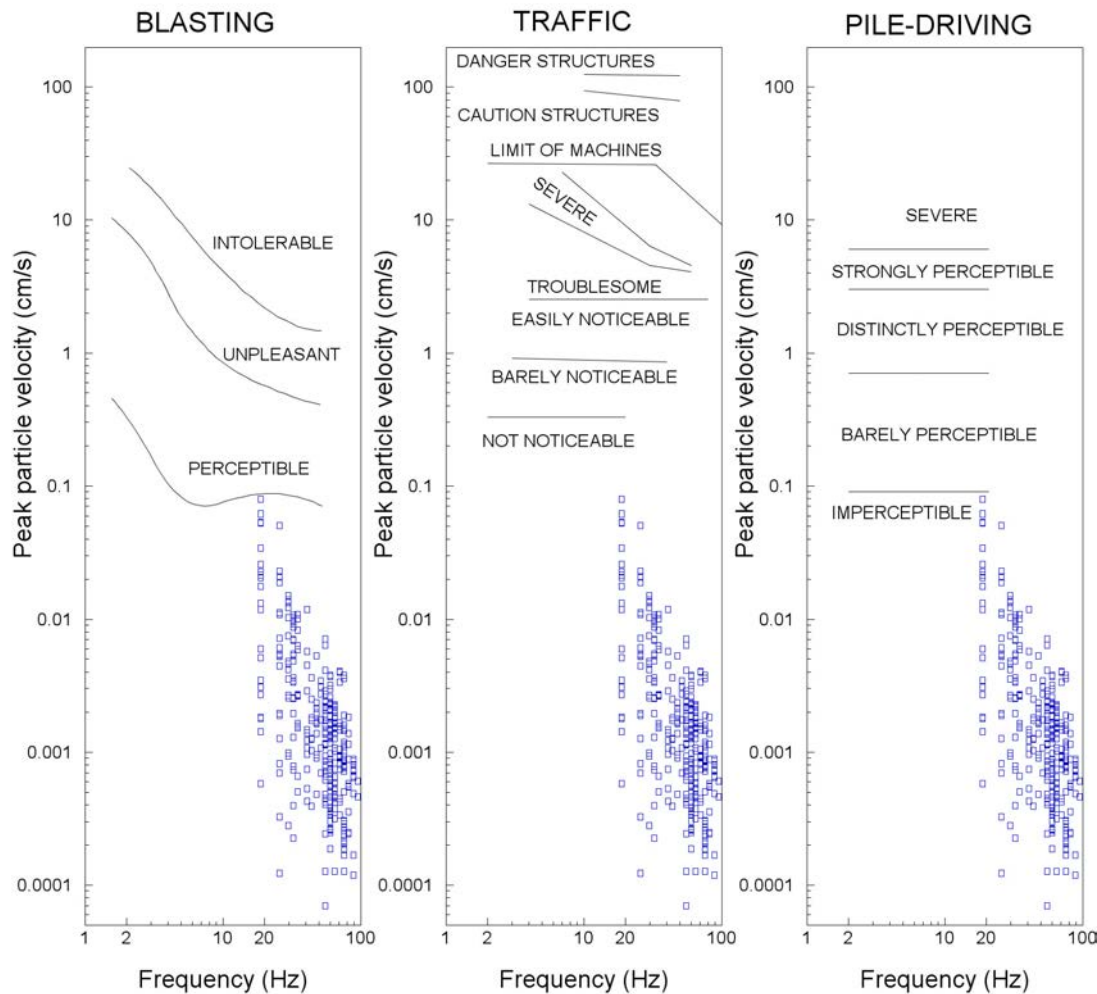


Figure 4.22. Examples of thresholds for tolerable motions defined in terms of PGV and the dominant frequency of the shaking due to blasting (left; USACE, 1972), traffic (middle; Barneich, 1985) and pile-driving (right; Athanasopoulos and Pelekis, 2000) and PGV from the PNR dataset (blue squares). Modified from Bommer et al. (2006).

Definitions of damage categories are presented in British Standard ISO 4866 (BSI, 2010), where:

- **Cosmetic:** the formation of hairline cracks on drywall surfaces, or the growth of existing cracks in plaster or drywall surfaces; in addition, the formation of hairline cracks in mortar joints of brick/concrete block construction. This is roughly equivalent to damage state 1 (DS1, see Section 2.6).
- **Minor:** the formation of large cracks or loosening and falling of plaster or drywall surfaces, or cracks through bricks/concrete blocks. This is roughly equivalent to DS2.
- **Major:** the damage to structural elements of the structure, cracks in support columns, loosening of joints, splaying of masonry cracks, etc.

Table 4.1. From British Standard 6472-2 (BSI, 2008b). Maximum satisfactory magnitudes of vibration with respect to human response for up to three blast vibration events per day.

Place	Time	Satisfactory magnitude <sup>A)</sup> ppv mm·s <sup>-1</sup>
Residential	Day <sup>D)</sup>	6.0 to 10.0 <sup>C)</sup>
	Night <sup>D)</sup>	2.0
	Other times <sup>D)</sup>	4.5
Offices <sup>B)</sup>	Any time	14.0
Workshops <sup>B)</sup>	Any time	14.0

*NOTE 1 This table recommends magnitudes of vibration below which the probability of adverse comment is low (noise caused by any structural vibration is not considered).*

*NOTE 2 Doubling the suggested vibration magnitudes could result in adverse comment and this will increase significantly if the magnitudes are quadrupled.*

*NOTE 3 For more than three occurrences of vibrations per day see the further multiplication factor in 5.2.*

- <sup>A)</sup> The satisfactory magnitudes are the same for the working day and the rest of the day unless stated otherwise.
- <sup>B)</sup> Critical working areas where delicate tasks impose more stringent criteria than human comfort are outside the scope of this standard.
- <sup>C)</sup> Within residential properties people exhibit a wide variation of tolerance to vibration. Specific values are dependent upon social and cultural factors, psychological attitudes and the expected degree of intrusion. In practice the lower satisfactory magnitude should be used with the higher magnitude being justified on a case-by-case basis.
- <sup>D)</sup> For the purpose of blasting, daytime is considered to be 08h00 to 18h00 Monday to Friday and 08h00 to 13h00 Saturday. Routine blasting would not normally be considered on Sundays or Public Holidays. Other times cover the period outside of the working day but exclude night-time, which is defined as 23h00 to 07h00.

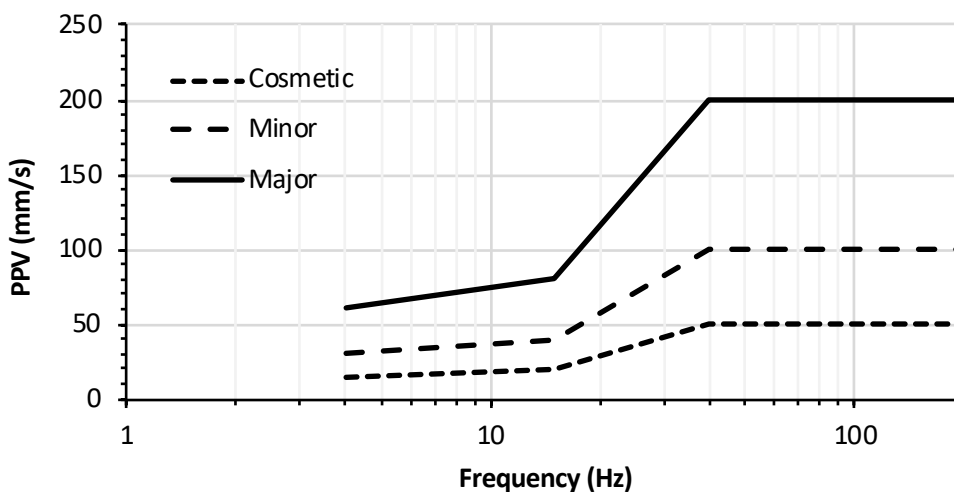


Figure 4.23. British Standard 7385-2:1993 PPV (component) thresholds for cosmetic, minor and major damage.

## 5. Assessment of Potential Impact of Future Scenarios

The following section deals with potential future earthquake scenarios and their impact on people and the built environment.

### 5.1 Proposal of Potential Induced Earthquake Scenarios

Defining possible earthquake scenarios, given the available information and state of knowledge about induced seismicity, is difficult and somewhat ambiguous. Nevertheless, we define five illustrative scenarios (with focus on the three of those in terms of intensity prediction) and, in the subsequent sections, describe the effects of those events in terms of building damage and exposure of the local population to shaking. It is worth highlighting that the work reported here was completed prior to the operator commencing hydraulic fracturing operations on a second well at PNR (PNR-2), and which led to even larger magnitude events than at PNR-1z ( $M_L$  1.5) and earlier at Preese Hall ( $M_L$  2.3). The logic behind our choice of scenarios is not altered by this increased level of seismicity (with the  $M_L$  2.9 originally considered between ‘likely to happen’ and ‘may happen’ in our scenarios).

The scenarios we consider are  $M_L = 2.5$  to 4.5 in 0.5 increments. The  $M_L = 2.5$  event is similar to a previous induced event in 2011 that led to a moratorium on hydraulic fracturing in the UK, the Preese Hall  $M_L = 2.3$  earthquake. This event therefore represents a scenario that can be considered ‘likely to happen’ (or unsurprising) at PNR, which is only 4 km from the Preese Hall site. Events of  $M_L$  3.0 and 3.5 are not appreciably larger than that this so cannot be ruled out in the future and may, for instance, occur as trailing events, despite shut in. For instance, the Basel 2006  $M_L$  3.4 event occurred during shut in after an earlier  $M_L$  2.3 event. Since the work for this report was completed a larger  $M_L$  2.9 event was recorded at the PNR-2 well, which is close to the ‘maximum magnitude’ of  $M_L$  3.1 for that well proposed by the operator (Cuadrilla Resources, 2019b). The largest events we consider are  $M_L$  4.0 and 4.5, which are considered unlikely given the UK traffic light threshold and regulatory environment (e.g., with 3D seismic imaging and extensive monitoring) in place. Nevertheless, shallow focus events of similar magnitude have occurred previously in the UK and we cannot therefore rule out that an event of this magnitude could be triggered by fluid injection into a critically stressed fault (particularly small faults with limited throw in the vicinity of the reservoir that may not have been observed by 3D seismics). It is beyond the scope of this report to assign probabilities or quantitative likelihoods to these scenarios and they are provided instead as illustrative examples to aid decision making.

### 5.2 Assessment of Potential Shaking Levels

In order to estimate the shaking level and associated macroseismic intensity we use the GMPE of Atkinson (2015) (see Section 2.3) along with the  $M_L$  to  $M$  conversion equation of Gruenthal et al. (2009) (since all considered scenarios have  $M \geq 2.5$ , see Section 2.2.1). We use three  $V_{s30}$  values (200, 240 and 280 m/s, see Section 3) to represent the site conditions across the PNR region. The GMICE of Caprio et al. (2015) (see Section 2.4.2) is used to convert predicted PGV to macroseismic intensity. Note that the GMICE is developed using largest component motion, rather than geometric mean motion, as provided by Atkinson (2015). The difference

between geometric mean and largest horizontal component, considering typical, non-polarised signals, is around 10 % for PGA (Beyer and Bommer, 2006). For the purpose of this analysis, considering the uncertainties in the GMICE predictions themselves, we consider the geometric mean predictions a suitable input for the GMICE. However, further work could investigate component-to-component variability (e.g., Stafford et al., 2019) and its impact on macroseismic intensity and ultimately risk at the PNR site.

Three of the 5 median scenarios (Section 5.1) are presented in the following,  $M_L$  2.5, 3.5 and 4.5, which we refer to as ‘likely to happen’, ‘may happen’ and ‘unlikely to happen’ respectively. The intensity scenarios are presented for the  $V_{s30} = 200$  m/s case, which represented the most strongly amplifying soil condition of the three. The  $M_L$  3.0 and 4.0 events sit between those presented in the following and are not presented for brevity. The full risk analyses (Section 5.5) is performed for all 5 earthquake scenarios and three  $V_{s30}$  values.

### 5.2.1 $M_L = 2.5$ Scenario

This scenario leads to median PGV of 0.175 cm/s in the epicentral region. This is equivalent to macroseismic intensity of III, which is felt (generally by some people indoors), but not damaging. Intensity III extends for distances of about 2 km from the epicentre (Figure 5.1). Macroseismic intensity II (scarcely felt) extends for 7.6 km from the epicentre, covering much of the Fylde region and Blackpool.

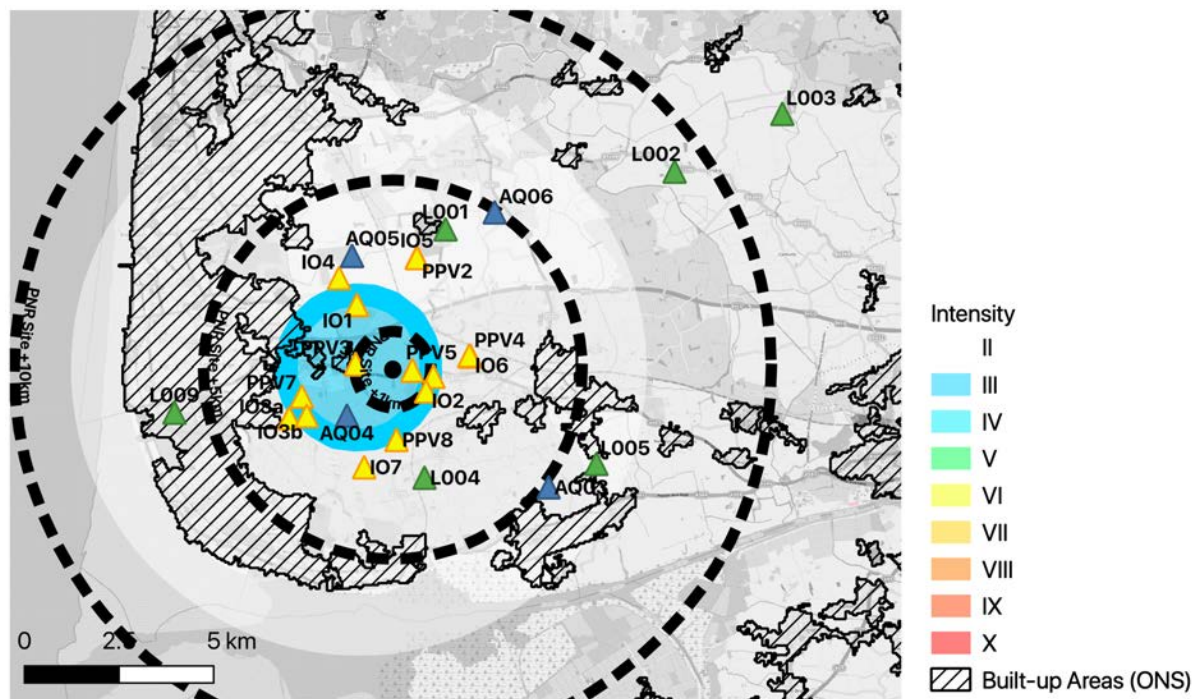


Figure 5.1. Intensity predictions (epicentral intensity III) for  $M_L$  2.5 event using median predictions of geometrical mean PGV. Seismic monitoring stations are indicated by triangles. The standard *Shakemap* (Wald et al., 2005) colour scale is used. Note the intensity contours are opaque and the fill is transparent, which may lead to slightly different colours visible.

The intensity presented in Figure 5.1 (and subsequently in Figures 5.3, 5.5) are for the median intensity from a median PGV prediction. This represents the most likely scenario for a  $M_L$  2.5 event (based on the models adopted). However, ground motions are highly variable, both from

event to event (for the same magnitude) and from site to site (for one event) (see Section 2.1.4). If we instead look for a low-probability case we can use the PGV model's standard deviation (sigma) to predict motions that lie on the 84th-percentile (i.e., plus one standard deviation). This implies not only that we have a particularly energetic earthquake, but also a particularly amplifying soil condition. It is obviously unlikely that a uniform condition like this would exist across the region (only 16 % of motions for this scenario will exceed the predicted median plus one sigma), however, we may observe pockets of high intensity motion consistent with those predicted. Figure 5.2 therefore represents the intensity possible at this level – but should not be considered a proxy for the region-wide intensity map. For the median plus one sigma prediction of geometrical mean PGV we observe a widening of the intensity III and II regions to 5 and 13 km respectively (Figure 5.2).

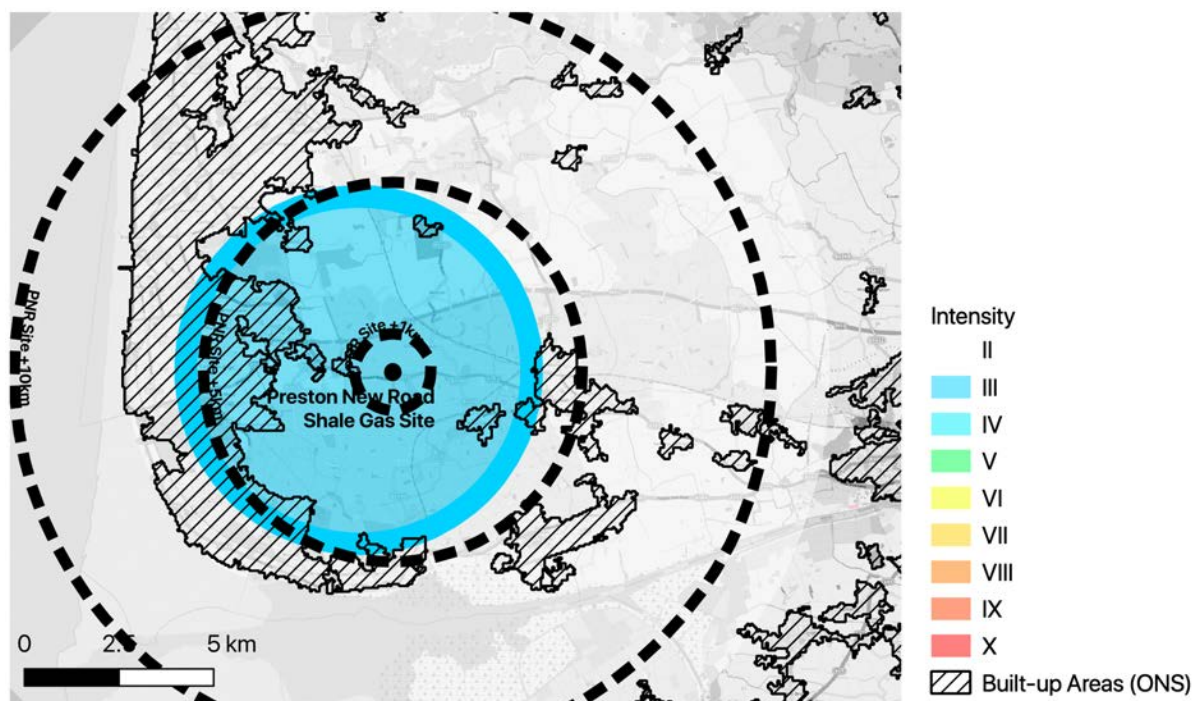


Figure 5.2. Intensity predictions (epicentral intensity III) for  $M_L$  2.5 event using median plus one sigma predictions of geometrical mean PGV. The standard *Shakemap* colour scale is used. Note the intensity contours are opaque and the fill is transparent, which may lead to slightly different colours visible.

### 5.2.2 $M_L = 3.5$ Scenario

The  $M_L = 3.5$  scenario (Figure 5.3) leads to a significant increase in the extent of felt shaking and an increase in the epicentral intensity to IV (light shaking, may cause windows and doors to rattle). The maximum median PGV is 1.5 cm/s. Intensity IV is not generally associated with damage. Intensity IV extends for approximately 5 km from the epicentre, while intensity III extends for about 15 km. While median motions are below the threshold considered potentially damaging in British Standard 7385-2:1993, the significant aleatory variability means that motions may exceed 1.5 cm/s and lead to some cosmetic damage at the epicentre with intensity V expected up to 2.5 km from the epicentre (Figure 5.4). Please see Section 5.2.1 for an explanation of the median plus one sigma predictions, which should not be considered as a likely region-wide prediction, but possible upper-estimates in some localised areas.

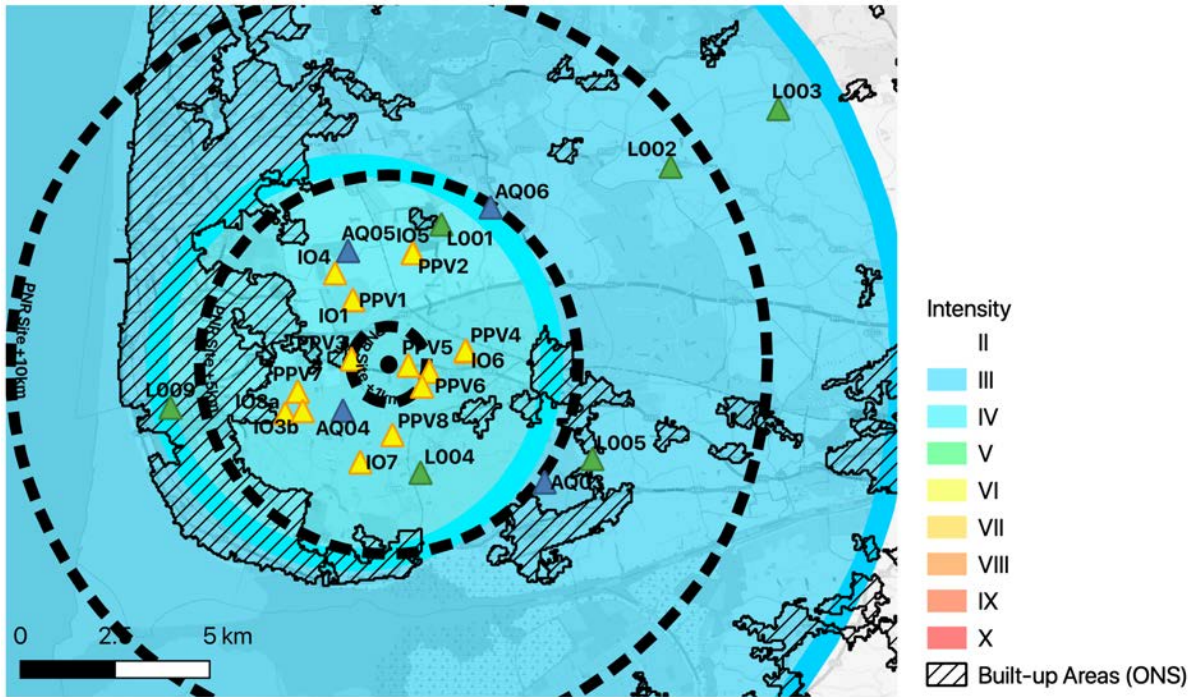


Figure 5.3. Intensity predictions (epicentral intensity IV) for  $M_L$  3.5 event using median predictions of geometrical mean PGV. Seismic monitoring stations are indicated by triangles. The standard *Shakemap* colour scale is used. Note the intensity contours are opaque and the fill is transparent, which may lead to slightly different colours visible. An electronic version may be required to distinguish between intensity III and IV.

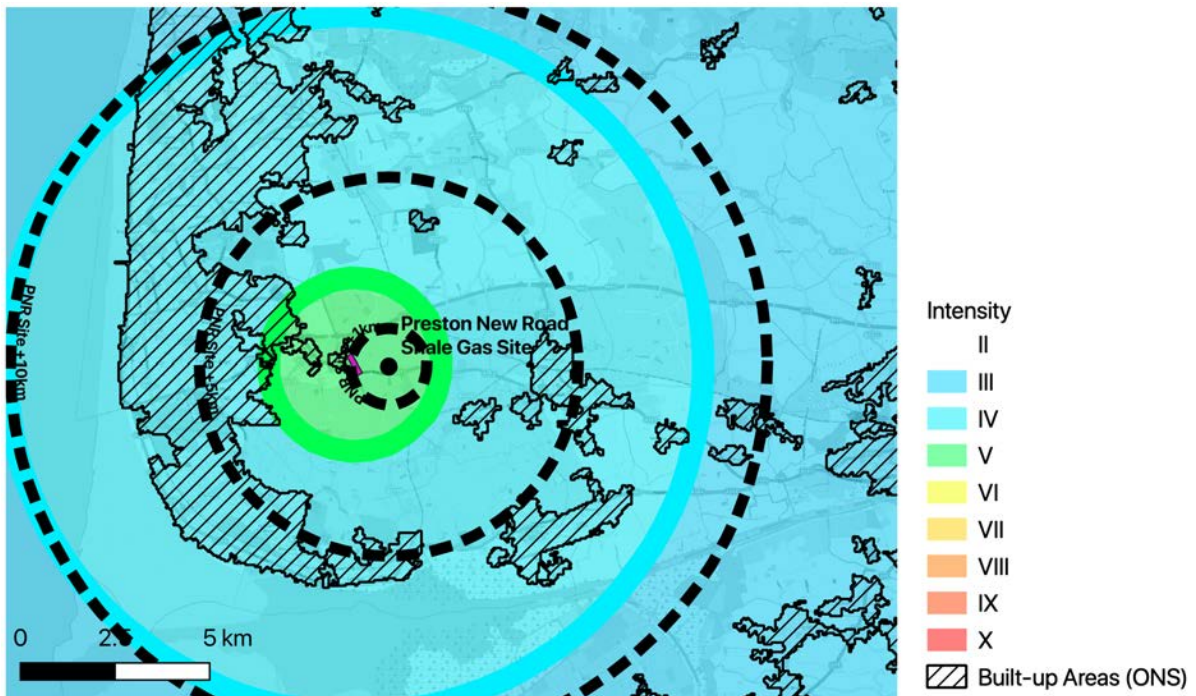


Figure 5.4. Intensity predictions (epicentral intensity V) for  $M_L$  3.5 event using median plus one sigma predictions of geometrical mean PGV. The standard *Shakemap* colour scale is used. Note the intensity contours are opaque and the fill is transparent, which may lead to slightly different colours visible. An electronic version may be required to distinguish between intensity III and IV.

### 5.2.3 $M_L = 4.5$ Scenario

This scenario (Figure 5.5) leads to damaging motions, with median PGV up to 7.8 cm/s. This is classed as intensity VI and according to the EMS-98 is associated with non-structural damage. Intensity VI extends for 3.5 km from the epicentre, while intensity V extends for almost 9 km, covering much of the Fylde coast. According to EMS-98 intensity V is not typically associated with damage. However, according to the Modified Mercalli Scale (to which EMS-98 is generally considered equivalent) intensity V may be associated with very light damage.

As previously noted, the significant aleatory variability associated with ground motions means that at one standard deviation we may see PGV of up to 16.7 cm/s in the epicentral region, which is associated with intensity VII (damaging) (Figure 5.6). This region extends for approximately 3 km using the median-plus-sigma geometrical mean PGV predictions. Here we would expect to observe many well-built buildings suffering moderate damage: small cracks in walls, fall of plaster, parts of chimneys fall down; older buildings may show large cracks in walls and failure of fill-in walls. Please see Section 5.2.1 for an explanation of the median-plus-one sigma predictions, which should not be considered as a likely region-wide prediction, but possible upper estimates in some localised areas.

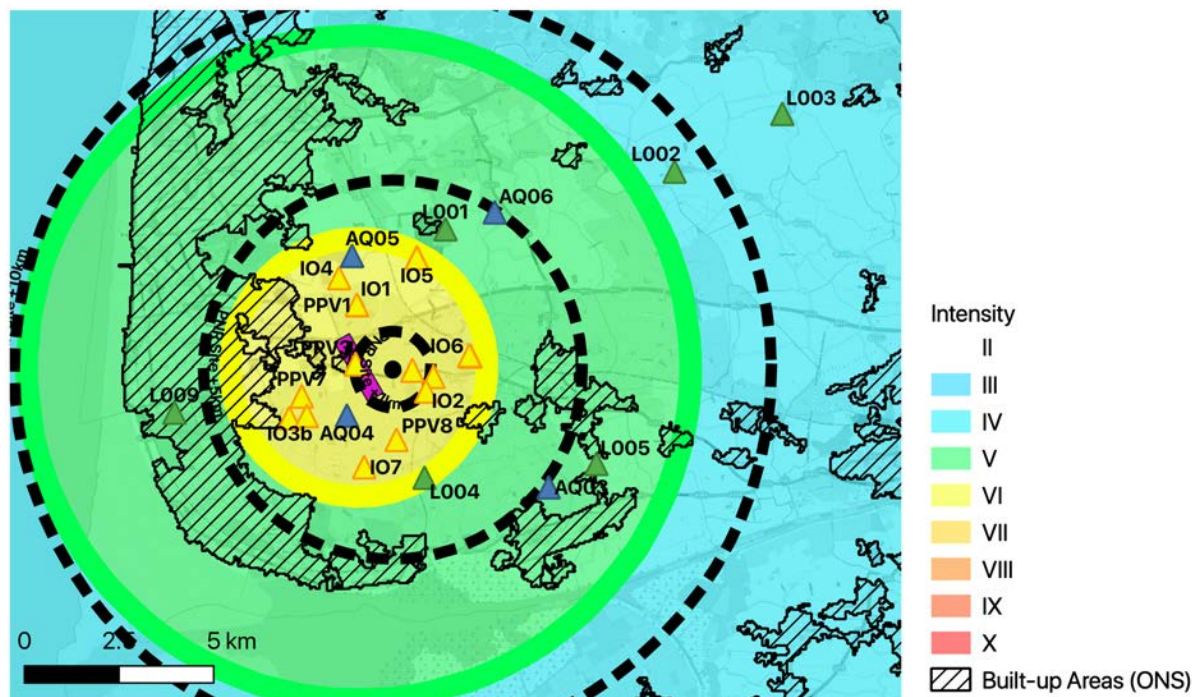


Figure 5.5. Intensity predictions (epicentral intensity VI) for  $M_L$  4.5 event using median geometrical mean PGV. Seismic monitoring stations are indicated by triangles. An example  $M_L$  4.5 fault surface projection is shown by the purple rectangle. The standard *Shakemap* colour scale is used. Note the intensity contours are opaque and the fill is transparent, which may lead to slightly different colours visible.

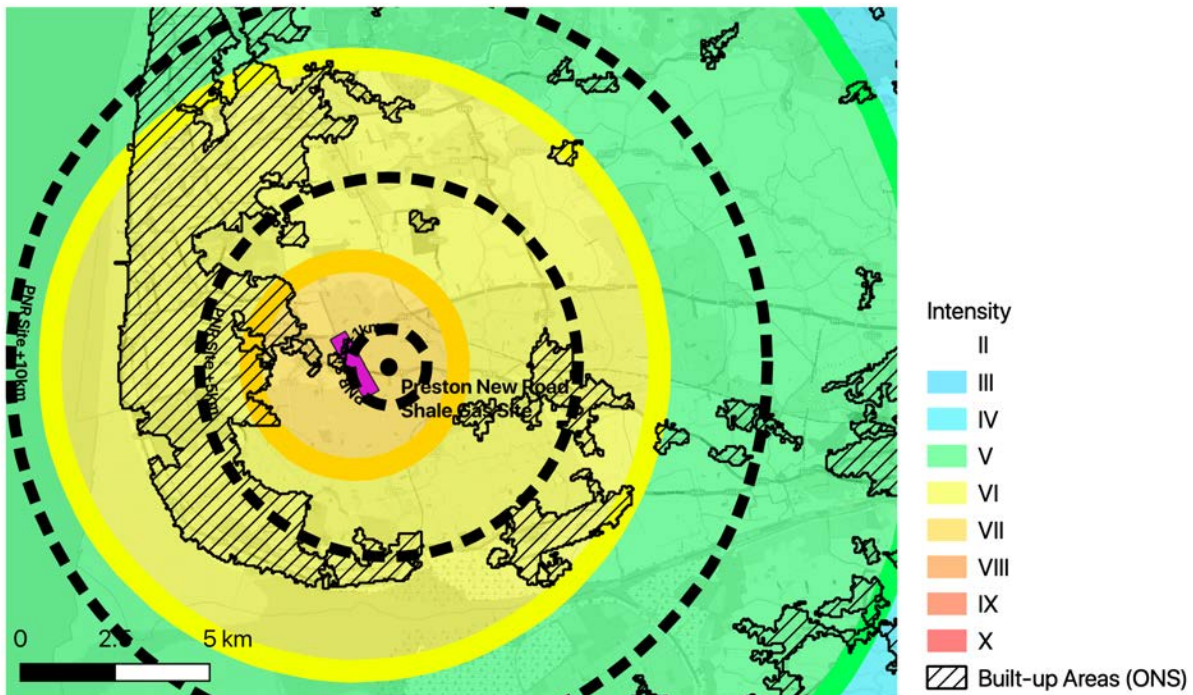


Figure 5.6. Intensity predictions (epicentral intensity VII) for  $M_L$  4.5 event using median plus one sigma geometrical mean PGV. An example  $M_L$  4.5 fault surface projection is shown by the purple rectangle. The standard *Shakemap* colour scale is used. Note the intensity contours are opaque and the fill is transparent, which may lead to slightly different colours visible.

#### 5.2.4 Scenario Ground Motion Variability

Significant aleatory variability is present in predictions of PGA, PGV and PSA, which leads to differences from site to site and event to event of a factor of up to 2 to 2.6 (depending on ground motion measure) at one standard deviation. Some 99% of the motions are expected to fall within 3 standard deviations of the median, or a factor of 6–7.8 for the Atkinson (2015) model. For risk calculations presented subsequently, we perform multiple calculations with spatially-correlated variable motions (see Section 2.1.5) with within- and between-event variability defined by the Atkinson (2015) model for geometric mean motions. As for the intensity analysis, we again do not consider and component-to-component variability (Stafford et al., 2019), which may lead to an increase in motions such as PGA. For example, Beyer and Bommer (2006) show a mean increase of 10 % in PGA between geometric mean and largest component definitions. This is, however, left open to further work. Each event has a specific between-event term randomly selected (from a lognormal distribution with standard deviation  $\tau$ ). Single-scenario variability is then applied through random sampling from a lognormal distribution with standard deviation  $\phi$ , conditioned on the spatial correlation model of Jayaram and Baker (2009). Ground motions are determined for a regular grid with 1 km spacing over a 10 by 10 km area centred around the PNR site.

#### 5.3 Inventory of Exposed Structures and Population

In order to define the risk posed by the ground motions in the scenarios defined in the previous section, we require an exposure model. This defines the building typology and vulnerability to shaking. The development of an exposure model for the PNR region is detailed in the following.

### 5.3.1 Extent of Exposure Model

The Preston New Road site is located at the following coordinate 53.78720N, -2.95103E. A 5 km buffer around this coordinate has been used to create a grid of 100 cells, each of 1 km<sup>2</sup> (see Figure 5.7). It is noted that the extent of the exposure model has been defined based on initial judgment, but it should ideally depend on the results of the damage assessment to ensure that all buildings that could be potentially damaged are included in the model. However, due to the short time scale of the project, there was a need to select the scenarios, define the ground motions and develop the exposure model in parallel. The results presented herein thus define the distribution of damage given the selected exposure region, and even though they are therefore presented in terms of percentage of buildings present in the exposure model, they may not fully represent the distribution of damage for the larger scenario events considered herein.

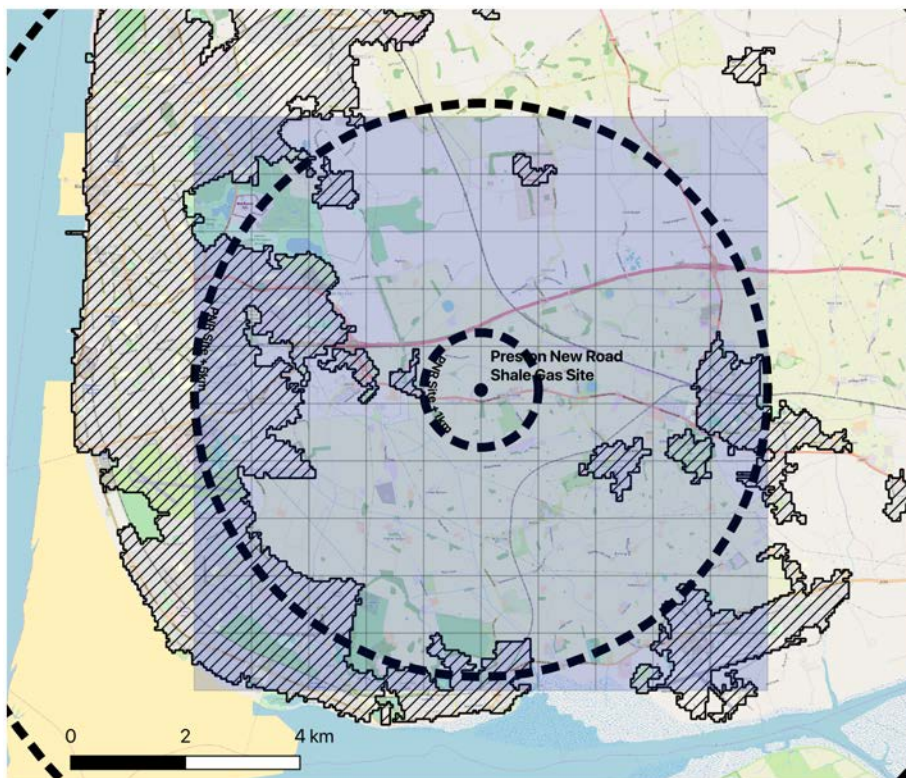


Figure 5.7. Extent of the exposure model. The point shows the coordinate of the Preston New Road site and circles indicate  $\pm 1$  and  $\pm 5$  km. The grid (blue) is 10 x 10 km at 1 km intervals.

### 5.3.2 Datasets

A number of different open datasets have been obtained and combined to produce an inventory of the exposed structures and population within the region of the Preston New Road site. A brief summary of each dataset is provided below:

- [1] OpenStreetMap (<https://www.openstreetmap.org>) Date accessed: 22/05/2019
- [2] World Pop ([www.worldpop.org](http://www.worldpop.org) - School of Geography and Environmental Science, University of Southampton; Department of Geography and Geosciences, University of Louisville; Departement de Geographie, Universite de Namur) and Center for International Earth Science Information Network (CIESIN), Columbia University (2018). Global High Resolution Population



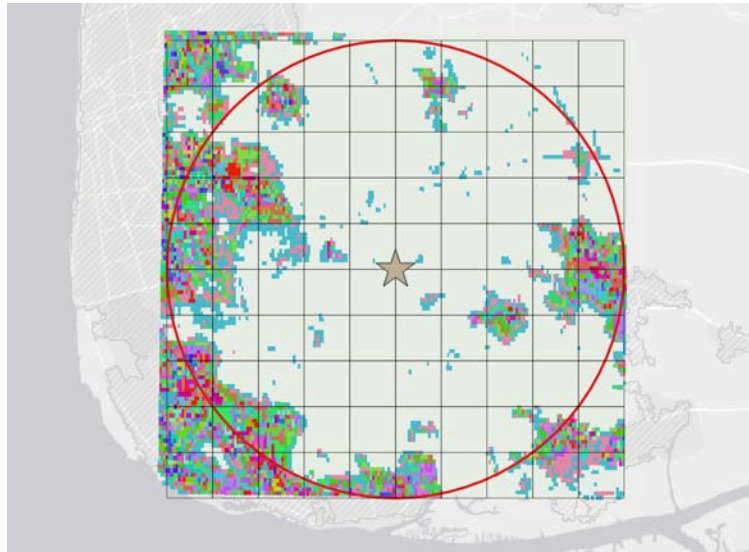


Figure 5.9 Worldpop geotiff for the region of interest.

*CORINE Land Cover* [3] (Figure 5.10) is an inventory of European land cover with 44 different classes. The classes of importance to this project are the following: urban, industrial or commercial, rural (non-irrigated arable land, pastures and broad-leaved forest) and sport and leisure as different building types were observed in each of these classes during the field trip (described further below). By overlaying the OpenStreetMap footprints on the land cover classes (Figure 5.11), an estimate of the percentage of buildings in each land use category in each grid cell has been made. These percentages are then used with the mapping schemes (described further below) to identify the number of buildings of each building class within each grid cell.

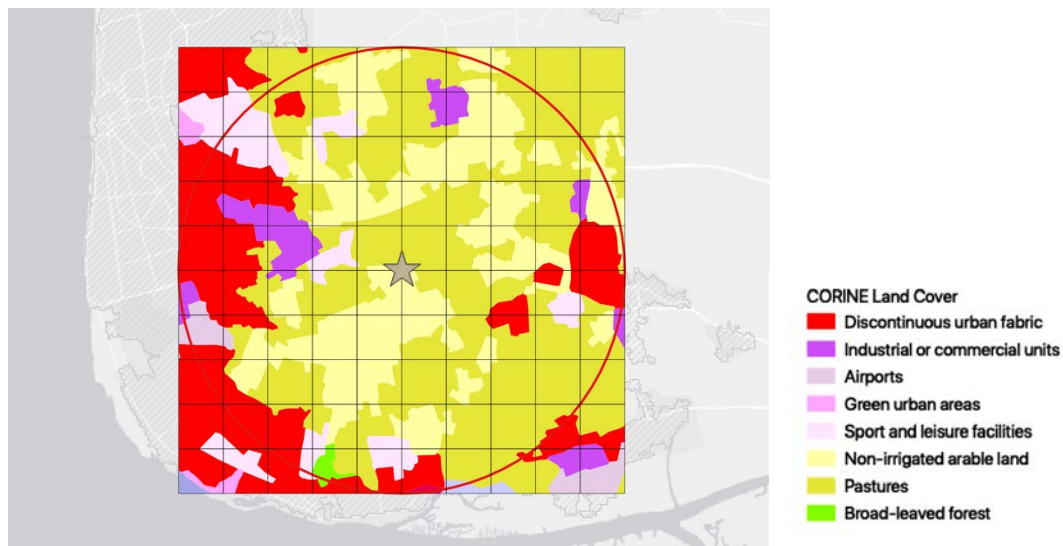


Figure 5.10. CORINE Land Cover classes within the exposure model grid.

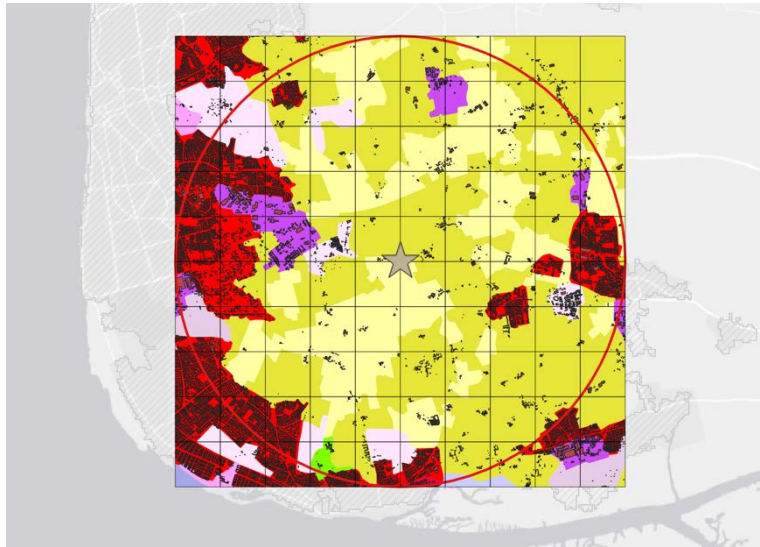


Figure 5.11. OpenStreetMap footprints overlaid on the CORINE Land Cover classes.

*Consumer Data Research Centre (CDRC) ‘dwelling age’ map* [4] is a map of the modal age of dwellings for each Lower Layer Super Output Area (LSOA) in England and Wales based on data provided by the Valuation Office Agency. The underlying dwelling age data is also supplied, grouped in approximately ten-year age bands (+ a pre-1900 catch-all), with a count of the number of houses in each band. The area covering the exposure model is presented in Figure 5.12. The data that has been extracted for the region shows that only around 15% of the buildings have been constructed pre-1919 (which is used in the assignment of the chimney fragility functions).

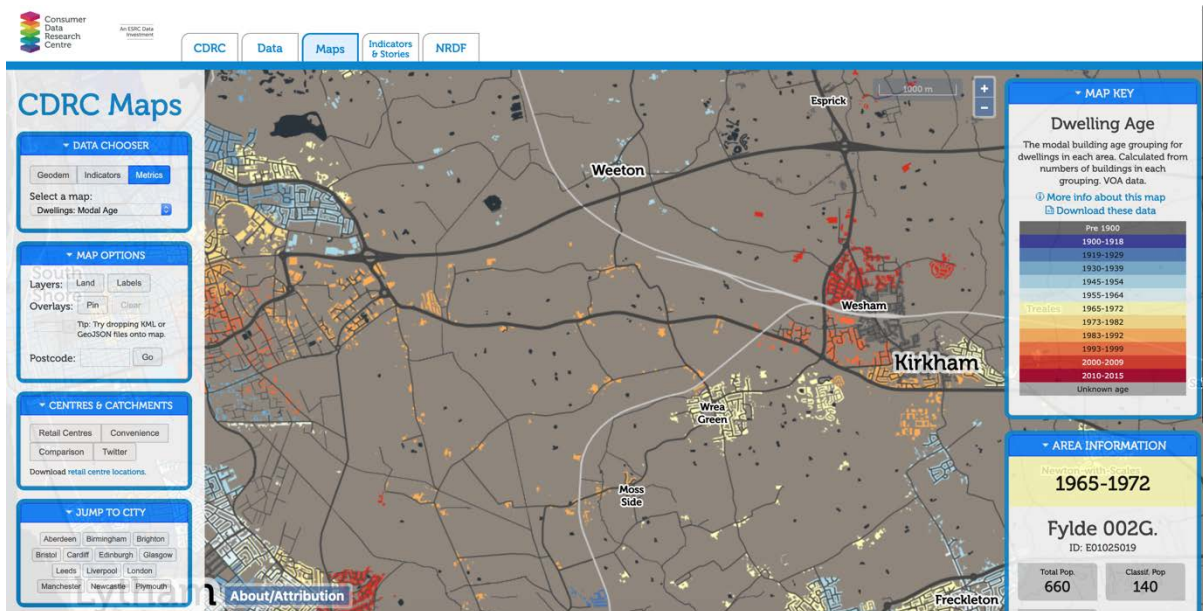


Figure 5.12. CDRC dwelling age map.

### 5.3.3 Field Trip (9<sup>th</sup> June 2019)

On Saturday 9<sup>th</sup> June, consultants Rui Pinho and Helen Crowley spent the day visiting the rural villages (Little Plumpton, Great Plumpton, Westby), urban zones (Wrea Green, Ribby, Wesham), industrial parks (Whitehalls Business Park and areas in Wesham) and sports and leisure areas (Ribby Hall Village, Carr Bridge residential park) within the region of interest. Some of the main building classes found within each land cover class (i.e., rural, urban, industrial and sports/leisure) are described below. Only visual external inspections of the buildings from street level were carried out during the site trip.

#### *Rural*

The predominant building class found within the rural areas comprises older unreinforced brick masonry detached and semi-detached housing with 2 storeys, and typically with tall brick chimneys (see Figure 5.13).



Figure 5.13. Detached two-storey brick masonry buildings with tall brick chimneys.

#### *Urban*

Within the urban residential areas, a predominance of more modern semi-detached, detached and terraced housing was found (Figure 5.14), often with shorter brick or prefabricated metal chimneys. Many of these buildings are likely to have cavity walls, as this became common during the inter-war period and mandatory in 1935.



Figure 5.14. Modern masonry housing (terraced, semi-detached) without tall brick chimneys.

### *Industrial*

The industrial building stock (of factories and large retail outlets) that was observed during the site visit comprised light steel frame construction, with bracing in the longitudinal direction (and also on the roof) and moment frames in the transverse direction (Figure 5.15).



Figure 5.15. Light steel frame buildings in Whitehalls Business Park.

### *Sports/Leisure*

Two different sports/leisure areas were visited: Ribby Hall Village and Carr Bridge residential park (Figure 5.16). The former was made up of a large number of different small units, some of which resembled static mobile homes and others that resembled detached bungalows and houses. Instead, at Carr Bridge, all of the houses were comprised of static mobile homes.



Figure 5.16. Static mobile and detached houses in sports/leisure areas (top left: mobile housing in Carr Bridge, top right and bottom: detached housing in Ribby Hall village).

### 5.3.4 Mapping Scheme

In order to estimate the number and distribution of different building classes across the region of the exposure model, a judgment-based mapping scheme has been used that assigns a percentage of each building type based on the land use class. The observations made during the site visit, as well as subsequent desk studies using Google Street View, have been used to identify the predominant building classes and their distribution in each land use class. Table 5.1 shows the proposed mapping scheme. The number of buildings in each grid cell for each building class is calculated by multiplying the total number of buildings (from the OpenStreetMap footprints), by the percentage of each land cover class (from the CORINE dataset), by the proportions from the mapping scheme (Table 5.1).

It has further been assumed that 15% of the brick masonry buildings have been constructed pre-1920, and 100% of these have brick chimneys, and 85% are from the post-1920 era, and 50% of these have brick chimneys. There are a total of 12,261 buildings with chimneys in the exposure model.

Table 5.1. Proposed mapping scheme.

Building Class	Rural	Urban	Industrial	Sports/Leisure
Brick masonry detached	0.9	0.6	-	0.2
Brick masonry terraced	0.1	0.4	-	-
Mobile home	-	-	-	0.8
Light steel frame	-	-	1.0	-

### 5.3.5 Exposure Maps

Figure 5.17 shows the population within the exposure model and Figure 5.18 shows the distribution of buildings (of each class).

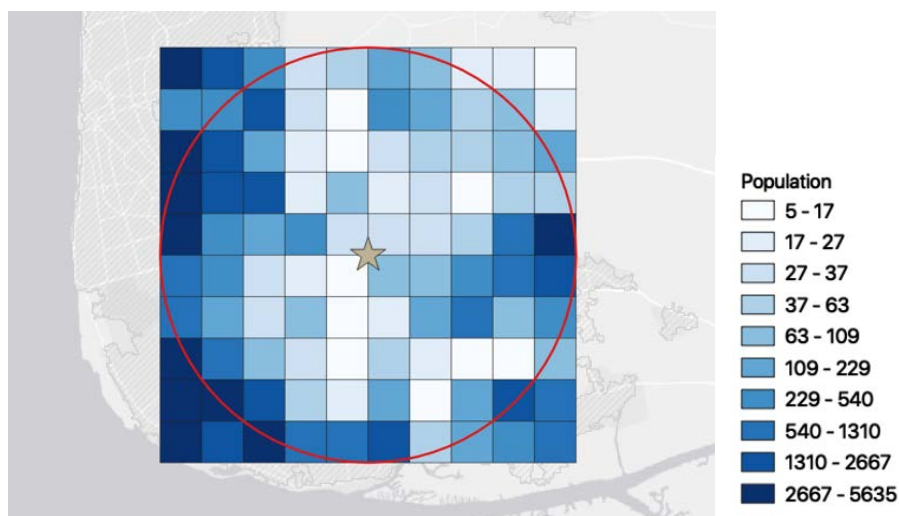


Figure 5.17. Distribution of population in the exposure model.

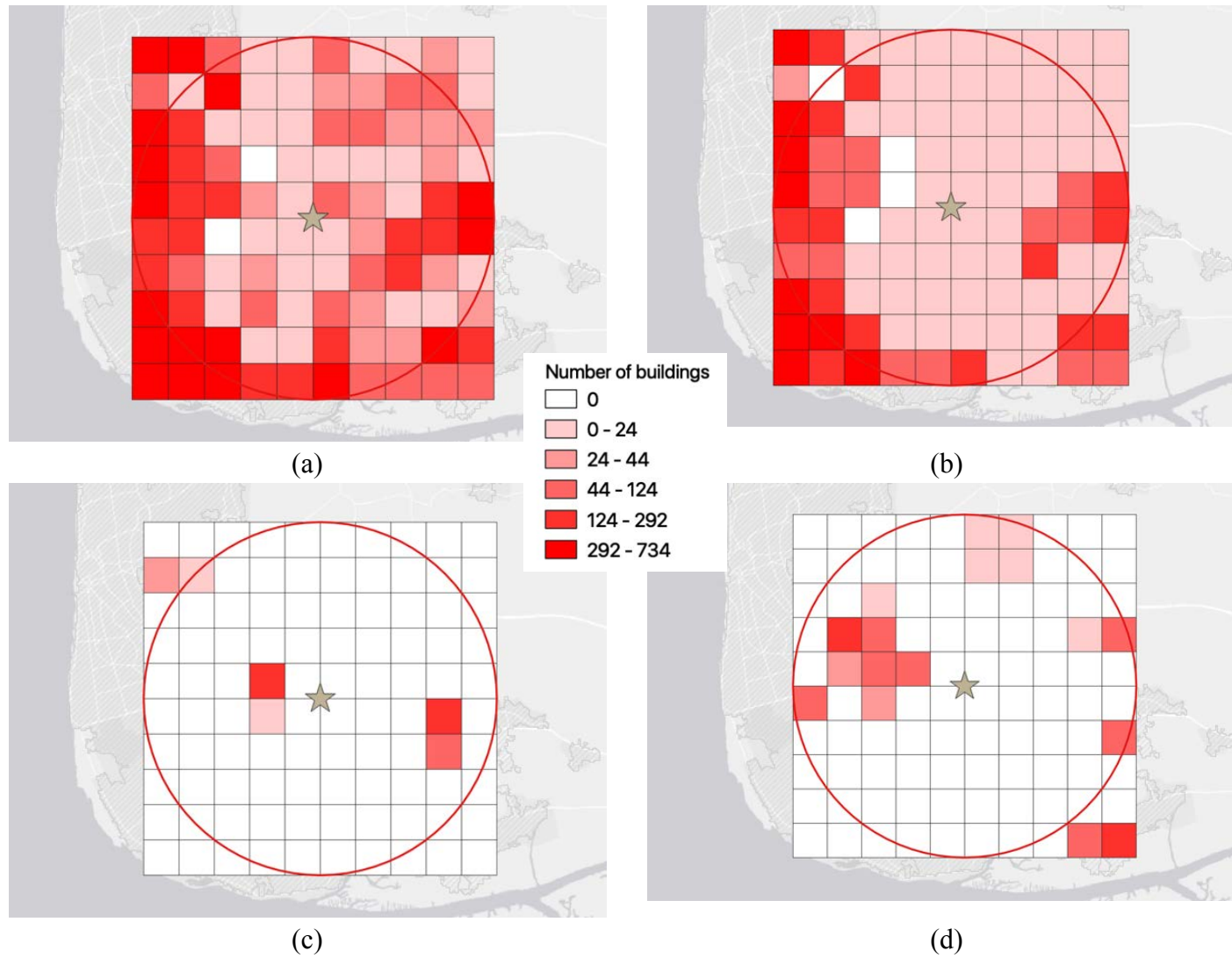


Figure 5.18. Distribution of each building class in the exposure model (a) brick masonry detached, (b) brick masonry terraced, (c) mobile home, (d) light steel frame.

**5.4 Assessment of Potential Impact on the Local Community**

Here we estimate the exposure of the *local* population to median levels of PGV and macroseismic intensity for three scenarios  $M_L$  2.5, 3.5 and 4.5. This is estimated by combining the Worldpop data (Figure 5.18) with the predicted PGV and intensity within each square of the grid. Note that we focus only on the 10 x 10 km grid around the PNR site. It is clear from Figure 5.19 (shown for the median  $M_L$  4.5 scenario) that for the largest scenarios this does not reflect the total exposed population, which is significantly higher. The results are presented in Tables 5.2 and 5.3 in terms of the percentage exposed within the grid.

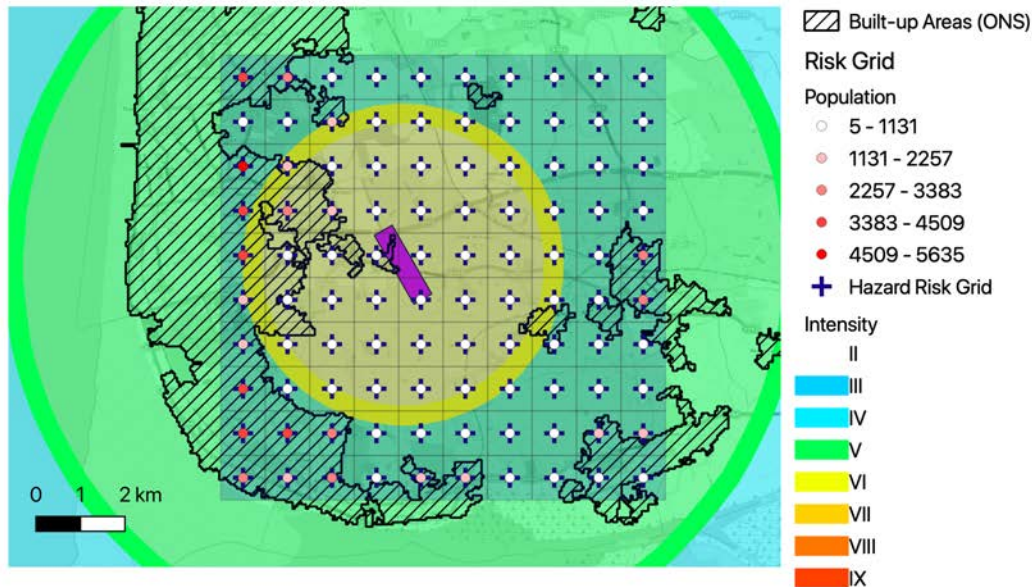


Figure 5.19. Example of exposed population within the 10 x 10 km study region. The purple area shows the surface projection of the  $M_L$  4.5 fault. The colour of each of the points within the grid indicates the population within. The colour of the background indicates the macroseismic intensity.

Table 5.2. Average population exposure (% of total within grid) within the 10 x 10 km study area to various *median* intensity levels for  $M_L$  2.5, 3.5 and 4.5 events.

	Intensity					
	2	3	4	5	6	7
<b>N(<math>M_L</math> = 2.5)</b>	100.0	1.2	0.0	0.0	0.0	0.0
<b>N(<math>M_L</math> = 3.5)</b>	100.0	100.0	67.6	0.0	0.0	0.0
<b>N(<math>M_L</math> = 4.5)</b>	100.0	100.0	100.0	100.0	9.1	0.0

Table 5.3. Average population exposure (% of total within grid) within the 10 x 10 km study area to various *median* PGV thresholds for  $M_L$  2.5, 3.5 and 4.5 events.

	PGV (cm/s)					
	0.1	0.2	0.5	1.5	5	10
<b>N(<math>M_L</math> = 2.5)</b>	1.2	0.0	0.0	0.0	0.0	0.0
<b>N(<math>M_L</math> = 3.5)</b>	100.0	67.6	67.6	0.0	0.0	0.0
<b>N(<math>M_L</math> = 4.5)</b>	100.0	100.0	100.0	100.0	9.1	0.0

## 5.5 Assessment of Potential Impact on the Built Environment

### 5.5.1 Fragility Functions – Chimneys

As presented in Section 5.3, the built environment within the region has been classified into distinct building classes (brick masonry detached, brick masonry terraced, mobile homes and light steel frames), some of which have chimneys. Each class therefore represents a large number of buildings that can have varying structural properties, such as floor height, material properties, wall layout, chimney height etc. When subject to a given earthquake record (see e.g., Figure 2.1), each building or chimney within the class may thus respond slightly differently, with different levels of deformation and damage. This needs to be accounted for when assessing the impact of the ground shaking on the built environment. Furthermore, a given level of PGA or PGV can be obtained from different earthquake records, each with slightly different frequency content, and each of these will lead to slightly different responses of the buildings and chimneys. We combine these uncertainties and therefore assess the probability of damage to the whole class of buildings/chimneys, under a given intensity of ground shaking (e.g. PGA, PGV), and this is done through fragility functions. Fragility functions therefore provide the probability of reaching or exceeding a certain level of damage (e.g., DS2), given the predicted level of ground shaking intensity (e.g., PGA).

Chimney fragility functions have been obtained from the study of Taig and Pickup (2016). Following an extensive review of chimney damage in past earthquakes, the latter proposed lower and upper bound fragility functions for buildings built before and after 1920 (see Figure 5.20).

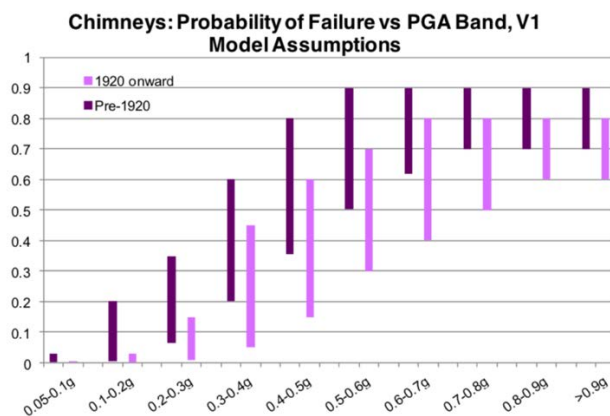


Figure 5.20 Chimney fragility functions proposed by Taig and Pickup (2016).

Taig (2018) recently evaluated the performance of these chimney fragility functions by calculating the probability of observing zero collapses in the four earthquakes with the highest ground motions that have occurred to date in the Groningen field (Huizinge, 't Zandt, Zandweer and Zeerijp). ShakeMaps provided by KNMI were used and the key result of the exercise was that the probability of zero collapses was low (2 - 10%) even when the lowest fragility assumptions were used. Considering that no chimney collapses have been observed to date, the conclusions drawn by Taig (2018) were that the fragility assumptions substantially

overstated the likelihood of failures at low levels of PGA. Considering these findings, the lower bound values presented in Figure 5.20 are taken as the best estimate for the chimney fragility functions, and a lognormal distribution has been fit to the data points of PGA versus probability of failure. The median and dispersion of these functions are shown in Table 5.4.

Table 5.4. Parameters of the lognormal chimney fragility functions.

<b>Chimney type</b>	<b>Median PGA (g)</b>	<b>Dispersion</b>
Pre-1920 masonry buildings	0.585	0.62
Post-1920 masonry buildings	0.765	0.52

### 5.5.2 Fragility Functions - Buildings

For the detached and terraced masonry houses and the light steel frame buildings, numerical models from studies being carried out as part of the probabilistic risk assessment in the Groningen gas field (van Elk et al., 2019) have been employed (see Figure 5.21a), given the similarity of these buildings in the Netherlands and the UK. These numerical models are described in detail in Arup (2017; 2019) and Mosayk (2017).

Capacity curves provide a description of the lateral strength and ductility capacity of a single-degree-of-freedom (SDOF) system (Figure 2.2) that has the first mode of vibration properties of the original multi-degree-of-freedom (MDOF) structure (see Figure 5.21b). The capacity curves for the three aforementioned building classes have been taken from the numerical models used in the Groningen field study. The capacity curve for mobile homes has been obtained from HAZUS (FEMA, 2004) as this class of building is not found in the Groningen field.

To develop fragility functions, the capacity curves of the SDOF systems are subjected to nonlinear dynamic analysis, and the peak displacement response of each analysis is obtained. When developing fragility functions for the Groningen gas field, Crowley et al. (2019) used ground motions that were consistent with the levels of hazard with between 500 to 100,000 years return periods, as the focus was on collapse fragility and fatality risk assessment. As the focus of the present study is on damage assessment (given the low magnitude range of the scenarios considered), ground motions with lower intensities (matching the hazard in Groningen with a return period of 50 years) were added to the pool of recordings used for the development of the fragility functions.

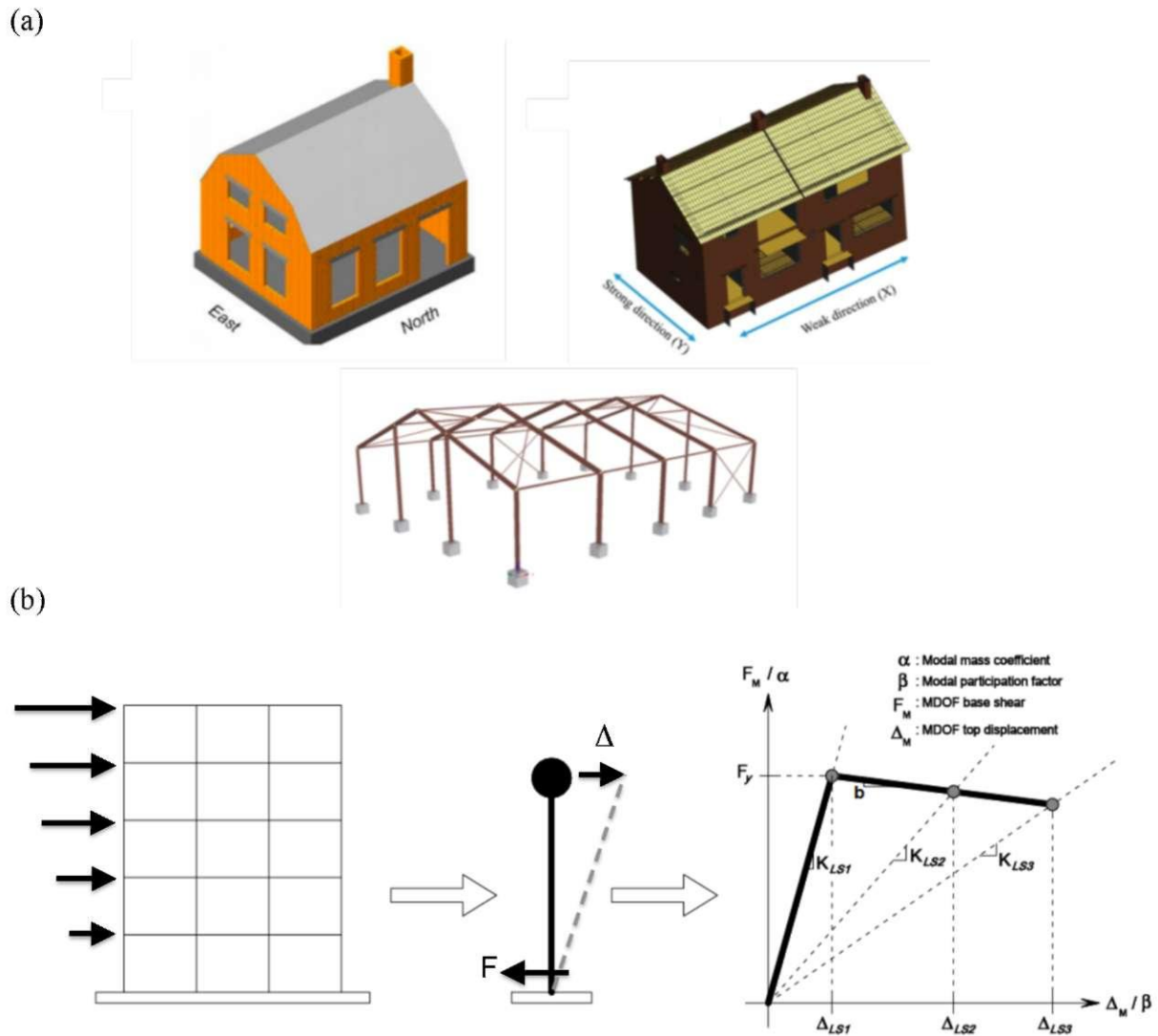


Figure 5.21. (a) Numerical models for detached (top left), terraced (top right) and light steel frame buildings. (b) Capacity curve (shown on the right) of a SDOF equivalent linear systems (middle figure) from the nonlinear analysis of MDOF structures (from Bal et al., 2010), where  $F$  is the lateral force and  $A$  is the displacement response.

With additional time and resources, one would ideally undertake a probabilistic seismic hazard analysis (PSHA) at the PNR site and then select records that are consistent with this hazard (following disaggregation of the hazard to understand the magnitude, distance, epsilon and duration of the events contributing most to the hazard at different levels of intensity) following, for example, the methods outlined in Bradley (2010) and Baker and Lee (2018). However, as this has not been possible within the timeframe of this project, the same records being used to develop fragility functions for the buildings in the Groningen gas field have been employed. It is noted that the duration of these records is likely to be longer than expected for the magnitude of the events considered herein and there may be differences in the frequency content, and this may lead to higher estimations of damage than actually expected.

Nonlinear dynamic analyses of SDOF models for each building class have been undertaken and the peak displacement response of each analysis has been recorded. This response is plotted

against a measure of intensity of each accelerogram (e.g., peak ground acceleration,  $SA[T=0.01s]$ ) and then piecewise linear regression of the displacement response has been carried out to obtain a bilinear relationship between the intensity measure and the response (see Figure 5.22). Piecewise linear regression has been employed as there is clearly a marked change in slope of the response displacements over the range of intensities considered (from linear to nonlinear response – shown in the capacity curve in Figure 5.21b), in particular for the brick masonry buildings.

Each spectral ordinate in the GMPE of Atkinson (2015) has been considered for the development of the fragility functions (from peak ground acceleration up to spectral accelerations at higher periods of vibration), and the final intensity measure selected for each building class is given by that which leads to the lowest dispersion in the response (i.e., the lowest scatter in the plots in Figure 5.22).

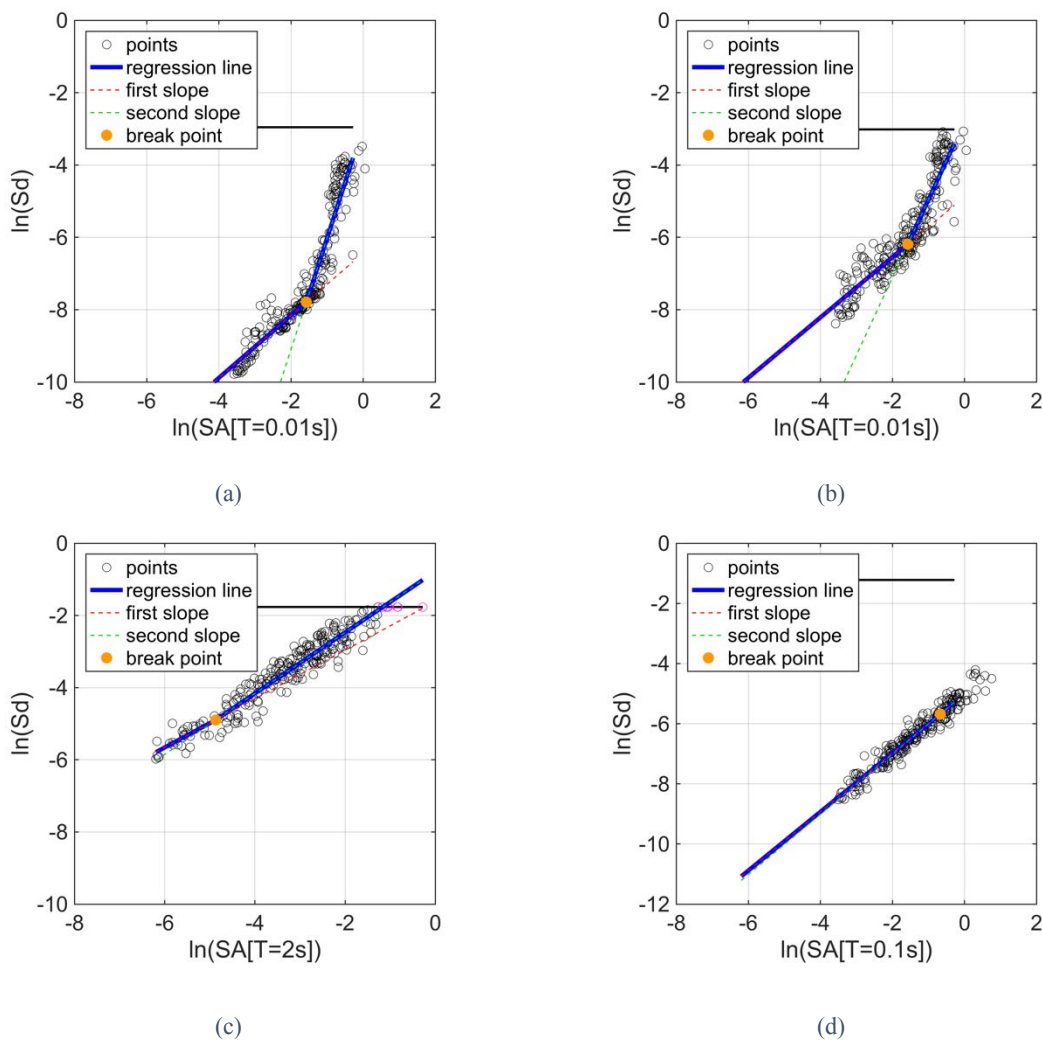


Figure 5.22. Response analyses (input spectral acceleration, SA vs. spectral displacement, SD, response) for SDOF models and piecewise linear regression (a) detached, (b) terraced, (c) mobile home and (d) light steel frame.

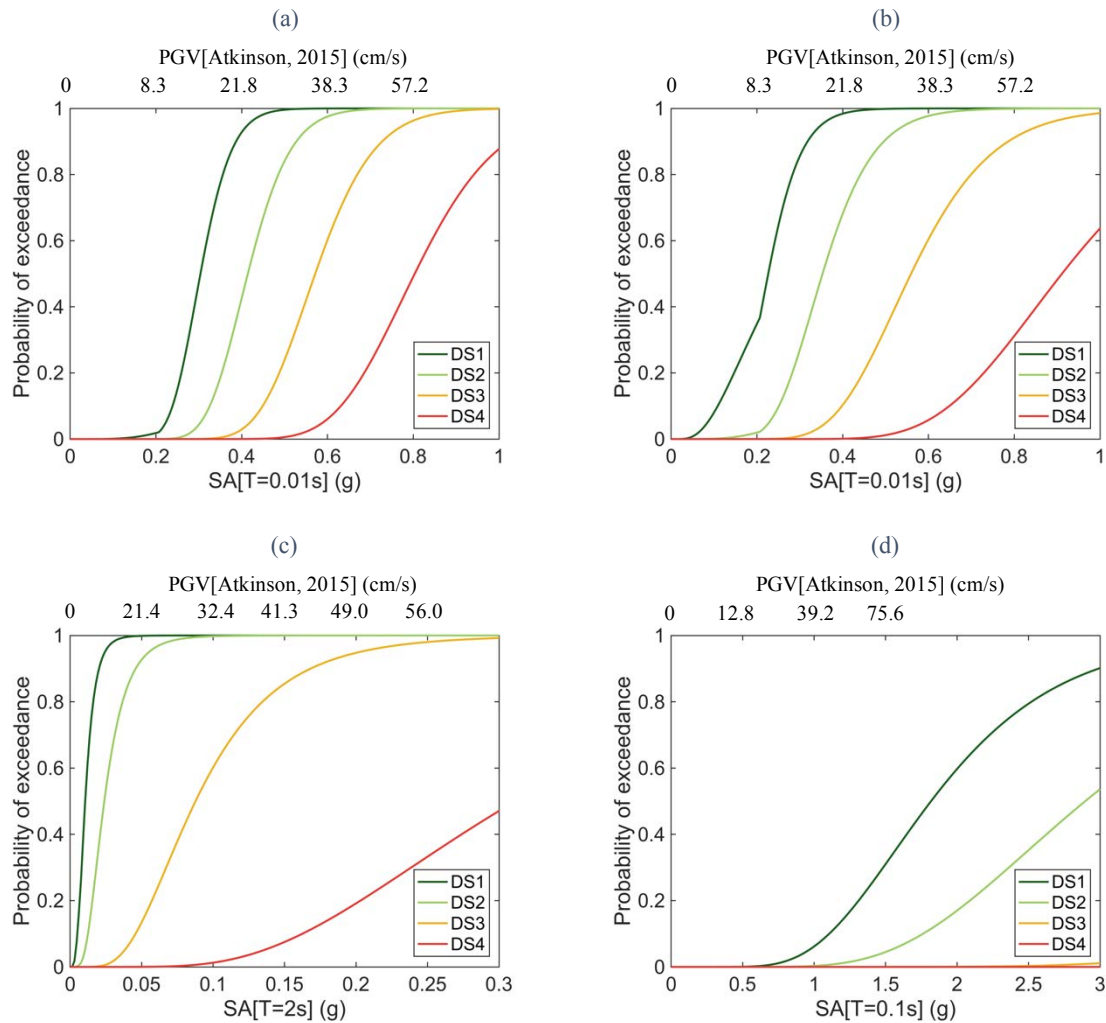


Figure 5.23. Building fragility functions (input spectral acceleration versus probability of exceeding damage state) for (a) detached, (b) terraced, (c) mobile home and (d) light steel frame for various damage states (DS, see Section 2.6). Indicative PGV values are provided, where possible and with minimal extrapolation, as equivalent motions (for a given value of SA) according to Atkinson (2015). These values were determined by comparing predictions of SA and PGV over a range of magnitudes ( $4 \leq M \leq 6$ , i.e., extending well above scenarios under consideration here) at short distances  $< 10$  km and for  $V_{s30} = 240$  m/s.

For a given damage state, a displacement threshold is identified (as shown by the vertical lines in the capacity curve shown in Figure 5.21b). Once this threshold of displacement is exceeded, the damage state is reached or exceeded. The displacement thresholds for each damage state have been obtained from experimental testing campaigns for the masonry buildings (Graziotti et al. 2019; Borzi et al., 2018) and from HAZUS (FEMA, 2004) for the light steel frames and mobile homes. In order to calculate the fragility function, it is thus necessary to calculate the probability of reaching or exceeding these levels of displacement. This can be undertaken using the equation describing the displacement response (given by the blue lines in Figure 5.22) together with the aleatory variability (defined by the scatter in the plots in Figure 5.22), and assuming a lognormal distribution. For each level of ground shaking intensity, the probability of reaching or exceeding each damage state is calculated and plotted, as shown in Figure 5.23. Interested readers are referred to Crowley et al. (2017; 2018) for a more detailed description, and complete presentation of the equations used to develop the fragility functions.

### 5.5.3 Scenario Damage Assessment

The Scenario Damage Calculator of the OpenQuake-engine (Silva et al., 2014) has been used to calculate the damage distribution for each scenario event. For each scenario event, the exposure model, the fragility functions (chimney and building) and the 200 ground motion fields have been input. The spatial distribution of the mean and standard deviation of the probability of reaching each damage state (DS1, DS2, DS3, DS4 and chimney collapse) for each building class is output. Figure 5.24 shows examples of some of the ground motion fields (in terms of peak ground acceleration) that have been input into the calculations for the  $M_L$  4.5 scenario event.

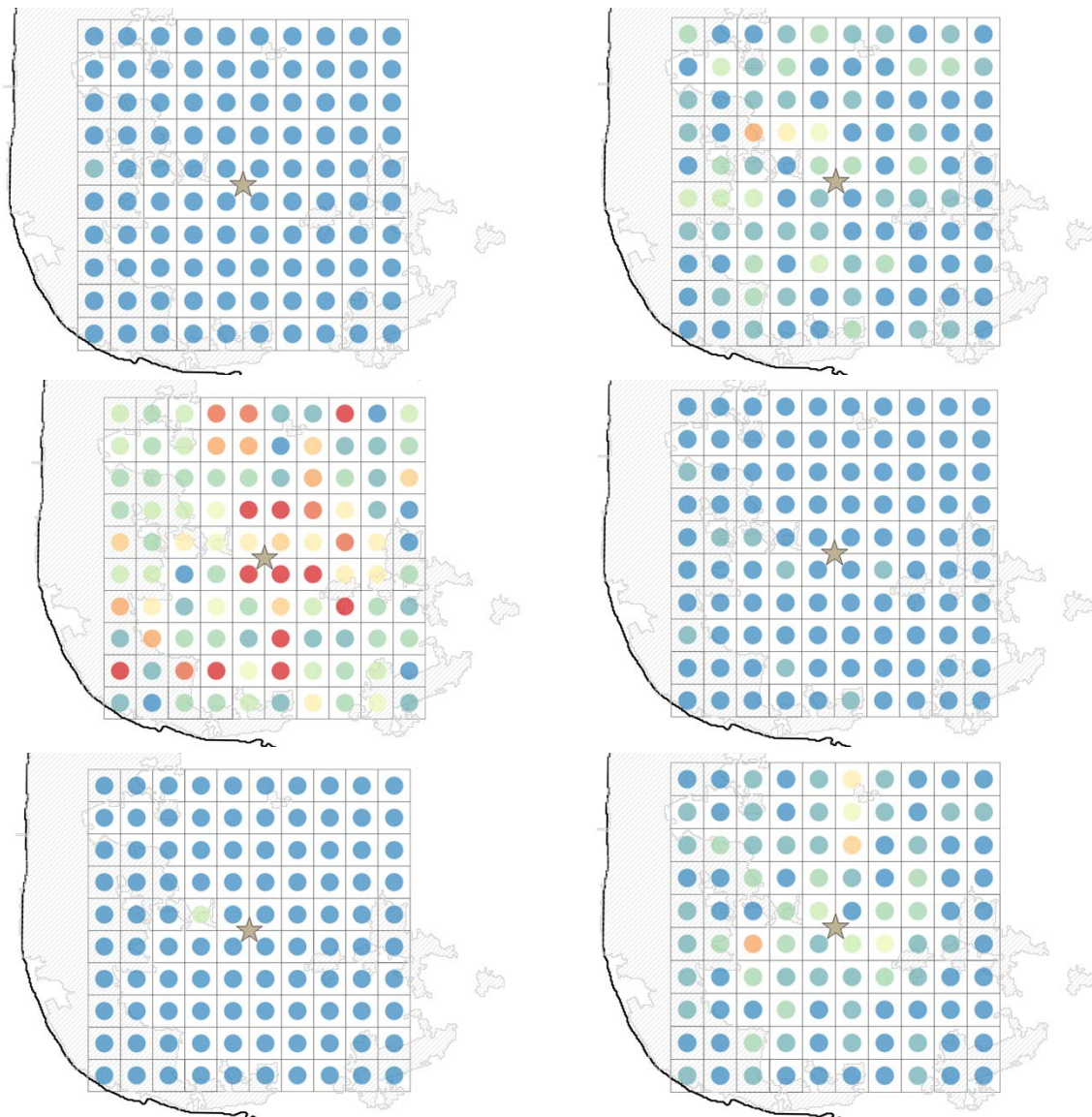


Figure 5.24. Example of 6 (of the total 200) spatially correlated ground motion fields used in the  $M_L$  4.5 scenario damage assessment, highlighting ground motion variability and spatial correlation.

Tables 5.5 to 5.7 presents a summary of results for each scenario event and for each assumption of  $V_{S30}$ . There is a very large standard deviation in the results (due to the aleatory variability in the ground motion), and this has a large influence on the mean. The median is thus also presented, and a box and whisker plot for scenario events with  $M_L$  of 3.5, 4.0 and 4.5 with  $V_{S30} = 240$  m/s are provided in Figure 5.25, showing the large variability in the estimates of damaged buildings.

Table 5.5. Summary of scenario damage results for the case where  $V_{S30} = 200$  m/s throughout the field.

Scenario ( $M_L$ )	DS1 (%)		DS2 (%)		DS3 (%)		DS4 (%)		Chimney failure (%)	
	Mean	Median	Mean	Median	Mean	Median	Mean	Median	Mean	Median
2.5	0.0	0.0	0.0	0.0	0.0	0.0	0.0	0.0	0.0	0.0
3	0.1	0.0	0.0	0.0	0.0	0.0	0.0	0.0	0.0	0.0
3.5	1.0	0.2	0.3	0.0	0.2	0.0	0.1	0.0	0.3	0.0
4	4.9	2.6	2.3	0.3	1.1	0.0	0.6	0.0	2.0	0.3
4.5	10.1	9.8	6.3	3.8	3.8	0.8	3.2	0.1	6.8	2.1

Table 5.6 Summary of scenario damage results for the case where  $V_{S30} = 240$  m/s throughout the field.

Scenario ( $M_L$ )	DS1 (%)		DS2 (%)		DS3 (%)		DS4 (%)		Chimney failure (%)	
	Mean	Median	Mean	Median	Mean	Median	Mean	Median	Mean	Median
2.5	0.0	0.0	0.0	0.0	0.0	0.0	0.0	0.0	0.0	0.0
3	0.1	0.0	0.0	0.0	0.0	0.0	0.0	0.0	0.0	0.0
3.5	0.9	0.2	0.2	0.0	0.0	0.0	0.0	0.0	0.1	0.0
4	3.9	2.2	1.6	0.2	0.8	0.0	0.4	0.0	1.4	0.2
4.5	9.6	8.6	5.4	3.5	3.2	0.8	2.3	0.1	5.4	2.1

Table 5.7. Summary of scenario damage results for the case where  $V_{S30} = 280$  m/s throughout the field.

Scenario ( $M_L$ )	DS1 (%)		DS2 (%)		DS3 (%)		DS4 (%)		Chimney failure (%)	
	Mean	Median	Mean	Median	Mean	Median	Mean	Median	Mean	Median
2.5	0.0	0.0	0.0	0.0	0.0	0.0	0.0	0.0	0.0	0.0
3	0.1	0.0	0.0	0.0	0.0	0.0	0.0	0.0	0.0	0.0
3.5	0.7	0.1	0.2	0.0	0.0	0.0	0.0	0.0	0.1	0.0
4	4.0	1.7	1.7	0.1	0.8	0.0	0.4	0.0	1.4	0.1
4.5	10.1	8.9	5.9	3.3	3.3	1.2	2.9	0.2	6.2	2.5

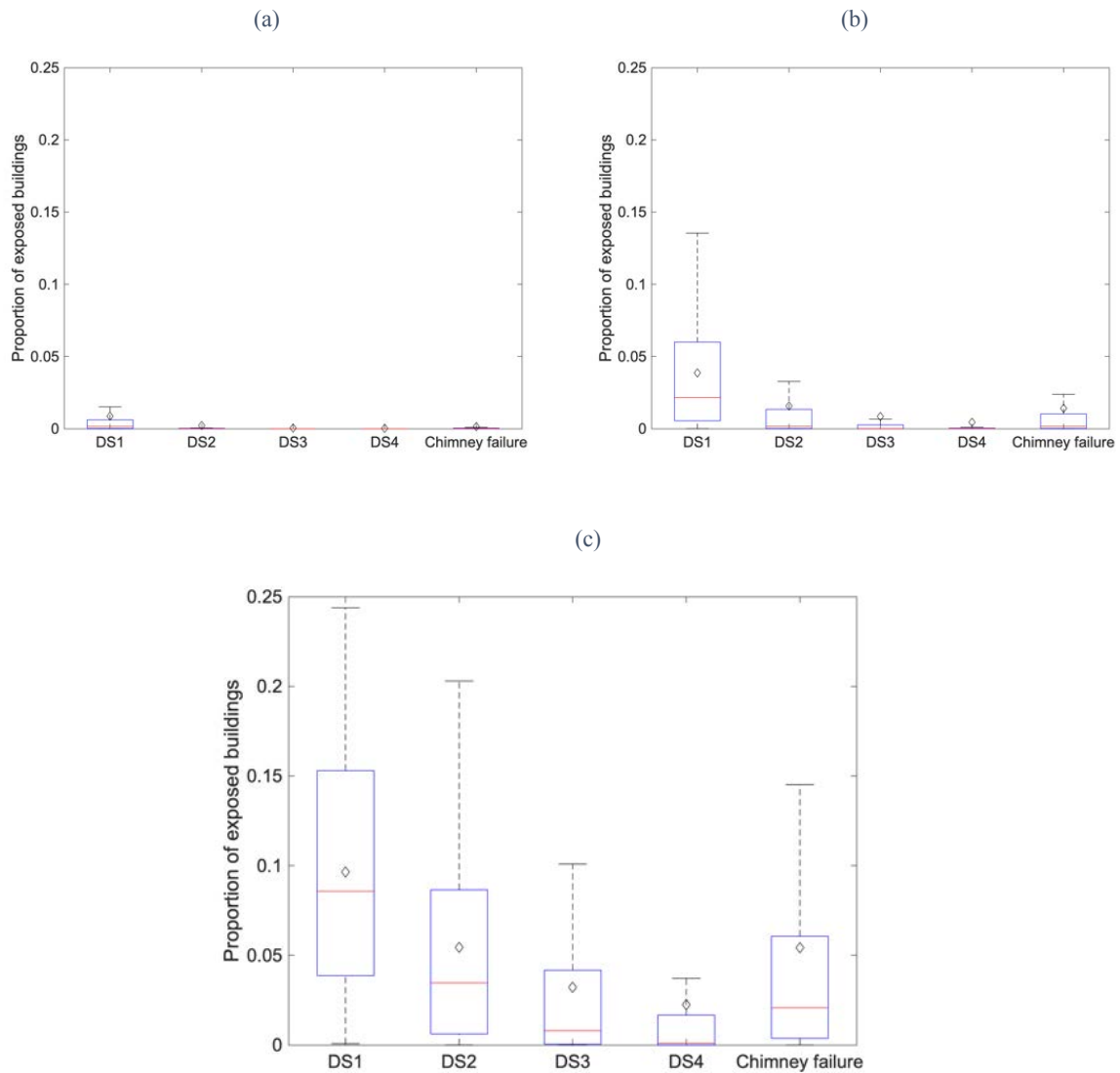


Figure 5.25. Box and whisker plot showing the total proportion of buildings (i.e., 0.25 = 25%) in each damage state for the scenario event with (a)  $M_L = 3.5$  and  $V_{S30} = 240$  m/s, (b)  $M_L = 4.0$  and  $V_{S30} = 240$  m/s and (c)  $M_L = 4.5$  and  $V_{S30} = 240$  m/s. The diamond indicates the mean, the box represents the lower to upper quartiles and the whisker indicates the total range (lowest to highest value). The median (50<sup>th</sup> percentile) is indicated by the red horizontal line.

Maps showing the distribution of the mean percentage of damaged buildings in each damage state and percentage of buildings with collapsed chimneys for the  $M_L$  3.0 and 4.5 scenario events with  $V_{S30} = 240$  m/s are shown in Figures 5.26 and 5.27, respectively.

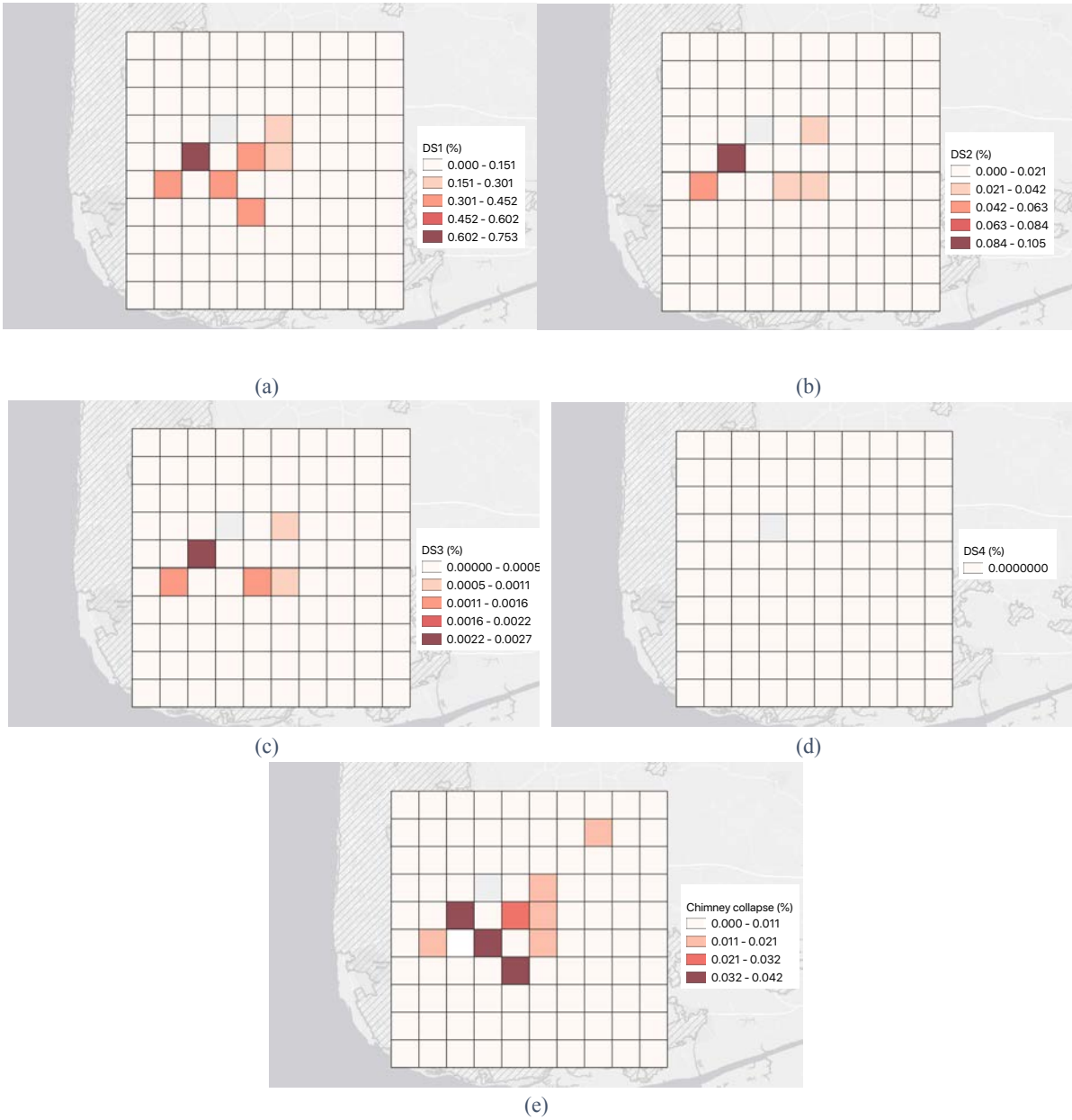


Figure 5.26. Spatial distribution of the mean percentage of buildings in each damage state for the scenario event  $M_L = 3.5$  and  $V_{S30} = 240$  m/s (a) DS1, (b) DS2, (c) DS3, (d) DS4, (e) chimney collapse.

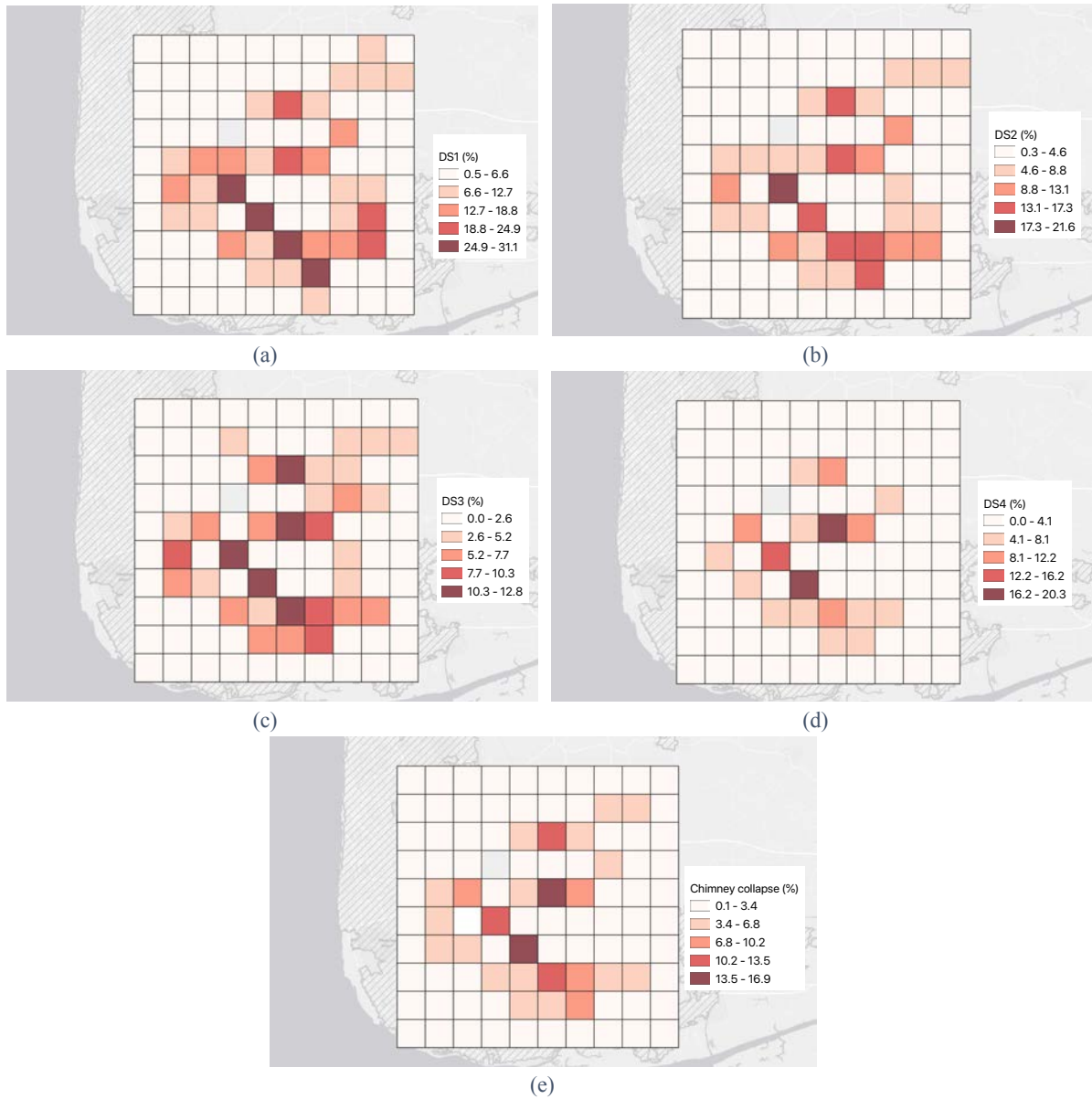


Figure 5.27. Spatial distribution of the mean percentage of buildings in each damage state for the scenario event  $M_L = 4.5$  and  $V_{S30} = 240$  m/s (a) DS1, (b) DS2, (c) DS3, (d) DS4, (e) chimney collapse.

#### 5.5.4 Discussion of Results

The scenario damage results presented in the previous section can be compared with the damage observed in past events with magnitudes of the same range, shallow depths and with similar characteristics, vulnerability and density of the building stock (i.e., Basel, Huizinge, Darmstadt, and Folkestone, as presented in Section 2.6).

The Basel (M3.2, depth 5 km) and Huizinge (M3.5, depth 3 km) events both led to a much larger number of buildings with DS1 (around 2000) than predicted herein for events of this magnitude, but these numbers are based on damage claims rather than inspections of damage made by structural engineers. It is highly likely that a large proportion of these buildings already had DS1 damage due to lack of maintenance and settlement of the foundations (Bommer et al., 2015).

On the other hand, the damage caused by the Darmstadt event (M3.6, depth 5km) had reported levels of DS1-2 damage and chimney collapse which are similar to the estimates made herein for the M<sub>L</sub> 3.5 scenario (i.e., a few hundred damaged buildings and tens of collapsed chimneys).

The Folkestone (M4.0, depth 5.3 km) led to around 1000 damaged buildings (DS1-2) and a number of collapsed chimneys, though the exact number is unknown. A similar order of magnitude of damaged buildings has been estimated for the M<sub>L</sub> 4.0 event herein.

#### 5.6 Assessment of Potential Impact on Well Integrity

The following text from API (2009) explains the basic concept of well integrity in relation to hydrocarbon extraction through hydraulic fracturing:

*“The primary method used for protecting groundwater during drilling operations consists of drilling the wellbore through the groundwater aquifers, immediately installing a steel pipe (called casing), and cementing this steel pipe into place. .... The steel casing protects the zones from material inside the wellbore during subsequent drilling operations and, in combination with other steel casing and cement sheaths that are subsequently installed, protects the groundwater with multiple layers of protection for the life of the well.*

*The subsurface zone or formation containing hydrocarbons produces into the well, and that production is contained within the well all the way to the surface. This containment is what is meant by the term “well integrity.” Moreover, regular monitoring takes place during drilling and production operations to ensure that these operations proceed within established parameters and in accordance with the well design, well plan, and permit requirements. Finally, the integrity of well construction is periodically tested to ensure its integrity is maintained.”*

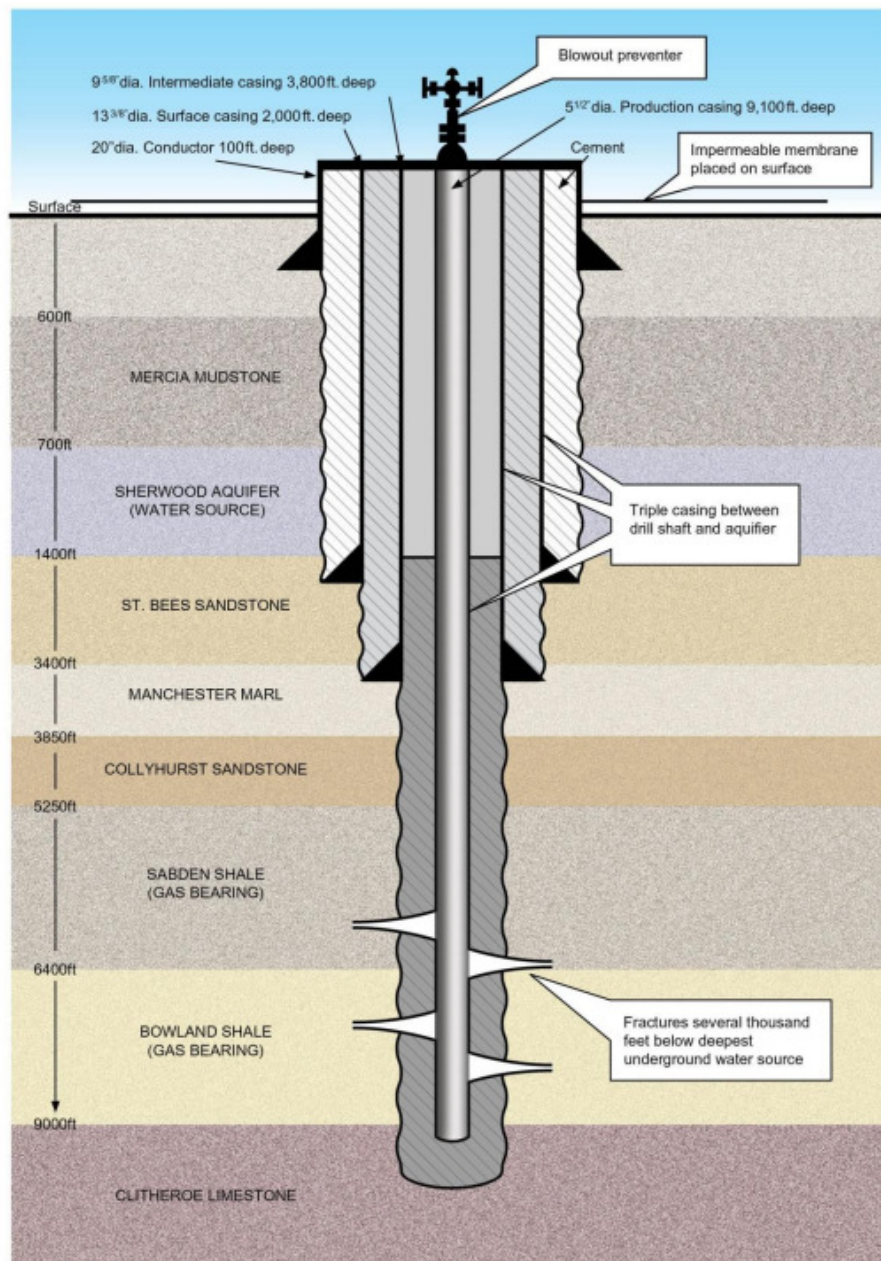


Figure 5.28. Schematic of Bowland Shale well (not to scale) (Regeneris, 2011).

Figure 5.28 shows a schematic of the Bowland Shale wells being used at Preston New Road. For the purposes of this study, well integrity is assumed to be compromised when either the yield flexural capacity, the yield strain or the shear stress capacity of the steel production casing (see Figure 5.28) is exceeded due to earthquake effects. It is noted that the exceedance of these capacities would not necessarily result in immediate exchange between the hydrocarbons or fracking fluid in the well and the surrounding groundwater, and these are thus conservative thresholds with which to assess the integrity of the well following seismic action.

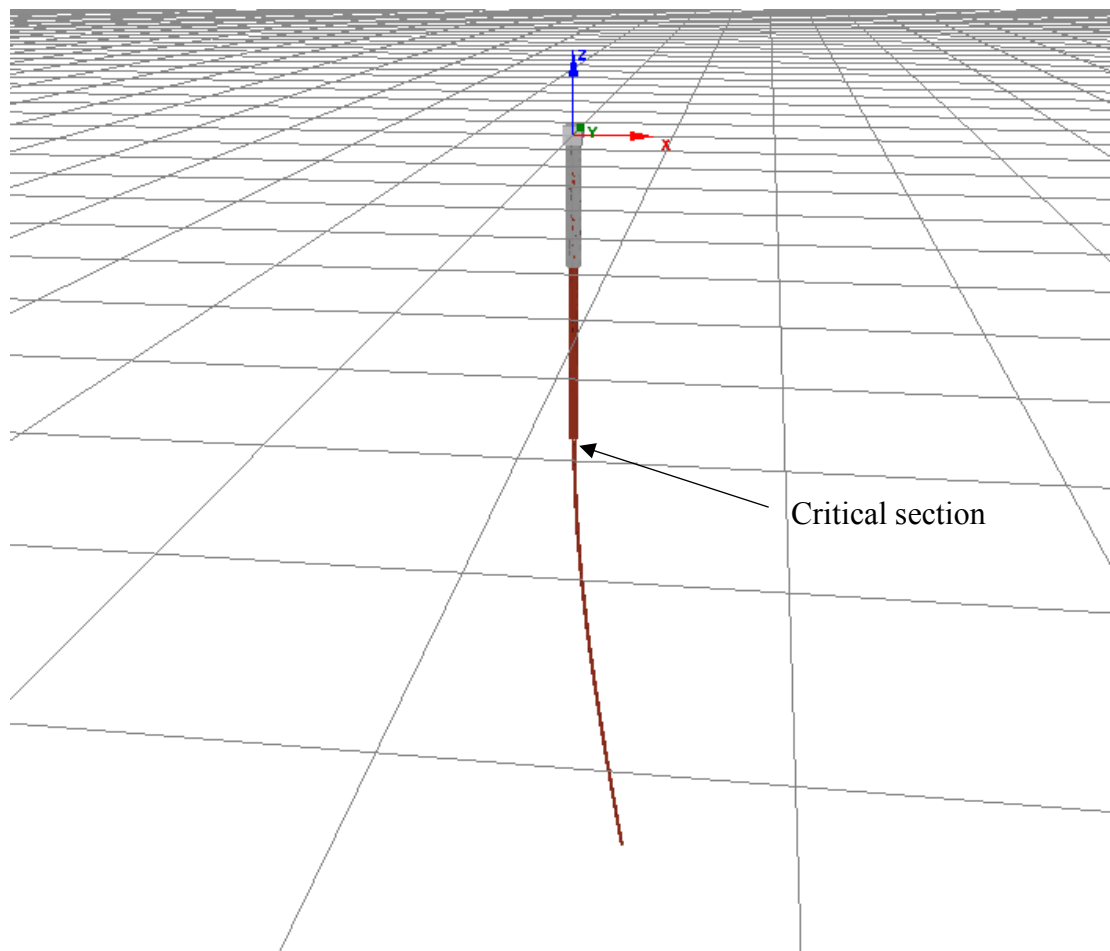


Figure 5.29. Structural model of the Bowland Shale Well.

In a vertical structural assembly subjected to lateral deformation, the highest strains and stresses are typically found in locations of the structure that are adjacent/interfacing with a very stiff body. For instance, in bridge piers, airport towers, lamp posts, etc., the highest strain/stress concentrations are observed at the base of the structures, where they are connected to the necessarily much stiffer foundation elements. In the case of the well structure being studied herein, the location where the sharpest variation of stiffness occurs is found in the production casing at the point where the intermediate casing ends, given how much stiffer the (cemented) upper sections of the well are with respect to the smaller non-cemented production casing. This (expected) structural behavior was also observed in preliminary structural analyses that not only showed the portion of the production casing below the intermediate casing deflecting much more than its upper counterparts when the well is subjected to lateral displacements (see Figure 5.29), but also confirmed that the largest strains and stresses were indeed located in the production casing at the point where the intermediate casing is interrupted; we henceforth term this location as the critical section of the well.

As discussed in Bommer (2018), buried structures may experience relative displacements due to one of three causes: (a) slip on a geological fault that the structure traverses; (b) liquefaction

of the surrounding ground; (c) the passage of the seismic waves along the structure or component. Only the first and the third causes have been considered herein, given that liquefaction would require moment magnitudes above at least 4.5 in order to be triggered (Green and Bommer, 2019). The potential impact of (a) and (c) on the aforementioned critical section of the well is therefore analysed herein (see sub-sections 5.6.1 and 5.6.2, respectively).

The material properties<sup>1</sup> of the steel casing used in Preston New Road were not available at the time of producing this report, and so typical values have been taken from the literature. Based on a nominal diameter of 5.5 inches (139.7 mm), as shown in Figure 5.28, a wall thickness of 10 mm has been taken from the common production casing sizes table reported in Renpu (2011) and steel class S355 has been assumed. The design properties for a S355 steel class Circular Hollow Section (CHS) with diameter of 139.7 mm and wall thickness of 10 mm are as reported in Table 5.8.

Table 5.8. Assumed mechanical properties of the (steel) production casing.

Parameter	Value	Units
Second moment of area (I)	$8.619 \times 10^6$	mm <sup>4</sup>
Elasticity Modulus (E)	$2 \times 10^8$	kN/m <sup>2</sup>
Elastic bending moment capacity ( $M_{max}$ )	43.8	kNm
Plastic shear force capacity	532	kN
Shear area	2594	mm <sup>2</sup>
Yield strain	0.0018	-

### 5.6.1 Well Integrity due to Fault Slip

For a well drilled vertically, fault slip would pose a very serious hazard if the well directly traversed the fault plane (Bommer, 2018). The amount of fault slip expected for a given magnitude can be estimated with the empirical relationship of Wells and Coppersmith (1994). For a **M** 4.5 event, fault displacement would be 17 mm, though it is noted that this relationship is derived from field observations and is not calibrated for events below **M** 5.2. Two mechanisms of failure are investigated: exceedance of maximum (i) bending capacity; and (ii) shear capacity.

As discussed already (and shown in Figure 5.29 above), when subjected to lateral loading the well behaves as an inverted cantilever with flexural bending of structural relevance developing downwards from the critical section, which is also the location at which largest values of bending moment are generated. Starting from the classical formulae to calculate the horizontal tip deflection ( $\delta$ ) of a cantilever for a given moment at its base ( $M$ ), it is then possible to estimate the critical length ( $L_{critical}$ ) below which the elastic bending moment capacity of the production casing ( $M_{max}$ ) is exceeded:

<sup>1</sup> It is reiterated that given the critical section discussion above, concrete properties needed not to be assumed, given that neither cracking of the cement nor separation of the cement from the steel casing had to be considered.

$$\delta = \frac{M \cdot L^2}{3EI} \quad \longrightarrow \quad L_{critical} = \sqrt{\frac{3EI \cdot \delta}{M_{max}}} \quad (21)$$

where E is the elasticity modulus and I is the second moment of area of the structural section. Using the production casing mechanical properties given in Table 5.8, the critical length (at which a lateral deformation of 17 mm makes the well reach its bending capacity, beyond which damage to the casing would occur) is found to be just under 1.5 m. This means that for the well integrity to be compromised through exceedance of its bending capacity under a magnitude 4.5 event, the fault would have to pass within the length of 1.5 m below the depth at which the intermediate casing is interrupted. Given that the total depth of the production casing is over 2 km, this critical length is less than 0.075 % of the total length of the well. There is thus a very small probability that a fault would actually pass within the critical length.

Furthermore, it is noted that the above calculations are very conservative (i.e., the critical length would in reality be much lower than the 0.075% value reported above), given that:

- the well is actually embedded in the ground (ignored in the above calculations), and this will reduce the deformability of the well;
- the horizontal component of the displacement is likely to be less than the fault displacement, given the dip of the fault (see Figure 5.30);
- in the calculations above the elastic bending moment capacity ( $M_{max}$ ) at the critical section has been adopted as resistance threshold, however, whilst exceedance of this value could cause some damage to the production casing, it would not necessarily result in immediate exchange between the hydrocarbons or fracking fluid in the well and the surrounding groundwater;
- the additional plastic flexural capacity of the steel casing has not been considered.

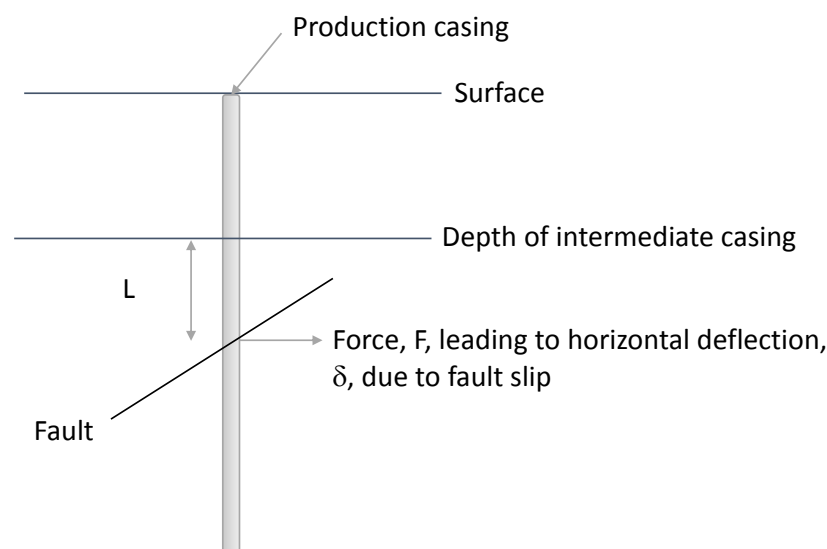


Figure 5.30. Sketch of the production casing and the parameters used to estimate well integrity due to fault slip.

As mentioned above, in addition to the flexural bending capacity of the production casing, the shear capacity also needs to be considered, given that, again, if shear forces above such value would develop in the well then the casing would experience damage. The shear stress capacity of the assumed steel section is given by the design plastic shear force resistance divided by the shear area, both of which are quantified in Table 5.8 (for the production casing considered in this study), thus leading to a shear stress capacity of approximately 205 MPa, which safely exceeds expected shear stresses in local faults. For instance, Fellgett et al. (2017) provide a comprehensive overview of the information available on the state of stress in the UK; based on analysis of available borehole data across Cheshire and Lancashire (including Preese Hall) they show that vertical stress gradients vary between 25 and 26 MPa/km, while the pore pressure gradient for this region is 10.8 MPa/km, or broadly hydrostatic (10 MPa/km). Maximum horizontal stress tends to follow 28 MPa/km, with no measured or calculated value exceeding 75 MPa down to 2.6 km depth.

### 5.6.2 *Well Integrity due to Wave-Induced Ground Strain*

As discussed in Bommer (2018), it is generally assumed that near the ground surface, seismic waves propagate vertically upwards. Therefore, a vertical well will be exposed to longitudinal strain from the passage of P-waves and lateral strain due to the passage of S-waves. The ground strain can be estimated from the ratio of PGV to the propagation velocity; since S-waves generally carry greater energy and propagate more slowly than P-waves, the lateral strain is likely to be greater.

The maximum strain that the production casing may sustain without damage (i.e., the so-called ‘yield strain’ for steel material structures) is given in Table 5.8 as equal to 0.18 %. Considering that peak strain is given by the ratio between PGV and  $V_s$ , and assuming a  $V_s$  of 240 m/s close to the surface, a PGV of 43 cm/s would be required to induce this level of strain. As discussed in Section 5.2.3, even under the largest magnitude 4.5 scenario, median values of PGV only up to 7.8 cm/s are estimated in the epicentral region. At least 2.25 standard deviations above the median would be needed to reach a PGV of 43 cm/s. This corresponds to the 98.8<sup>th</sup> percentile—a level of motion that for the given scenario has a 1.2% chance of being exceeded. Thus, there is an extremely low probability that the well could be damaged due to wave-induced ground strain for the largest event considered herein.

## 6. Conclusions

This work aimed to improve our understanding of induced seismicity at PNR-1z and potential future events in terms of its impact on people, the built environment and well integrity. For a summary of the work, we refer the reader to the Executive Summary at the start of this report. In the following we make our concluding remarks.

- The induced seismicity at Preston New Road during October and December 2018, with maximum magnitude of  $M_L$  1.5, led to ground motions that were practically imperceptible to people at the surface. Anthropogenic sources of vibration far exceed those caused by

even the largest earthquake during that period and typical structures were not, therefore, at any risk whatsoever from these motions.

- Moment magnitude is predicted from local magnitude using a theoretically based conversion (Deichmann, 2017), calibrated against data from a Swiss geothermal site in St. Gallen (Edwards et al., 2015). The European conversion equation of Gruenthal et al. (2009) underpredicted moment magnitude for these small events.
- The ground motion prediction equation (GMPE) of Atkinson (2015) performed well over a range of magnitudes, distances and periods, when compared to the recorded data at PNR-1z. For short to moderate periods at short distances ( $R_{\text{epi}} < 3$  km), the model tended to underpredict motions somewhat, however. We therefore recommend that the functional form and/or model coefficients are updated (using data from UK induced seismicity to date) to better fit the very near-field motions for small magnitude events (e.g., Bommer et al., 2006).
- We note, however, that simply because Atkinson (2015) underpredicts near-source motions for small events ( $M_L < 1.5$ ), we cannot rule out its direct applicability (without adjustment) at larger magnitudes ( $M_L > 3$ ), for which the model was developed. GMPEs should therefore be adjusted to fit local data, without having an impact on their predictions outside the available data range used for calibration.
- The 30 m average shear-wave velocity ( $V_{s30}$ ) of sites around PNR was low (200–270 m/s). In particular, areas characterised by blown sand deposits had the lowest velocity. Sites around PNR will therefore amplify ground motions significantly with respect to a (theoretical) site located on a rock outcrop.
- Intensity predictions were made for scenario events ( $M_L$  2.5, 3.5 and 4.5) at PNR. These showed that median field-wide epicentral-intensities would reach III (weak), IV (largely observed) and VI (slightly damaging) respectively. For the  $M_L$  3.5 and 4.5 scenarios at the 84<sup>th</sup>-percentile prediction of PGV, we estimate that some intensities could rise to V (strong) and VII (damaging) respectively, in limited pockets close to the epicenter.
- An inventory model has been developed for a 10 x 10 km grid around the PNR site for the purpose of probabilistic risk assessment. This includes a mapped building typology and population exposure, along with associated fragility functions.
- Risk analyses have been performed by simulating 200 random and spatially correlated ground motion fields (consistent with those used for the intensity models) and, for each randomization, calculating the number and type of damage to structures based on the regional building inventory and the fragility functions assigned to each type.
- We find that in terms of median risk (of which there is a 50% chance of not exceeding) the onset of non-structural building damage (DS1) is at  $M_L$  3.5. DS2 (minor structural damage) may occur at  $M_L$  4, DS3 and DS4 (major structural damage) may occur at  $M_L$  4.5. In terms of mean risk (which is more sensitive to the outlier predictions, e.g., high ground motions coinciding with more vulnerable structures in a particular location), we see onset of damage (for each state) at 0.5 magnitude units lower.
- The proportion of buildings in each damage state is affected by the  $V_{s30}$  on which it is located, with up to 0.9 % increase in the mean proportion of buildings in each damage state when going from  $V_{s30} = 280$  to  $V_{s30} = 200$  m/s.

- Well integrity is very unlikely to be affected by strain due to seismic waves from a nearby earthquakes (up to  $M_L$  4.5). The chance of damage, let alone failure, due to fault ruptures (with slip up to 17 mm) transecting the well is also very low due to the fact that a fault must transect a critical portion of the well (around 0.075 % of its length) to exceed its elastic bending capacity. Finally, the shear strength of the well itself is well in excess of the maximum known fault stresses at reservoir depths.

## **7. Acknowledgements**

We thank the Oil and Gas Authority for initiating this study and providing or facilitating the provision of various datasets used herein. We extend our thanks to the British Geological Survey, in particular Richard Luckett and Brian Baptie, who provided data for the surface seismometers operated by both the BGS themselves and those operated by Cuadrilla Resources. Map data copyrighted OpenStreetMap contributors and available from <https://www.openstreetmap.org>.

## 8. References

- Akkar, S. and Bommer, J.J., 2006. Influence of long-period filter cut-off on elastic spectral displacements. *Earthquake Engineering and Structural Dynamics*, 35(9), pp.1145-1165.
- Akkar, S., Sandıkkaya, M.A. and Bommer, J.J., 2014. Empirical ground-motion models for point-and extended-source crustal earthquake scenarios in Europe and the Middle East. *Bulletin of Earthquake Engineering*, 12(1), pp.359-387.
- Anderson, J.G. and Hough, S.E., 1984. A model for the shape of the Fourier amplitude spectrum of acceleration at high frequencies. *Bulletin of the Seismological Society of America*, 74(5), pp.1969-1993.
- Ancheta, T.D., Darragh, R.B., Stewart, J.P., Seyhan, E., Silva, W.J., Chiou, B.S.J., Wooddell, K.E., Graves, R.W., Kottke, A.R., Boore, D.M. and Kishida, T., 2014. NGA-West2 database. *Earthquake Spectra*, 30(3), pp.989-1005.
- API, 2009. Hydraulic Fracturing Operations—Well Construction and Integrity Guidelines. *API Guidance Document HF1, First Edition*, October, American Petroleum Institute, Washington D.C.
- Arup, 2014. Environmental Statement: Appendix L – Induced Seismicity. *Temporary Shale Gas Exploration: Preston New Road, Lancashire*. Cuadrilla Bowland Ltd., May, 140 pp.
- Arup, 2017. Typology modelling: Analysis results in support of fragility functions - 2017 batch results, Technical report: 229746\_031.0\_REP2005, November 2017.
- Arup, 2019. Typology modelling: Analysis results in support of fragility functions - 2018-2019 batch results, June 2019.
- Athanasopoulos, G.A. and Pelekis,, P.C., 2000. Ground vibrations from sheetpile driving in urban environment: measurements, analysis and effects on buildings and occupants. *Soil Dynamics and Earthquake Engineering*, 19(5), 371-387.
- Atkinson, G.M. and Morrison, M., 2009. Observations on regional variability in ground-motion amplitudes for small-to-moderate earthquakes in North America. *Bulletin of the Seismological Society of America*, 99(4), pp.2393-2409.
- Atkinson, G.M., 2015. Ground-motion prediction equation for small-to-moderate events at short hypocentral distances, with application to induced-seismicity hazards. *Bulletin of the Seismological Society of America*, 105(2A), pp.981-992.
- Baker J.W. and Lee C., 2018. An improved algorithm for selecting ground motions to match a conditional spectrum, *Journal of Earthquake Engineering*, 22 (4), pp.708-723.

- Barneich, J.A., 1985. Vibration problems in geotechnical engineering-vehicle induced ground motion. In proceedings of a symposium sponsored by the geotechnical engineering division in conjunction with the ASCE convention in Detroit, 187-202.
- Beyer, K. and Bommer, J.J., 2006. Relationships between median values and between aleatory variabilities for different definitions of the horizontal component of motion. *Bulletin of the Seismological Society of America*, 96(4A), pp.1512-1522.
- Bommer, J.J., Oates, S., Cepeda, J.M., Lindholm, C., Bird, J., Torres, R., Marroquin, G. and Rivas, J., 2006. Control of hazard due to seismicity induced by a hot fractured rock geothermal project. *Engineering Geology*, 83(4), pp.287-306.
- Bommer, J.J., Stafford, P.J., Alarcón, J.E. and Akkar, S., 2007. The influence of magnitude range on empirical ground-motion prediction. *Bulletin of the Seismological Society of America*, 97(6), pp.2152-2170.
- Bommer, J.J., Stafford, P.J. and Alarcón, J.E., 2009. Empirical equations for the prediction of the significant, bracketed, and uniform duration of earthquake ground motion. *Bulletin of the Seismological Society of America*, 99(6), pp.3217-3233.
- Bommer, J.J., Douglas, J., Scherbaum, F., Cotton, F., Bungum, H. and Fäh, D., 2010. On the selection of ground-motion prediction equations for seismic hazard analysis. *Seismological Research Letters*, 81(5), pp.783-793.
- Bommer, J.J., Crowley, H. and Pinho, R., 2015. A risk-mitigation approach to the management of induced seismicity. *Journal of Seismology*, 19(2), pp.623-646.
- Bommer, J.J., 2017. Predicting and Monitoring Ground Motions Induced by Hydraulic Fracturing. Technical report prepared for the Oil and Gas Authority, 23 pp. Online (last accessed 09/2019): [https://www.ogauthority.co.uk/media/3693/pgv-thresholds-for-control-of-induced-seismic-hazard\\_v5.pdf](https://www.ogauthority.co.uk/media/3693/pgv-thresholds-for-control-of-induced-seismic-hazard_v5.pdf)
- Bommer J.J., 2018. Integrity of Hydraulic Fracturing Wells During Earthquakes, Technical report for the Oil and Gas Authority, 12 April 2017, <https://www.ogauthority.co.uk/media/5156/5-julian-bommer-well-integrity-during-earthquakes.pdf>
- Bommer J.J. and Edwards, B., 2018. Evaluation of PPV Prediction and Monitoring for the Preston New Road TLS. A technical report prepared for the Oil and Gas Authority, 26 pp.
- Boore, D.M., Watson-Lamprey, J. and Abrahamson, N.A., 2006. Orientation-independent measures of ground motion. *Bulletin of the seismological Society of America*, 96(4A), pp.1502-1511.
- Boore, D.M., Thompson, E.M. and Cadet, H., 2011. Regional correlations of VS 30 and velocities averaged over depths less than and greater than 30 meters. *Bulletin of the Seismological Society of America*, 101(6), pp.3046-3059.

- Boore, D.M., 2013. The uses and limitations of the square-root-impedance method for computing site amplification. *Bulletin of the Seismological Society of America*, 103(4), pp.2356-2368.
- Boore, D.M., Stewart, J.P., Seyhan, E. and Atkinson, G.M., 2014. NGA-West2 equations for predicting PGA, PGV, and 5% damped PSA for shallow crustal earthquakes. *Earthquake Spectra*, 30(3), pp.1057-1085.
- Bora, S.S., Scherbaum, F., Kuehn, N. and Stafford, P., 2016. On the relationship between Fourier and response spectra: Implications for the adjustment of empirical ground-motion prediction equations (GMPEs). *Bulletin of the Seismological Society of America*, 106(3), pp.1235-1253.
- Borzi B., Crowley H. and Pinho R., 2008. Simplified pushover-based earthquake loss assessment (SP-BELA) method for masonry buildings, *International Journal of Architectural Heritage*, 2:4, 353-376.
- Bradley, B.A., 2010. A generalized conditional intensity measure approach and holistic ground-motion selection. *Earthquake Engineering & Structural Dynamics*, 39(12), pp.1321-1342.
- British Standards Institute (BSI), 2008. Guide to evaluation of human exposure to vibration in buildings, Part 2: Blast-induced vibration. BS 6472-2:2008.
- British Standards Institute (BSI), 2010. Mechanical vibration and shock — Vibration of fixed structures – Guidelines for the measurement of vibrations and evaluation of their effects on structures. BS ISO 4866:2010.
- British Standards Institute (BSI), 2014. Code of practice for noise and vibration control on construction and open sites – Part 2: Vibration. BS 5228-2:2009+A1:2014.
- Brune, J.N., 1970. Tectonic stress and the spectra of seismic shear waves from earthquakes. *Journal of Geophysical Research*, 75(26), pp.4997-5009.
- Brune, J.N., 1971. Correction to tectonic stress and the spectra of seismic shear waves from earthquakes. *Journal of Geophysical Research*, 76(20), p.5002.
- Caprio, M., Tarigan, B., Worden, C.B., Wiemer, S. and Wald, D.J., 2015. Ground motion to intensity conversion equations (GMICEs): A global relationship and evaluation of regional dependency. *Bulletin of the Seismological Society of America*, 105(3), pp.1476-1490.
- Chiou, B., Youngs, R., Abrahamson, N. and Addo, K., 2010. Ground-motion attenuation model for small-to-moderate shallow crustal earthquakes in California and its implications on regionalization of ground-motion prediction models. *Earthquake Spectra*, 26(4), pp.907-926.

- Chiou, B.S.J. and Youngs, R.R., 2014. Update of the Chiou and Youngs NGA model for the average horizontal component of peak ground motion and response spectra. *Earthquake Spectra*, 30(3), pp.1117-1153.
- Crowley, H., Polidoro, B., Pinho, R., and van Elk, J., 2017. Framework for developing fragility and consequence models for local personal risk, *Earthquake Spectra*, 33 (4) 1325-1345.
- Crowley, H., Pinho, R., van Elk, J. and Uilenreef, J., 2019. Probabilistic damage assessment of buildings due to induced seismicity. *Bulletin of Earthquake Engineering*, 17(8), pp.4495-4516.
- Crowley H., Pinho R., Cavalieri F., 2019. Report on the v6 Fragility and Consequence Models for the Groningen Field, NAM Platform, March 2019.
- Cotton, F., Scherbaum, F., Bommer, J.J. and Bungum, H., 2006. Criteria for selecting and adjusting ground-motion models for specific target regions: Application to central Europe and rock sites. *Journal of Seismology*, 10(2), p.137.
- Cuadrilla Resources, 2018. Preston New Road 1z Hydraulic Fracture Plan, Technical Report PNR1z HFP, 8 pp.
- Cuadrilla Resources, 2019a. Preston New Road-1z HFP Report, Technical Report PNR1z-HFP- Report-001, 25 pp.
- Cuadrilla Resources, 2019b. Hydraulic Fracture Plan PNR 2, Technical Report CORP-HSE-RPT-003, 24 pp.
- Deichmann, N., 2017. Theoretical basis for the observed break in  $M_L/M_w$  scaling between small and large earthquakes. *Bulletin of the Seismological Society of America*, 107(2), pp.505-520.
- Dost, B., Edwards, B. and Bommer, J.J., 2018. The relationship between  $M$  and  $M_L$ : a review and application to induced seismicity in the Groningen Gas Field, The Netherlands. *Seismological Research Letters*, 89(3), pp.1062-1074.
- Dost, B., Edwards, B. and Bommer, J.J., 2019. Erratum: The relationship between  $M$  and  $M_L$ : a review and application to induced seismicity in the Groningen Gas Field, The Netherlands. *Seismological Research Letters*, 90 (4), pp.1660-1662.
- Douglas, J. and Boore, D.M., 2011. High-frequency filtering of strong-motion records. *Bulletin of Earthquake Engineering*, 9(2), pp.395-409.
- Douglas, J., Edwards, B., Convertito, V., Sharma, N., Tramelli, A., Kraaijpoel, D., Cabrera, B.M., Maercklin, N. and Troise, C., 2013. Predicting ground motion from induced earthquakes in geothermal areas. *Bulletin of the Seismological Society of America*, 103(3), pp.1875-1897.

Douglas, J. and Edwards, B., 2016. Recent and future developments in earthquake ground motion estimation. *Earth-Science Reviews*, 160, pp.203-219.

Edwards, B. and Douglas, J., 2013. Selecting ground-motion models developed for induced seismicity in geothermal areas. *Geophysical Journal International*, 195(2), pp.1314-1322.

Edwards, B., Kraft, T., Cauzzi, C., Kästli, P. and Wiemer, S., 2015. Seismic monitoring and analysis of deep geothermal projects in St Gallen and Basel, Switzerland. *Geophysical Journal International*, 201(2), pp.1022-1039.

Edwards, B. and Bommer, J.J., 2018. Communicating the Effects of Surface Vibrations due to Induced Seismicity. A technical report prepared for the Oil and Gas Authority. 20 pp.

Edwards, B., Delvoeye, A. and Brotherson, L., 2018. Seismic Context Measurements for Induced Seismicity. Technical report for the Department of Business, Energy and Industrial Strategy. 43 pp.

Edwards, B., Zurek, B., van Dedem, E., Stafford, P.J., Oates, S., van Elk, J., deMartin, B. and Bommer, J.J., 2019. Simulations for the development of a ground motion model for induced seismicity in the Groningen gas field, The Netherlands. *Bulletin of Earthquake Engineering*, 17(8), pp.4441-4456.

Faenza, L. and Michelini, A., 2010. Regression analysis of MCS intensity and ground motion parameters in Italy and its application in ShakeMap. *Geophysical Journal International*, 180(3), pp.1138-1152.

Fellgett, M.W., Kingdon, A., Williams, J.D.O. and Gent C.M.A. State of stress across UK Regions, BGS Open Report OR/17/048, 64 pp.

FEMA, 2004. HAZUS-MH Technical Manual, Federal Emergency Management Agency, Washington D.C.

Foti, S., Hollender, S., Garofalo, F., Albarello, D., Asten, M., Bard, P.-Y., Comina, C., Cornou, C., Cox, B., Di Giulio, G., Forbriger, T., Hayashi, K., Lunedei, E., Martin, A., Mercerat, D., Ohrnberger, M., Poggi, V., Renalier, F., Sicilia, D., Socco, L.V., 2017. Guidelines for the good practice of surface wave analysis: a product of the InterPACIFIC project. *Bulletin of Earthquake Engineering*, 16(6), pp.2367-2420.

García, D., Mah, R.T., Johnson, K.L., Hearne, M.G., Marano, K.D., Lin, K.W., Wald, D.J., Worden, C.B. and So, E., 2012. ShakeMap Atlas 2.0: An improved suite of recent historical earthquake ShakeMaps for global hazard analyses and loss model calibration. In Proceedings of the *World Conference on Earthquake Engineering*, September 2012.

Graziotti F., Tomassetti U., Penna A., Magenes M., 2019. Tests on URM clay and calcium-silicate masonry structures: identification of damage states, Eucentre Foundation, Pavia, Italy, May 2019.

- Green, C.A., Styles, P. and Baptie, B.J., 2012. Preese Hall shale gas fracturing review and recommendations for induced seismic mitigation. *Department of Energy and Climate Change, London*, 26 pp.
- Green, R.A. and Bommer, J.J., 2019. What is the Smallest Earthquake Magnitude that Needs to be Considered in Assessing Liquefaction Hazard? *Earthquake Spectra*, 35(3), pp.1441-1464.
- Grünthal, G., 1998. European Macroseismic Scale 1998 (EMS-98). Cahiers du Centre Européen de Géodynamique et de Séismologie 15, Centre Européen de Géodynamique et de Séismologie, Luxembourg, 99 pp.
- Grünthal, G., Wahlström, R. and Stromeyer, D., 2009. The unified catalogue of earthquakes in central, northern, and northwestern Europe (CENEC)—updated and expanded to the last millennium. *Journal of Seismology*, 13(4), pp.517-541.
- Hanks, T.C. and Kanamori, H., 1979. A moment magnitude scale. *Journal of Geophysical Research: Solid Earth*, 84(B5), pp.2348-2350.
- Hicks, S.P., Verdon, J., Baptie, B., Luckett, R., Mildon, Z.K. and Gernon, T., 2019. A Shallow Earthquake Swarm Close to Hydrocarbon Activities: Discriminating between Natural and Induced Causes for the 2018–2019 Surrey, United Kingdom, Earthquake Sequence. *Seismological Research Letters*. DOI: 10.1785/0220190125.
- Hough, S.E., 2014. Shaking from injection-induced earthquakes in the central and eastern United States. *Bulletin of the Seismological Society of America*, 104(5), pp.2619-2626.
- Jayaram, N. and Baker, J.W., 2009. Correlation model for spatially distributed ground-motion intensities. *Earthquake Engineering and Structural Dynamics*, 38(15), pp.1687-1708.
- Joyner, W.B., Warrick, R.E. and Fumal, T.E., 1981. The effect of Quaternary alluvium on strong ground motion in the Coyote Lake, California, earthquake of 1979. *Bulletin of the Seismological Society of America*, 71(4), pp.1333-1349.
- Kempton, J.J. and Stewart, J.P., 2006. Prediction equations for significant duration of earthquake ground motions considering site and near-source effects. *Earthquake spectra*, 22(4), pp.985-1013.
- Knopoff, L., 1964. Q. *Reviews of Geophysics*, 2(4), pp.625– 660.
- Luckett, R., Ottemöller, L., Butcher, A. and Baptie, B., 2018. Extending local magnitude  $M_L$  to short distances. *Geophysical Journal International*, 216(2), pp.1145-1156.
- Madariaga, R., 1976. Dynamics of an expanding circular fault. *Bulletin of the Seismological Society of America*, 66(3), pp.639-666.
- Miller, M.M., Melbourne, T., Johnson, D.J. and Sumner, W.Q., 2002. Periodic slow earthquakes from the Cascadia subduction zone. *Science*, 295(5564), 2423-2423.

Miller; R. D. Park, C. B. and Xia, J., 1999. Multichannel analysis of surface waves. *Geophysics*, 64, 800–808.

Mosayk, 2017. Nonlinear dynamic analysis of index buildings for v5 fragility and consequence models, October 2017.

Musson, R.M.W., 1998. The Barrow-in-Furness earthquake of 15 February 1865: liquefaction from a very small magnitude event. *Pure and Applied Geophysics*, 152(4), pp.733-745.

Musson, R.M.W., 2003. Updated intensity attenuation for the UK. A British Geological Survey Technical Report. Earth Hazards and Systems Programme Open Report OR/13/029, 19 pp.

Musson, R.M.W., Grünthal, G. and Stucchi, M., 2010. The comparison of macroseismic intensity scales. *Journal of Seismology*, 14(2), pp.413-428.

Nievas C. I., Ntinalexis M., Kazantzidou-Firinidou D., Borozan J., Sangirardi M., Crowley H., Bommer J.J. (2019) “A Database of Damaging Earthquakes of Moment Magnitude from 4.0 to 5.5 (Part 2)” March 2019, Available at NAM Platform: <https://nam-onderzoeksrapporten.data-app.nl/reports/download/groningen/en/bb24d606-1c5d-40dc-a9af-968ed182c400>

Regeneris (2011). Economic Impact of Shale Gas Exploration and Production in Lancashire and the UK, Cuadrilla Resources.

Renpu W. (2011). Advanced Well Completion Engineering. Chapter 5 - Production Casing and Cementing, Elsevier Publishing, DOI: 10.1016/C2010-0-66820-9.

Richter, C.F., 1935. An instrumental earthquake magnitude scale. *Bulletin of the Seismological Society of America*, 25(1), pp.1-32.

Rietbrock, A. and Edwards, B., 2019. Update of the UK stochastic ground motion model using a decade of broadband data. Proceedings of the SECED conference, 9-10<sup>th</sup> September 2019, Greenwich, London.

Sandıkkaya, M.A., Akkar, S. and Bard, P.Y., 2013. A nonlinear site-amplification model for the next pan-European ground-motion prediction equations. *Bulletin of the Seismological Society of America*, 103(1), pp.19-32.

Silva, V., Crowley, H., Pagani, M., Monelli, D., Pinho, R., 2013. Development of the OpenQuake engine, the Global Earthquake Model’s open-source software for seismic risk assessment. *Natural Hazards*, 72(3), pp.1409-1427.

Stafford, P.J., Zurek, B.D., Ntinalexis, M. and Bommer, J.J., 2019. Extensions to the Groningen ground-motion model for seismic risk calculations: component-to-component variability and spatial correlation. *Bulletin of Earthquake Engineering*, 17(8), pp.4417–4439.

Taig A.R. and Pickup F.E., 2016. Risk Assessment of Falling Hazards in Earthquakes in the Groningen region, Arup Report 229746\_032.0\_REP1008.

Taig T., 2018. Groningen Region Falling Hazard Risk Assessments: An update, October 2018.

USACE, 1972. Army Corps of Engineers, Engineering and Design Systematic Drilling and Blasting for Surface Excavations. Chapter 2. Mechanics of Blasting.

van Elk J., Bourne S.J., Oates S., Bommer J.J., Pinho R. and Crowley H., 2019. A probabilistic model to evaluate options for mitigating induced seismic risk *Earthquake Spectra*, 35(2), pp. 537-564.

Wald, D.J., Worden, B.C., Quitoriano, V. and Pankow, K.L., 2005. *ShakeMap manual: technical manual, user's guide, and software guide* (No. 12-A1).

Wathelet, M., 2008. An improved neighborhood algorithm: parameter conditions and dynamic scaling, *Geophysical Research Letters*, 35, L09301, DOI: 10.1029/2008GL033256.

Wathelet, M., D. Jongmans, and Ohrnberger, M., 2004. Surface wave inversion using a direct search algorithm and its application to ambient vibration measurements, *Near Surface Geophysics* 2, 211-221.

Worden, C.B., Gerstenberger, M.C., Rhoades, D.A. and Wald, D.J., 2012. Probabilistic relationships between ground-motion parameters and modified Mercalli intensity in California. *Bulletin of the Seismological Society of America*, 102(1), pp.204-221.

Yenier, E. and Atkinson, G.M., 2015. Regionally adjustable generic ground-motion prediction equation based on equivalent point-source simulations: Application to central and eastern North America. *Bulletin of the Seismological Society of America*, 105(4), pp.1989-2009.

Yenier, E., Atkinson, G.M. and Sumy, D.F., 2016. Ground motions for induced earthquakes in Oklahoma. *Bulletin of the Seismological Society of America*, 107(1), pp.198-215.